Imperial College London

Turbulent/Turbulent Entrainment: A detailed examination of entrainment, and the behaviour of the outer interface as affected by background turbulence

Krishna S. Kankanwadi

Department of Aeronautics

Imperial College London

London, SW7 2AZ

This thesis is submitted for the degree of Doctor of Philosophy

January, 2022

I hereby declare that this thesis, and the research to which it refers, are entirely my own work and have not been submitted for any other award. Where other sources of information have been used they have been acknowledged and fully referenced.

Krishna S. Kankanwadi
London
January, 2022

Abstract

This thesis presents an experimental investigation into the effects of free-stream turbulence on entrainment and examines the outer boundaries of fluidic regions with turbulence present on both sides of the interface. Simultaneous particle image velocimetry (PIV) and planar laser induced fluorescence (PLIF) experiments are conducted in the wake of a circular cylinder subjected to grid generated turbulence.

The turbulent/turbulent interface (TTI) is identified for the first time. Analogous to the classical case of a turbulent/non-turbulent interface (TNTI), it facilitates the change in the enstrophy level between one region to the other. The TTI is seen to persist even at the most extreme background turbulence conditions.

In the far wake of a circular cylinder, free-stream turbulence is seen to reduce the net entrainment into the wake relative to a non-turbulent background. This behaviour is driven by infrequent yet powerful, intermittent detrainment events. It is found that the intensity of the background turbulence is most important in determining this behaviour, whereas the length scale is seen to have, only a second order effect.

The mechanism of this entrainment process is investigated and it is observed that role of viscosity in this process is insignificant when turbulence is present on both sides of the fluidic boundary. This is possible, since the availability of turbulent strain (and vorticity) on both sides of the interface in a TTI, allows the inertial term to take over the responsibilities of enstrophy production.

Finally, in the near-field of a cylinder wake, the influence of length scale is more important. Unlike in the far-field, coherent structures play a vital role in near wake development. The traditional increase in a bluff body wake width in the near field is reproduced and the effects of both wake meandering as well as wake growth through entrainment are investigated.

Acknowledgements

I would like to take this opportunity to acknowledge several people that helped me during the course of this PhD.

Firstly, I would like to express my deepest gratitude to my supervisor, Dr. Oliver Buxton, who was always generous with his time and helped me greatly during my PhD. Be it with impromptu meetings or providing me with crucial bits of advice in the lab, I am very thankful. Furthermore, I would like to thank him for being patient and understanding, especially during the rather complicated last couple of years under the global pandemic! I really could not have wished for a better supervisor.

I must acknowledge EPSRC for funding my PhD through Grant No. EP/R512540/1. This has not only supported me during this time, but also allowed me to present my work at APS-2018, TSFP11 and iTi-IX.

My PhD would not have been complete without the assistance that I received from the department's technical staff. I would especially like to thank Mr. Roland Hutchins, Mr. Alan Smith, Mr. Franco Giammaria and Mr. Ian James for their expert help with designing and manufacturing parts and also in assisting with numerous technical issues that I ran into in the past few years.

My time here at Imperial would not have been as enjoyable as it has been, had it not been for my wonderful group of friends, with whom I shared this experience. Among them, I would like to thank Murilo Cicolin, who helped me many a time with my setup and also shared several discussions about our experimental methods.

Lastly, I would like to express my thanks to my parents. They have been my rock over the course of my time at Imperial and without their care and understanding, I would not have been able to complete this PhD. They have supported me at every instance and I am forever grateful for having such supportive parents.

Contents

List of Figures

Chapter 1

Introduction

1.1 Motivation

Turbulent entrainment is the process by which mass is transferred into a body of turbulent fluid from the background. This process is of great significance as it defines the growth rate of regions encompassing turbulent fluid. Figure 1.1 is a stunning image that illustrates the growth of turbulent wakes in a large wind farm. The diameter of the wake significantly increases at increasing downstream distances from the turbine. Following continuity (assuming incompressibility in the flow), the increase in size of the wake has to be accompanied by a net transfer of mass (entrainment) from the background into the wake. Therefore, the entrainment process is central in governing all physical processes that lead to a transfer of mass across a fluidic boundary. These entrainment processes are critical in defining the behaviour of numerous industrial and environmental phenomena. These range from the design of wind farms to the governance of meteorological phenomena such as cloud formation in both terrestrial and extra-terrestrial settings (de Rooy *et al.*, 2013; Atreya *et al.*, 1999).

A significant amount of work has gone into understanding the TNTI as well as entrainment from a non-turbulent environment, reviewed in da Silva *et al.* (2014). However, the process of entrainment when the background itself is turbulent is largely unexplored and poorly understood, whilst being highly relevant to a majority of industrial and environmental flows. This

Figure 1.1: A photograph of the Horns Rev offshore wind farm near Denmark. Photograph by Christian Steiness. See Hasager *et al.* (2013) for more details regarding the image.

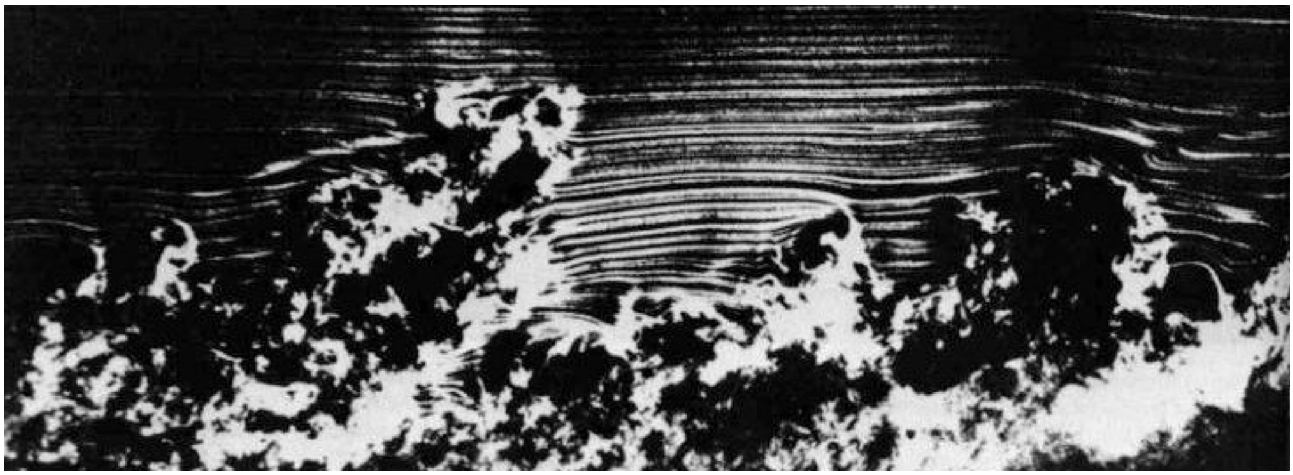

Figure 1.2: Side view of a turbulent boundary layer. Reproduced from van Dyke (1982).

thesis aims to correct that and provide insights into the effects of free-stream turbulence on the entrainment process and the mechanisms by which they are realised. To this end an experimental investigation was conducted, examining the wake of a circular cylinder that is subjected to grid-generated turbulence.

1.2 Literature review

Sections of literature review are present in all following chapters of the thesis. However, a summary of the critical references that govern the entrainment process are presented in this section.

1.2.1 The entrainment process

The rate of entrainment is effectively set by the dynamics near the outer boundary of particular turbulent regions. The outer boundary is characterised by a sharp contorted interface of finite thickness, which is beautifully illustrated in a smoke visualisation of a turbulent boundary layer seen in figure 1.2. When surrounded by irrotational fluid, this boundary is referred to as the turbulent/non-turbulent interface (TNTI), and has been studied to a great extent at the edges of wakes, jets, mixing layers and boundary layers (e.g. Bisset *et al.*, 2002; Westerweel *et al.*, 2005; Chauhan *et al.*, 2014). The pioneering work of Corrsin & Kistler (1955), made great strides into understanding the nature of the TNTI. They postulated the existence of a viscous 'superlayer' (VSL), a zone where viscosity plays a central role in acting to transmit vorticity, that is always present within the turbulent portion of the flow, to the irrotational background. They further proposed that the thickness of this layer is characterised by the Kolmogorov length scale, η, and, through dimensional arguments, that the propagation velocity of the layer is governed by the Kolmogorov velocity, $u_\eta = (\varepsilon\nu)^{1/4}$. Note, ε refers to the dissipation rate of turbulent kinetic energy and ν is the kinematic viscosity. These scalings have since been experimentally confirmed by Holzner & Lüthi (2011), who analysed a turbulent front generated by an oscillating grid. The zone just inside the viscous superlayer is termed the 'buffer layer' (Van Reeuwijk

& Holzner (2013)) and is responsible for the change in vorticity from the superlayer to the turbulent core. It is also a region where inertial effects dominate. A more detailed literature review of the turbulent boundary can be found in chapter 4.

It is well known that turbulent entrainment is a multi-scale process. Townsend (1976) comments on the fact that the rate of entrainment is independent of the magnitude of fluid viscosity and the slow process of diffusion is accelerated through the interaction with all scales. Furthermore, commenting on how it is the large scales that control the rate of entrainment into a bounding surface between a turbulent and irrotational region, Sreenivasan *et al.* (1989) explain that large-scale motions are responsible for the creation of a larger interface surface area which in turn results in an increased rate of entrainment through small-scale viscous processes. Mistry *et al.* (2016) provide experimental evidence by showing that a balance is maintained between interface surface area and local entrainment velocity, in order to keep the overall mass flux as a function of length scale, constant.

Whilst, entrainment from a non-turbulent background has been thoroughly investigated (da Silva *et al.*, 2014), the entrainment process when the background is also turbulent is largely unexplored. The outer edge of the viscous superlayer in a TNTI is only defined in an arbitrary sense and represents an enstrophy iso-surface, where the rate of change of enstrophy is equal to zero. It is clear to see that the TNTI is defined by the lack of enstrophy present on one side of the interface. However, a large discrepancy in enstrophy either side of the interface is not a requirement for a turbulent-turbulent interface (TTI), with a change in mean momentum being the only constant for a turbulent shear flow exposed to a turbulent background. It may be possible that this interface is no longer an enstrophy iso-surface due to the dynamically evolving conditions on the free-stream side of the interface. In this study we aim to examine the structure of the bounding interface between the wake and the free-stream turbulence. However, prior to answering this, a zeroth-order question may be raised by reviewing comments of da Silva *et al.* (2014) on the interfacial region between two bodies of fluid hosting different levels of non-zero turbulence. This is to question if the turbulent-turbulent interface even exists? Therefore, the first priority of this study is to answer this zeroth-order question. It is worth noting that the TNTI is simply a special case of an interfacial region between two bodies that

contain a differing level of turbulence in which one of the these bodies is irrotational. However, this study aims to tackle the problem of the general case by investigating the boundary and studying the entrainment process between two regions of differing yet non-zero levels of turbulence. Literature on turbulent-turbulent entrainment (TTE) is scarce and only a few studies have examined it. Previous studies have highlighted the importance of two parameters of the free-stream turbulence to TTE, $\{L,\ u'\}$, respectively, the integral length scale and turbulence intensity.

Gaskin *et al.* (2004) investigated the near field of plane jets in a turbulent environment. They observed that once the turbulence intensity in the background was strong enough to disrupt the energy-containing eddies of the jet, the entrainment mechanism switched from large-scale engulfment to the small-scale process of turbulent diffusion. In this case the result was a suppressed rate of entrainment as a result of the background turbulence. Khorsandi *et al.* (2013) come to a similar conclusion of suppressed entrainment due to background turbulence, in their experiments of an axi-symmetric turbulent jet. Ching *et al.* (1995) also determined the dominant parameter to be u' in the free-stream turbulence (FST). In a study that observed turbulent line plumes subjected to FST, they were able to show a marked change in the spreading of the plume when the plume convective velocity, w_*, was comparable to the background turbulence intensity. They explained that when background turbulence intensity was high enough, $w_* > \beta u'$, where $\beta \sim \mathcal{O}(1)$, energy containing eddies effaced the identity of the plume, greatly increasing the spreading angle and thereby entrainment. They were also able to show that the plume was destroyed from the onset when $u' > w_*$.

Eames *et al.* (2011), on the other hand, demonstrated the influence of L, on the spreading rate of a cylinder wake. They concluded that in the absence of FST, the wake grew diffusively with respect to $x^{1/2}$, where x is the streamwise distance downstream of the cylinder. However, when FST was introduced and the velocity deficit decayed sufficiently such that it was comparable to u' of the ambient turbulence, Eames *et al.* explained that the wake grew linearly with streamwise distance when L was larger than the wake width. If this condition was not met, the wake continued to grow diffusively.

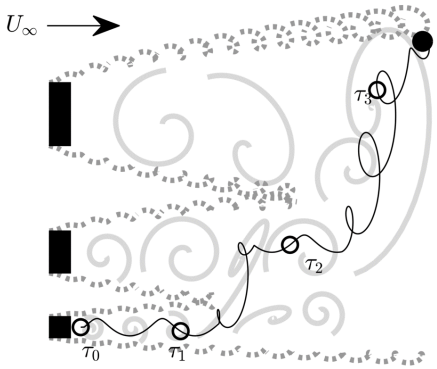

Figure 1.3: An illustration of the space-scale unfolding mechanism. The trace of a hypothetical fluid element is depicted at several time instances, τ_1, τ_2 and τ_3. Reproduced from Baj (2018).

It is clear to see from current literature that L and u' both have a part to play in the physics behind TTE, although there is no consensus on the influence of each parameter and their respective sensitivities. Furthermore, the answer to the core question is unclear from the literature, that is, whether free-stream turbulence acts to increase or decrease entrainment relative to a non-turbulent background. Given two bodies with differing levels of non-zero turbulence, it may be reasonable to expect that fluid is entrained from a region of low turbulence to a region of higher turbulence. Behaviour similar to that suggested is evident in the space-scale unfolding mechanism between adjacent wakes in multi-scale generated turbulence postulated by Laizet & Vassilicos (2012) and experimentally verified by Baj & Buxton (2019). This mechanism is defined by the enhanced transverse displacement of a hypothetical fluid element when adjacent wakes interact. Figure 1.3 illustrates the phenomenon and traces the movement of the discussed fluid element. Therefore, to answer this core question on the effect of free-stream turbulence and to address the sensitivities of its parameters on the entrainment process, a systematic investigation exploring the effects of these parameters has been conducted in chapter 3 of this study through the investigation of a wake behind a cylinder under the influence of free-stream turbulence, in which these parameters may be varied independently of each other.

1.2.2 Grid generated turbulence

User specified turbulence that was subjected to the circular cylinder was produced using turbulence generating grids. Turbulence generating grids have been studied extensively in the

literature, with seminal work being conducted on classical grids that house regular rectangular arrays of bars (Batchelor, 1953; Comte-Bellot & Corrsin, 1966). More recently, the flow downstream of space filling fractal grids was first characterised by Hurst & Vassilicos (2007). They investigated fractal grids of three kinds, each with a unique fractal pattern. These included fractal iterations of squares, cross grids and I grids. In general, across all families, Hurst & Vassilicos (2007) find that the number of iterations present in the grid, the external dimensions of the grid as well as the thickness ratio between each iteration are the three most critical geometric parameters in defining the downstream flow. Their findings with respect to square fractal grids are most crucial to this thesis, since they demonstrate a prolonged production region until a downstream distance, x_{peak}, where the turbulence intensity continues to increase. The downstream distance denoted by x_{peak} is referred to as the location of peak turbulence intensity. Turbulence downstream of a fractal grid is generated by the interaction between wakes generated of different bars of the grid. As a fractal grid consists of bars of different sizes, the downstream location at which the different wakes interact will vary (see figure 1.4). Mazellier & Vassilicos (2010) placed an upper bound on the location of peak turbulence intensity by evaluating the wake interaction length scale. This quantifies the distance at which the wakes from the two largest bars meet. At this point, the wake width will be equal to the distance between the zeroth iteration of the grid, $\mathcal{L}_0$. Using a scaling of the typical wake width, $\delta \sim \sqrt{t_j x}$, where t_j is the thickness of bar at the j^{th} iteration, they approximated the x_{peak} location to equal, $x_{peak} = 0.45\mathcal{L}_0^2/t_0$. Gomes-Fernandes *et al.* (2012) improved this estimation by accounting for the drag coefficient of the grid and the background turbulence intensity in the incoming flow.

For regular grids, the location of the peak turbulence intensity is much smaller than the respective location for fractal grids. The centreline turbulence intensity in the case of a regular grid fits very well with the well known power law in the decay region downstream of the x_{peak} location (Comte-Bellot & Corrsin, 1966). Mazellier & Vassilicos (2010) found an exponential decay of turbulence intensity even in the case of square fractal grids, for the region that followed x_{peak}.

For both regular grids as well as fractal grids, there is an expected slow downstream growth of the integral length scale (Comte-Bellot & Corrsin, 1966; Hurst & Vassilicos, 2007).

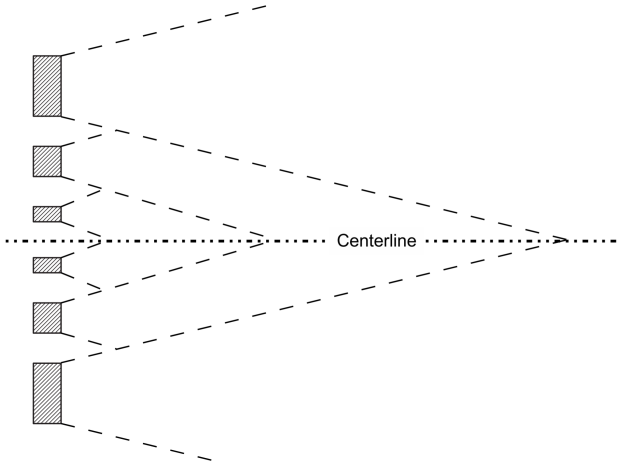

Figure 1.4: Schematic of the intersection points of wakes resulting from the bars of a fractal grid. Reproduced from Mazellier & Vassilicos (2010).

During the course of this thesis, the unique behaviour of both, regular grids as well as fractal grids was fully exploited. The prolonged production and decay regions of square fractal grids and the immediate decay of turbulence intensity downstream of a regular grid allowed for the construction of an extensive parameter space in both L and TI of the free-stream turbulence.

1.2.3 Turbulent wakes

The wake downstream of a circular cylinder transitions into turbulence at a Reynolds number, $Re_d \approx 260$ (Williamson, 1996). In this thesis the Reynolds number of the wake being examined ranges from approximately 4000 to 12000. This is well below the critical transition Reynolds number where the drag crisis of a circular cylinder occurs ($Re_d > 2 \times 10^5$). More specifically, the regime in which this study operates is known as the shear layer transition regime, which is in operation for a large range of Reynolds numbers, all the way from $Re_d = 1000$ to $Re_d = 200,000$ (Williamson, 1996). It should be noted that the shear-layer instability phenomenon is in operation within this regime. Prasad & Williamson (1997) state that for parallel shedding conditions, the onset of the shear layer instability occurs at $Re_d \approx 1200$. Whereas, in the case of oblique shedding conditions, this number increases to $Re_d \approx 2600$. The critical Reynolds numbers for the onset of the instability phenomenon are well below the Re_d of the current study and therefore it can be safely said that any incoming free-stream turbulence that will be applied

to the cylinder will not play a part in determining the existence of the instability. Therefore, one can be satisfied that the wake regime is consistent for all the campaigns conducted within this thesis.

Cantwell & Coles (1983) highlight the critical influence of coherent structures in wake development in the near field. They examine the near wake of a circular cylinder in the sub-critical regime at a Reynolds number of 140,000. Cantwell & Coles (1983) suggest that the dominant topological feature of the near wake is formation and evolution of saddle points between shed vortices. They conclude that a large part of the turbulence production in the wake occurs at these saddle points and explain that this is probably a result of the imposed strain field, which causes significant vortex stretching at intermediate scales. Furthermore, they explain that entrainment is also closely associated to saddle points and is concentrated near the upstream facing interface of each shed vortex.

Traditionally the entrainment phenomena have been decomposed into one of two processes, either occurring through engulfment or nibbling. Engulfment is a large-scale inviscid process where large regions of ambient fluid are deposited into the bulk of the turbulent fluid, whereas, nibbling is a small-scale viscous process that occurs at the outer boundaries of the turbulent region over the smallest physical length scales (Corrsin & Kistler, 1955).

Several investigators in the past have examined the relative influences of both engulfment and nibbling on the entrainment process. Whilst some debate still exists, nibbling is often seen to be the more dominant process. Mathew & Basu (2002) show that entrainment most often occurs through a nibbling process in a data-set comprising of a direct numerical simulation (DNS) of round jet flow. Westerweel *et al.* (2009) conduct experiments 60 to 100 nozzle diameters downstream of a round jet. They show that the total engulfed mass only consisted of less than 10% of the total entrained mass and thereby, the entrainment process is dominated by small scale nibbling. Taveira *et al.* (2013) investigate Lagrangian statistics in a DNS data-set of a turbulent plane jet. They show that with millions of particles initially seeded in the irrotational flow, only 1% of them make their way into irrotational bubbles within the jet. Similarly, Mistry *et al.* (2016) show that in their experimental study of an axi-symmetric jet, which was conducted

approximately 50 diameters downstream, only 0.44% of the turbulent area was accounted for by engulfed fluid. The dominance of the small-scale nibbling process in far-field entrainment is clearly established through the literature.

However, in the presence of coherent structures in the near-field of a free shear flow, the influence of engulfment is not negligible. Dahm & Dimotakis (1987, 1990) conduct flow visualisation and measurements of scalar concentration downstream of a turbulent jet and explain that the entrainment process can be characterised by the local large scales of the flow. They find pockets of unmixed ambient fluid deep inside the core of the jet, indicative of engulfment being a significant entrainment process in the presence of large scale coherence. Burridge *et al.* (2017) similarly highlight the significance of engulfment in their experimental study of an axi-symmetric pure turbulent plume. They identify regions where coherent structures are present through analysis of the local plume width and coin them as 'eddy present' events. They explain that the passage of these large-scale coherent structures at the plume edge drives pockets of ambient fluid at significant velocities. This enhanced momentum enables these pockets to be engulfed into the plume. Hence, they conclude that the engulfment by large scale eddies constitutes a significant part of the process of turbulent entrainment by plumes. Once engulfed, pockets of ambient fluid are mixed through viscous diffusion of vorticity (Townsend, 1976).

Furthermore, in the near field of a wake, 'meandering' plays a significant role in near-field wake development. This phenomenon has been studied extensively in applications relating to flow downstream of wind turbines. Baker & Walker (1984) first observed wake meandering in full-scale measurements downstream of a horizontal axis wind turbine. Ainslie (1988) noticed that a variability in the wind direction gave rise to wake meandering particularly in non-stable atmospheric conditions. Wise & Bachynski (2020) further comment that in addition to atmospheric stability, meandering is likely caused by turbulence, shear, veer, wind speed etc. In the context of this study, meandering is defined to represent the transverse oscillations of the vortical structures shed from the cylinder. Introducing wake meandering is important, since it contributes to mean wake spreading in the near field, which is often discussed in literature (Jensen, 1983). Wake meandering is further addressed in chapter 5, where a decoupled analysis aims to quantify the effect of background turbulence on near-wake entrainment and meandering.

1.3 Thesis objectives and outline

Provided below is a summary of the questions we aim to answer during this thesis.

1. Does the turbulent/turbulent interface exist? (*Chapter 3*)
2. Does background turbulence act to increase or decrease entrainment into the wake of a circular cylinder? (*Chapters 3 and 5*)
3. What are the relationships of length scale and intensity of the background turbulence with respect to entrainment behaviour? (*Chapter 3*)
4. What are the mechanisms of entrainment within a turbulent/turbulent interface? (*Chapter 4*)
5. What are the effects of background turbulence in the near wake of a circular cylinder? In particular, are these effects on mean wake spreading realised principally via entrainment, meandering or a combination of both? (*Chapter 5*)

This thesis consists of six chapters, with the first one being this introduction. The experimental methodology utilised to address the questions posed above is detailed in chapter 2. Chapters 3 to 5 act as the results chapters. The findings reported in chapter 3 aim to answer questions 1, 2 and 3, and have been published in Kankanwadi & Buxton (2020). Chapter 4 analyses the interfacial region between two regions of turbulent fluid and aims to answer question 4. Part of the results presented in this chapter have been published as a book chapter (Kankanwadi & Buxton, 2021), and at the time of writing, the rest is under revision for publication in *J. Fluid Mech.*. The final question that is posed is addressed in chapter 5. The near field development of the wake is examined with a special interest on the entrainment behaviour. Finally, chapter 6 aims to summarise all the discussions and acts as a conclusion. In addition to the results chapters, a few minor appendices have been added to the thesis that address specific issues. These have been omitted from the main text in order to aid the narrative of the thesis.

Chapter 2

Experimental Methods

Firstly, a few points about the standard nomenclature that is used for the rest of the thesis must be made. x denotes the streamwise direction (x_1), y denotes the cross-stream or the transverse direction (x_2) and finally z denotes the spanwise direction (x_3) which runs parallel to the vertically mounted circular cylinder. (u, v, w) represent the velocity components and are used interchangeably with (u_1, u_2, u_3) when such notation is more convenient to use. Finally, the fluctuating component is described with an apostrophe as the suffix, (u'_1, u'_2, u'_3). These conventions describe the basis of the nomenclature used throughout the thesis. Further symobology is appropriately introduced and utilised in the following sections.

2.1 Facility and inflow conditions

All experimental campaigns that were carried out in this study were conducted in a water flume located at Imperial College London. This is a closed loop, open channel facility with a working section that stretches 9 m in length and a square cross-section of width, $H = 0.6\,\mathrm{m}$. The flume is capable of producing flow velocities of up to $1\,\mathrm{ms}^{-1}$. However, all experiments were conducted at an inlet velocity, $U_\infty \approx 0.4\,\mathrm{ms}^{-1}$, in order to ensure flow conditions were relatively unaffected by surface waves. This resulted in a global Reynolds number with respect to flume width, $Re_H \approx 240000$.

The wake of a circular cylinder was investigated at various downstream locations in the presence of free-stream turbulence during the course of this study. Two distinct cylinders of diameters, $d = 30\,\text{mm}$ and $d = 10\,\text{mm}$, were utilised. The cylinders produced Reynolds numbers with respect to their cylinder diameters of, $Re_d \approx 12000$ and $Re_d \approx 4000$ respectively. This firmly placed the flow around the cylinder in the sub-critical regime (Williamson, 1996). Furthermore, the presence of the cylinders alone in the working section, resulted in blockage ratios of 5% and 1.7%, thereby suggesting that wall effects may be considered negligible with respect to their impact on the entrainment behaviour downstream of the cylinder.

2.2 Experimental setup

Across all of the experimental campaigns conducted in this study, experimental techniques such as planar particle image velocimetry (PIV) and cinematographic stereoscopic particle image velocimetry were utilised. For all but one of the campaigns, these techniques were combined with simultaneous planar laser induced fluorescence (PLIF) experiments. Figures 2.1 and 2.2 provide illustrations of some of the experimental setups used during the course of the study. Note that the coordinate system has been shifted downstream of the rear face of the circular cylinder in the interest of clarity.

2.2.1 Grids

In this study, the incoming free-stream turbulence incident on the circular cylinder was produced by turbulence generating grids placed upstream of the circular cylinder. A total of 4 Perspex grids were manufactured and used. These grids were cut using 10mm sheets of Perspex in a laser cutting facility. Prior to manufacture, all designed grids were modelled in a finite element software (*Creo Simulate*) and it was ensured that they would not fail under appropriate loading conditions. Two of the used grids were space filling square fractal grids (SFG), whereas the other two were square regular grids (SRG). The philosophy behind the design of these grids was to encourage the $\{L, u'\}$ parameter space to be as widely investigated as possible, in order to

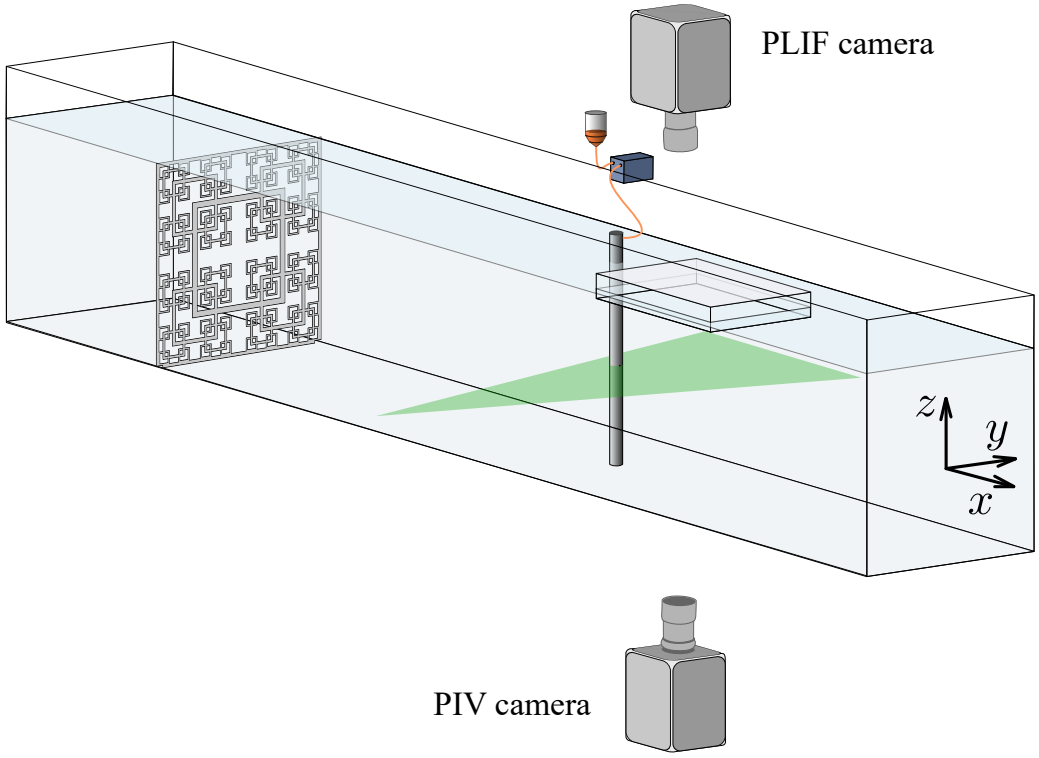

Figure 2.1: An example of the experimental set-up used during campaign II. Note that, for clarity, the coordinate system has not been plotted on the origin (which lies on the rear face of the circular cylinder), instead it has been shifted downstream in the streamwise direction.

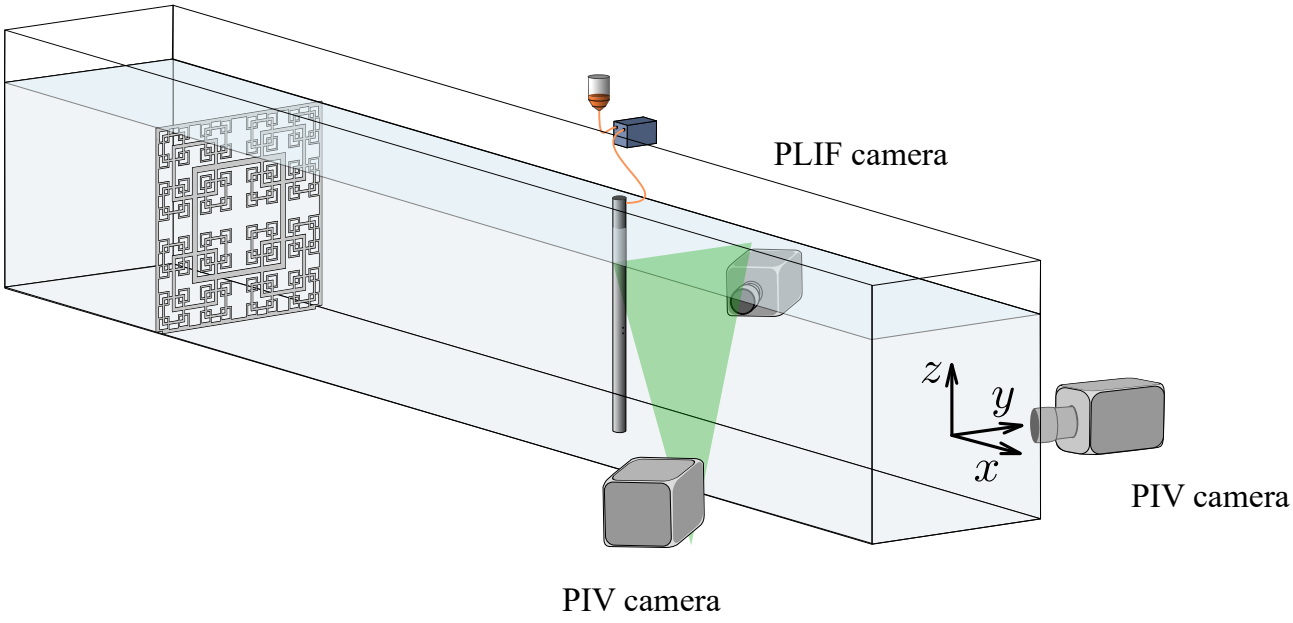

Figure 2.2: An illustration of the experimental setup used in campaign III. Note that the laboratory coordinate system has been shifted downstream in the interest of clarity.

Table 2.1: Fractal grids specification

Grid	T (mm)	N	$\mathcal{L}_0$ (mm)	t_0 (mm)	σ	R_L	R_t
SFG 5	569	4	312	15.3	33.76%	0.477	0.591
SFG 7	569	4	354	21.5	34.50%	0.389	0.533

Table 2.2: Regular grids specification

Grid	T (mm)	$\mathcal{L}_0$ (mm)	t_0 (mm)	σ
SRG 38	569	37.6	5.2	33.94%
SRG 111	569	111.3	12.7	32.01%

truly test the sensitivities of the entrainment process to both length scale as well as turbulence intensity. The flow downstream of all four grids was fully characterised and therefore the cylinder could be strategically placed at varying downstream distances so as to independently vary a single parameter in the background turbulence whilst the other remained constant. This followed the methodology of Melina *et al.* (2017). Tables 2.1 and 2.2 detail the design parameters of the fractal and square regular grids respectively, and figures 2.3 and 2.4 provide a schematic of all the turbulence generating grids. Note, T represents the width of the grid. In order to mount these grids in the flume they were encased in a frame and the blockage values specified in the table, σ, represents the true blockage of the grid as well as the encasing frame; N, is the the number of fractal iterations; $\mathcal{L}_0$ and t_0 represent the length and thickness of the 'zeroth' iteration; $R_\mathcal{L}$ is the length ratio and R_t is the thickness ratio such that, $\mathcal{L}_j = R_\mathcal{L}\mathcal{L}_{j-1}$ and $t_j = R_t t_{j-1}$, where j is the scale iteration ($1 \leqslant j \leqslant N-1$). The suffix of the grid naming convention represents the ratio t_0/t_3 for fractal grids and $\mathcal{L}_0$ for regular grids. The grid along with the encasing frame was mounted onto a traverse that ran the length of the working section, to easily change the position of the grid relative to the cylinder.

2.2.2 Grid characterisation

Particle image velocimetry experiments were conducted at various locations downstream of each turbulence generating grid in order to fully characterise the flow (see §2.4.1 for further

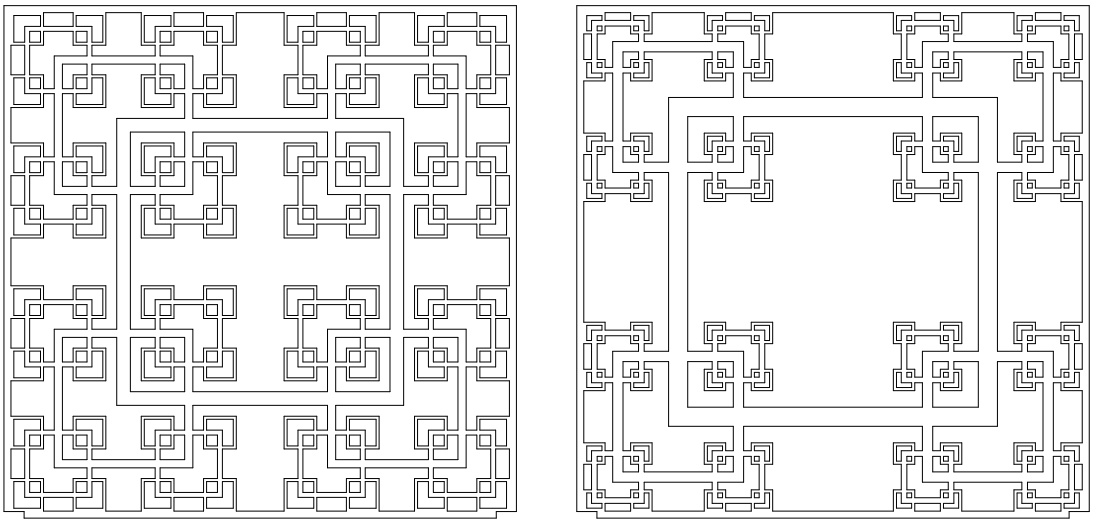

(*a*) SFG 5 (*b*) SFG 7

Figure 2.3: Schematic of turbulence generating grids: (*a*) & (*b*) square fractal grids

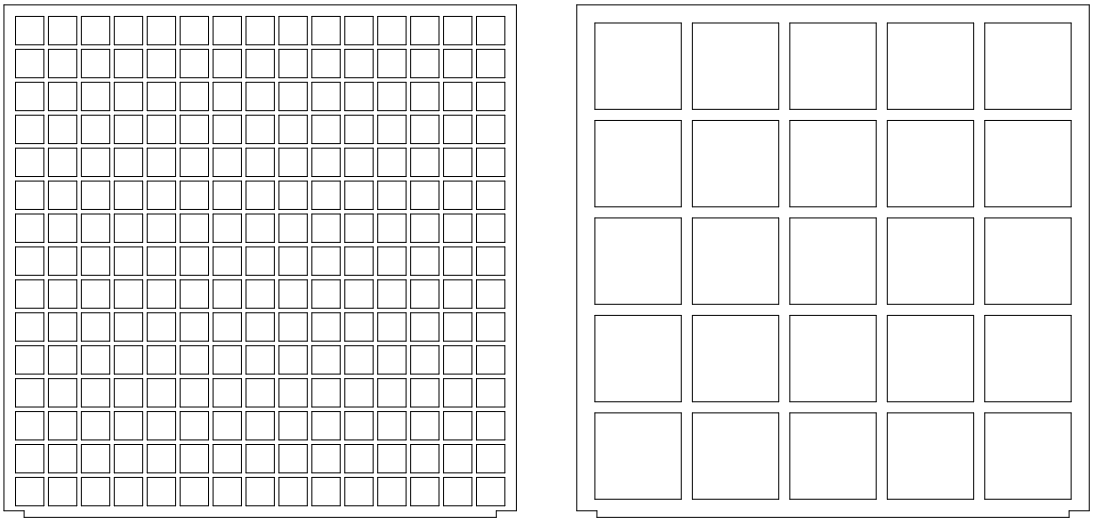

(*a*) SRG 38 (*b*) SRG 111

Figure 2.4: Schematic of turbulence generating grids: (*a*) & (*b*) square regular grids

details regarding PIV). Notably, the integral length scale and the turbulence intensity, which are believed to be most influential in the entrainment process, were evaluated.

Prior to addressing the results of the grid characterisation experiment, it is important to introduce the methodology of how the background turbulence parameters are calculated. Equations 2.1 and 2.2 mathematically define the integral length scale. The transverse auto-correlation function for the streamwise fluctuating velocity is represented by R'_{12}. Note that $r\boldsymbol{e_2}$ refers to some displacement r in the $\boldsymbol{e_2}$ direction, where $\boldsymbol{e_2}$ is a unit vector pointed along the y-direction. The length scale is then calculated by integrating the correlation function from zero to $\hat{r}$, where $\hat{r}$ is the location of the first zero crossing of the correlation function. Figure 2.5(a) depicts the auto-correlation function in the bulk flow in an empty tunnel. Calculating the integral length scale for 'no grid' placed upstream is not straightforward due to the presence of velocity correlation over a large distance, as would be expected for a predominantly laminar flow. However, an estimate for the integral length scale can be calculated by fitting an exponential to the short range correlation peak, producing a length scale estimate, L_{12}, of 3.4 mm. As a comparison figure 2.5(b) depicts a typical auto-correlation function that can be found downstream of a grid in turbulent flow. It should be noted that the length scale, L, may also be calculated in the streamwise direction or using the transverse fluctuating velocity. However, for the purposes of this study, L_{12} will be used to assess the length scale in the background. Finally, equation 2.3 provides a definition for the turbulence intensity. In this equation, u' and v' represent the fluctuating velocity in the streamwise and transverse directions, whereas, U_∞ represents the mean velocity in the free stream subjected to the circular cylinder. It is important to highlight that the fluctuating velocity, the integral length scale as well as the mean velocity subjected to the cylinder were measured through independent grid characterisation runs that were conducted without the cylinder mounted in the flume.

$$R'_{12}(\boldsymbol{x}, r) = \frac{< u'_1(\boldsymbol{x}) u'_1(\boldsymbol{x} + r\boldsymbol{e_2}) >}{\sqrt{< {u'_1}^2(\boldsymbol{x}) >}\sqrt{< {u'_1}^2(\boldsymbol{x} + r\boldsymbol{e_2}) >}} \tag{2.1}$$

$$L_{12} = \int_0^{\hat{r}} R'_{12} dr \tag{2.2}$$

$$TI = \frac{(u'^2 + v'^2)^{1/2}}{U_\infty} \tag{2.3}$$

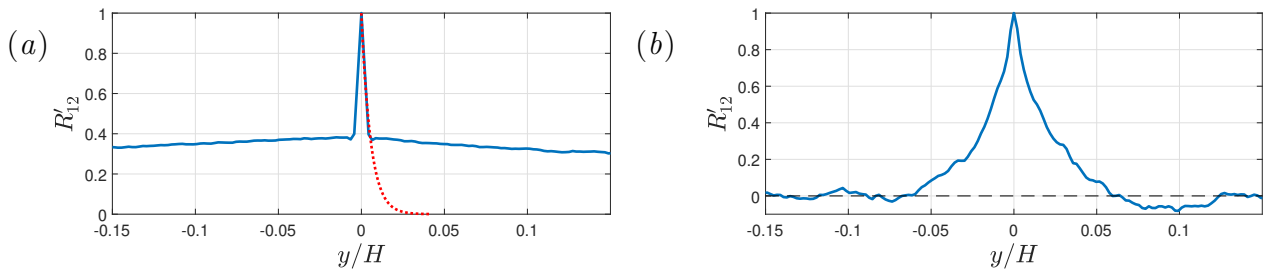

Figure 2.5: Transverse correlation function for streamwise fluctuating velocity. (a) Correlation function in an empty tunnel. Note that the dashed red line represents the exponential fitted to the short range correlation peak. (b) Typical function downstream of a turbulence generating grid. Note, H represents the width of the flume's working section.

It should be noted that a pilot characterisation study examining turbulence generating grids equivalent to the grids characterised in this campaign was previously conducted. This pilot study was conducted at a slightly lower Reynolds number and also with a larger encasing frame. Results of the pilot study are presented in appendix B and informed the locations at which the flow downstream of the grids were measured in campaign I.

Figures 2.6 and 2.7 depict the turbulence intensity field downstream of both regular grids. Figures 2.8 and 2.9 do the same for the used fractal grids, however, due to the significantly larger distance mapped, only a few positions have been depicted. For fractal grids, the production peak occurs at an increased downstream position when compared to a regular grid. This is because the peak in turbulence intensity is associated with the location where the wakes from the largest bars (ie. iteration 0) meet (Hurst & Vassilicos, 2007). This prolonged production and dissipation region allows for more flexibility when attempting to produce desired background turbulence intensity.

Figures 2.10 and 2.11 depict the behaviour of the integral length scale as a function of streamwise distance. Plotted here is the transverse correlation of the streamwise fluctuating velocity, L_{12}, with the probe located at $y/\mathcal{L}_0 = 0$. For the remainder of this thesis, the integral length scale will refer to the scale calculated in this manner, unless specified otherwise. A gradual increase in length scale is observed with increasing streamwise distance. This behaviour is in line with that seen in literature (Comte-Bellot & Corrsin, 1966; Hurst & Vassilicos, 2007).

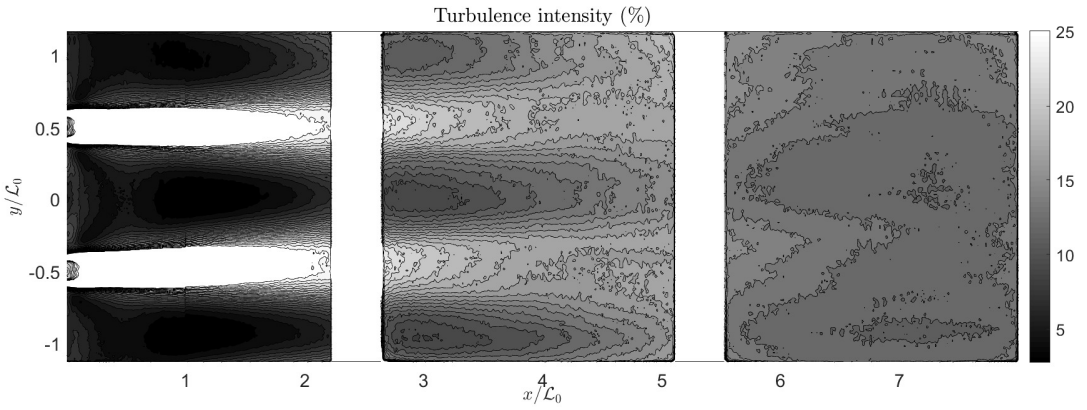

Figure 2.6: Turbulence intensity profile downstream of a square regular grid with $\mathcal{L}_0 = 111$ mm.

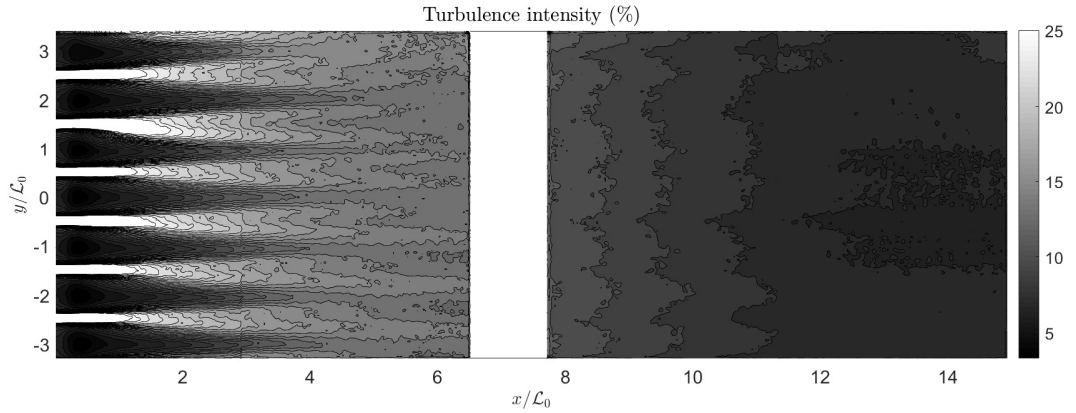

Figure 2.7: Turbulence intensity profile downstream of a square regular grid with $\mathcal{L}_0 = 38$ mm.

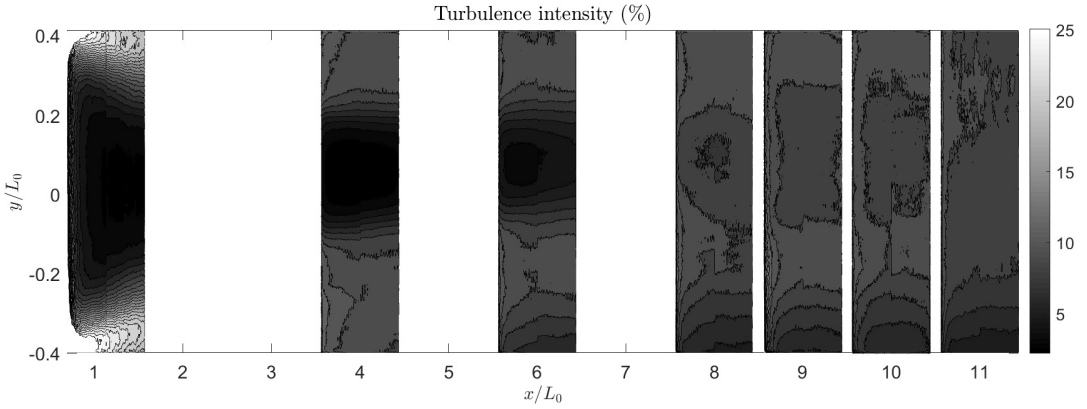

Figure 2.8: Turbulence intensity profile downstream of a square fractal grid with $\mathcal{L}_0 = 312$ mm.

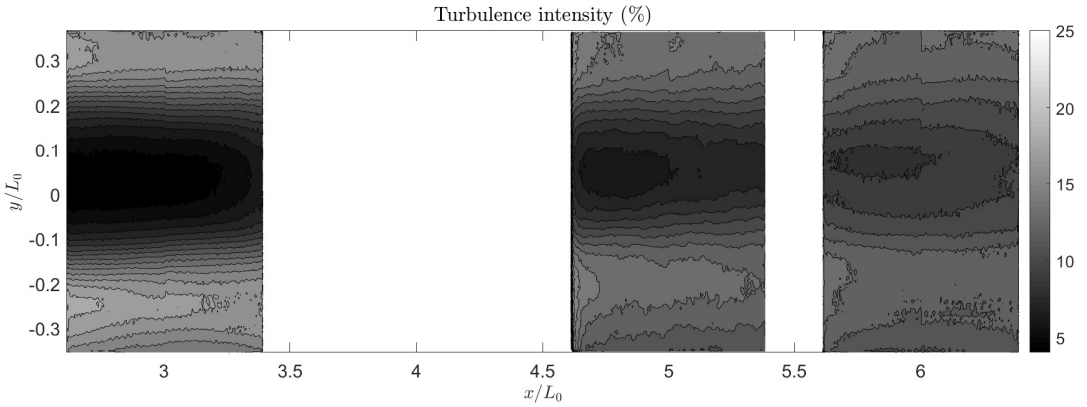

Figure 2.9: Turbulence intensity profile downstream of a square fractal grid with $\mathcal{L}_0 = 354$ mm.

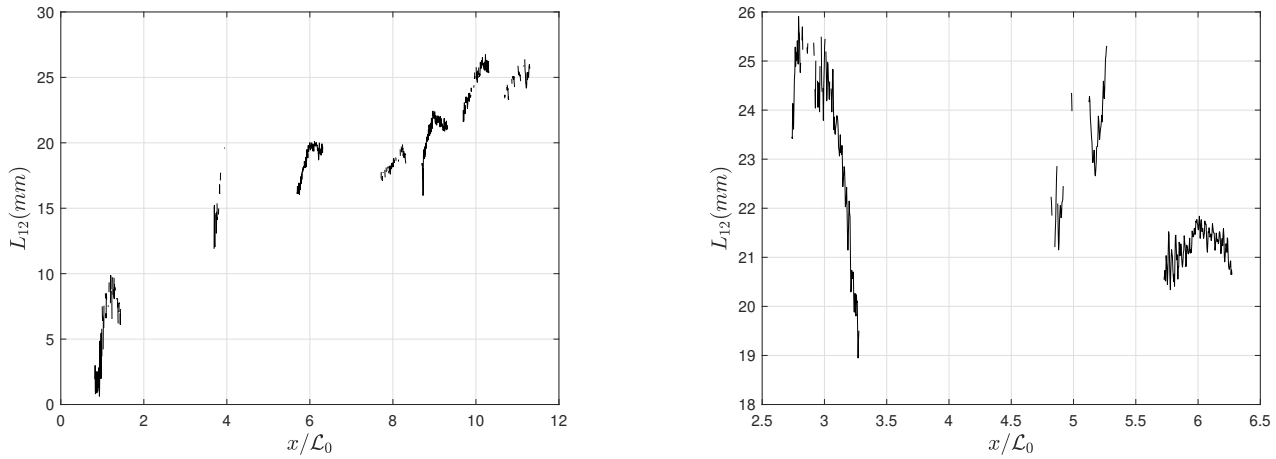

(a) SFG 5 (b) SFG 7

Figure 2.10: Behaviour of length scale as a function of streamwise distance: (a) & (b) square fractal grids.

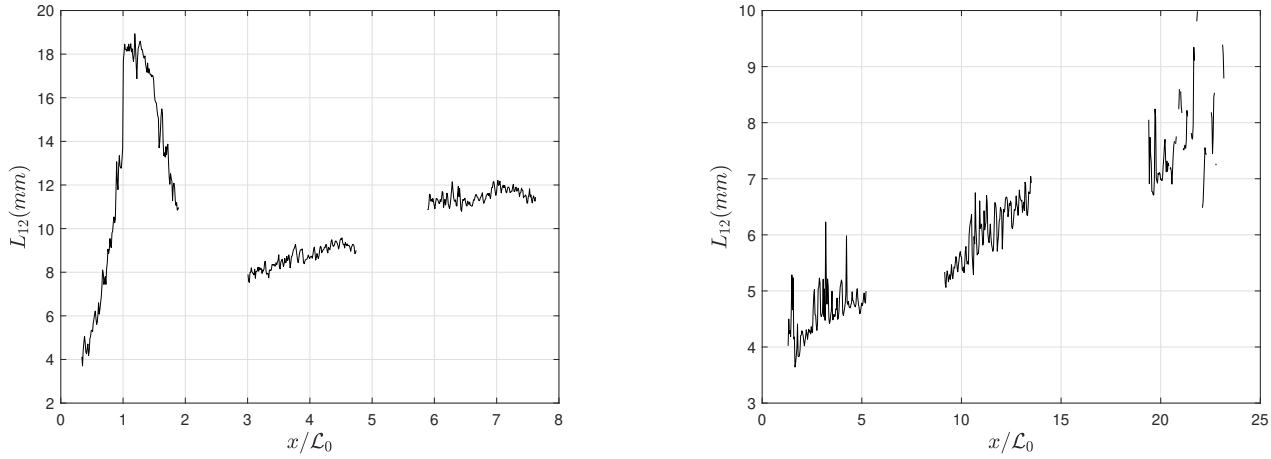

(a) SRG 111 (b) SRG 38

Figure 2.11: Behaviour of length scale as a function of streamwise distance: (a) & (b) square regular grids.

2.2.3 Illumination

Illumination for all experiments conducted in this study was provided by a Nd:YLF high-speed laser operating at 527 nm. Based on the requirements of each experiment, the laser was pulsed at frequencies ranging from 500 Hz to 1500 Hz using trigger signals generated by a digital pulse generator manufactured by Stanford Research Systems. The laser provided 25 mJ of energy per pulse and a periodic variation of 8% was noticed. The beam path was focused using a spherical lens, usually of focal length equating to 750 mm, and then opened into a sheet using a plano-concave lens. Several plano-concave lenses of differing focal lengths were used during the course of this study in-order to produce laser sheets of widths as required for each campaign. In some cases, the flow field was investigated in two separate downstream locations, requiring two distinct laser sheets. This was achieved by passing the beam through a non-polarising 50/50 beam-splitter. The split beams were then separately focused and opened into planar sheets. All of the optics used to manipulate the beams were manufactured by ThorLabs. The majority of the campaigns had the $x - y$ plane illuminated. However, in a single campaign, the laser sheet spanned the cross-stream plane ($y - z$).

2.2.4 Particles

Hollow glass spheres were mixed into the flow to be used as seeding particles for PIV experiments. The nominal diameter of these particles is $10\,\mu$m. Calculating the particle response time based on Stokes flow (τ_p) equates to $6\,\mu$s. For the particles to faithfully follow all the scales of fluid motion, the time scale with respect to the smallest eddies in the flow, the Kolmogorov time scale, τ_η, needs to be such that the Stokes number, $St_p = \tau_p/\tau_\eta \ll 1$. The resulting particle Stokes number was equal to 1.9×10^{-4}, hence indicating that the chosen seeding particles were appropriate.

2.2.5 The use of PLIF as an experimental technique

Researchers have used several methods in the past to detect the location of the turbulent/non-turbulent interface. The signature of a turbulent/non-turbulent interface is the large jump in enstrophy across the boundary. Therefore a threshold on enstrophy is the most commonly found method of interface identification. Some of the other methods that may also be used are highlighted by da Silva *et al.* (2014). These include (a) analysing the probability density functions (PDFs) of vorticity at several points along the edge of the turbulent boundary, whilst searching for a shape change in the PDFs. (Jiménez *et al.*, 2010) (b) Enacting a threshold based scheme on the turbulent kinetic energy. (Chauhan *et al.*, 2014) (c) Using a passive scalar as seen in the study by Westerweel *et al.* (2005). Since the aim of this study is to observe the entrainment behaviour in the presence of background turbulence, it is not possible to rely on enstrophy as a marker to identify the parts of fluid that constitute the cylinder wake. Due to the fact that rotational flow is present on both sides of the wake boundary only (c) is applicable to this study. It is important to note that the passive scalar used must be of a high Schmidt number, Sc, which represents the ratio between the momentum diffusivity and the mass diffusivity. A high Sc ensures that diffusion is restricted to exceptionally small length scales meaning that the scalar faithfully tracks the fluid in the wake. Hence, a high Schmidt number scalar in the form of Rhodamine 6G was injected into the wake from the rear face of the cylinder in order to demarcate the wake from the free-stream. Rhodamine 6G has a Schmidt

number of approximately 2500 in water (Vanderwel & Tavoularis, 2014), making it an ideal candidate for use as a scalar in this experiment.

Pump A Bürket micro dosing unit 7615 was used to pump the fluorescent dye into the wake of the cylinder through a hole, or an arrangement of holes, in the rear face of the cylinder. This arrangement varied depending on the requirements of each experimental campaign and ranged from a single hole for planar PIV campaigns to dual hole arrangements for stereoscopic PIV campaigns and when a splitter plate was used. When an arrangement that required two holes was used, two separate pumps were utilised, each connecting to separate holes. The pumps were discretely pulsed at frequencies ranging from 10 Hz to 20 Hz and were rated to eject 5 µl of fluid per stroke. The resultant ejection velocity was less than 2 % of the local velocity magnitude ensuring an isokinetic dye release into the wake of the cylinder. Furthermore, a long 2 m cable, between the pumping unit and the ejection hole, was used to smooth out the discrete behaviour of the pump.

Tests conducted in a non-turbulent background examining the very near field of the wake that compared the extent of the scalar to the enstrophy distribution, confirmed that the released scalar was well stirred and faithfully marked the entire extent of the wake fluid. Therefore, the use of Rhodamine 6G to perform simultaneous PLIF experiments forms the basis by which the the turbulent interface is identified, and hence the entrainment process is examined during the course of this study.

2.2.6 Cameras

Phantom v641 cameras were used for the entirety of the study. A combination of either two or three cameras were utilised depending on the needs of each campaign. The cameras house a 2560 px × 1600 px CMOS sensor and produced 12-bit images. An internal memory of 32 GB allowed 5475 images to be captured in a single run. All of the cameras were synced with the laser and triggered using the digital delay generator that also triggered the laser.

The PLIF experiment exploits the shifted emission peak of Rhodamine 6G to allow the PLIF camera, along with the help of a low pass filter, to capture the tracer data whilst ignoring any seeded PIV particles. Rhodamine 6G has an absorption peak of 525 nm with an emission peak at a wavelength of 560 nm (Arcoumanis *et al.*, 1990). Therefore, an Edmund Optics low pass filter with a specification cut on frequency of 550 nm was fitted onto the PLIF camera.

Cameras that were used for the PIV experiment were fitted with a ThorLabs bandpass filter centred around 535 nm, to prevent any fluorescent light from the dye affecting the PIV measurements.

Post-processing of all collected PIV images was done through a multi-pass cross-correlation method, which is implemented in the commercial PIV software offered by LaVision, DaVis. A total of three passes with a reducing window size were used to produce instantaneous velocity vectors. Images were also oversampled so that the overlap between two windows was equal to 50%. A minimum peak ratio between the primary and secondary correlation peaks of 1.2, along with a median filter, were applied to reject spurious vectors. Any missing vectors were then interpolated. For all runs, the experimental PIV settings were optimised in order to keep the number of replaced vectors below 3%. Post-processing for the PLIF experiment was done using in-house MATLAB codes.

2.3 Campaigns

During the course of this study, several experimental campaigns were conducted in the flume. The following section outlines the scope of each campaign and also details the main experimental parameters (see table 2.3).

Campaign I - Large scale PIV exploratory study and grid characterisation experiment. The main aim of this campaign was to fully characterise the flow downstream of the manufactured turbulence generating grids. The grids were encased in a custom built frame that allowed them to be mounted onto a traverse that ran the length of the working section of the flume. The

grids were systematically moved along their turbulence production and decay regions. The maximum distance downstream of a fractal grid at which the flow was characterised was equal to 3.5 m. The investigated region for the square regular grids was much shorter, maximising at 0.75 m, since the peak in turbulence intensity downstream of a regular grid is immediately downstream of the grid itself.

Furthermore, initial exploratory simultaneous PIV and PLIF experiments into the near wake of a circular cylinder were also conducted.

Campaign II - An investigation of the wake boundary in turbulent conditions. The far wake of a circular cylinder subjected to background turbulence conditions was investigated using near Kolmogorov-scale resolution experiments. The subjected free-stream turbulence conditions were selected in order to maximise the envelope of turbulence parameters (L_{12} & u'). This campaign aimed to answer the zeroth order question of whether the turbulent/turbulent interface even exists. Secondly, this campaign was also used to investigate entrainment behaviour under turbulent background conditions. This required the ability to track the interface in time, requiring Kolmogorov-scale resolution in both space and time. To this end, a parametric study was conducted that varied each background turbulence parameter independently and thereby, allowed for the decoupled investigation of the effect of each parameter on entrainment behaviour.

Campaign III - Entrainment mechanisms in a turbulent/turbulent interface. The turbulent/turbulent interface was investigated in detail through a simultaneous cinematographic stereoscopic PIV (Ganapathisubramani *et al.*, 2007) and PLIF experiment. This high resolution experiment investigated the far wake of a circular cylinder and aimed to identify the main drivers for the entrainment process within a turbulent/turbulent interface. In order to asses the entrainment mechanisms within the TTI, all three components of velocity as well as all nine components of the velocity gradient tensor were required. This was achieved by invoking Taylor's hypothesis to produce a quasi-instantaneous three-dimensional data-set. The in-plane velocity gradients could be readily calculated using the stereoscopic PIV data. Streamwise ve-

locity gradients were extracted after invoking Taylor's hypothesis. A high temporal resolution along with an induced angle of 45° for the stereoscopic PIV cameras ensured that the uncertainties for all three components of velocity were similar. Ganapathisubramani *et al.* (2007) detail the use of this methodology in a turbulent jet. Figure 2.2 illustrates the experimental setup used for this campaign.

Campaign IV - Near wake development in turbulent background conditions. The aim of this campaign was to explore the differing mechanisms of wake growth that exist in the near wake, a region where the influence of coherent structures is large. Experiments included large field of view simultaneous PIV and PLIF measurements of the flow in the immediate vicinity of the cylinder. The wake growth as well as the spectral signature of the wake in turbulent free-stream conditions was investigated. Another branch of the campaign attempted to assess the influence of coherent structures on near wake entrainment through the use of an 'infinitely' long splitter plate, (Apelt & West, 1975), attached to the cylinder acting as a control experiment.

2.4 Uncertainty

Throughout this thesis, uncertainties have been statistically quantified with the use of confidence intervals on all major results. Experimental uncertainties that exist in both the PIV and PLIF experiments are highlighted in this section.

A note on the three-dimensional nature of the entrainment process At this stage it is important to note that, while the entrainment process is indeed three-dimensional, campaign II examines the process using two-dimensional experiments in a similar fashion to previous studies (Westerweel *et al.*, 2005; Mistry *et al.*, 2016). A two-dimensional experiment is needed to achieve a spatial resolution of the order of a few Kolmogorov scales, which is a necessity to resolve the entrainment process. Furthermore, due care has been taken to reduce the influence of three-dimensional effects, as highlighted in appendix C.4.

Table 2.3: An outline of experimental parameters used for each campaign. N_{aq},f_{aq}, dt, η and τ_η refer to the number of acquired snapshors, the frequency of acquisition, the time separation between exposures, the Kolmogorov length scale and the Kolmogorov time scale respectively.

	Campaign I	Campaign II
	2D-2C - PIV	2D-2C - PIV & PLIF
Model	Phantom v641 (x2)	Phantom v641 (x3)
Lens	Nikor 60 mm f/4 (x2)	Nikor 200 mm f/4 (x2) (PIV) Tokina 100 mm f/5.6 (PLIF)
Viewing area	274.2 mm × 128.8 mm	32.0 mm × 51.3 mm
f_{aq}	5 Hz - 50 Hz	225 Hz ($0.14\tau_\eta$)
dt (PIV)	500 μs - 2500 μs	500 μs
N_{aq}	2000	2676
Spatial resolution (PIV)	2.39 mm	0.49 mm (3η)
Interrogation area	24 px × 24 px	24 px × 24 px
Window overlap	50%	50%
Concentration (μmol l^{-1})	-	400
Flow rate (mg s^{-1})	-	100

	Campaign III	Campaign IV
	2D-3C - PIV & PLIF	2D-2C - PIV & PLIF
Model	Phantom v641 (x3)	Phantom v641 (x3)
Lens	Nikor 200 mm f/5.6,f/8 (x2)(PIV) Nikor 105 mm f/5.6,f/8 (PLIF)	Nikor 50 mm (x3) Nikor 105 mm (x2) (PIV) Nikor 60 mm (PLIF)
Viewing area	32.0 mm × 51.3 mm	300.6 mm × 303.9 mm 152.6 mm × 137.3 mm
f_{aq}	666.6 Hz, 1400 Hz ($0.06\tau_\eta$,$0.03\tau_\eta$)	50 Hz
dt (PIV)	500 μs, 714 μs	1250 μs, 800 μs
N_{aq}	2537, 5076	2537
Spatial resolution (PIV)	0.58 mm (3.6η)	2.85 mm, 1.29 mm
Interrogation area	32 px × 32 px	24 px × 24 px
Window overlap	50%	50%
Concentration (μmol l^{-1})	200	200
Flow rate (mg s^{-1})	100	100

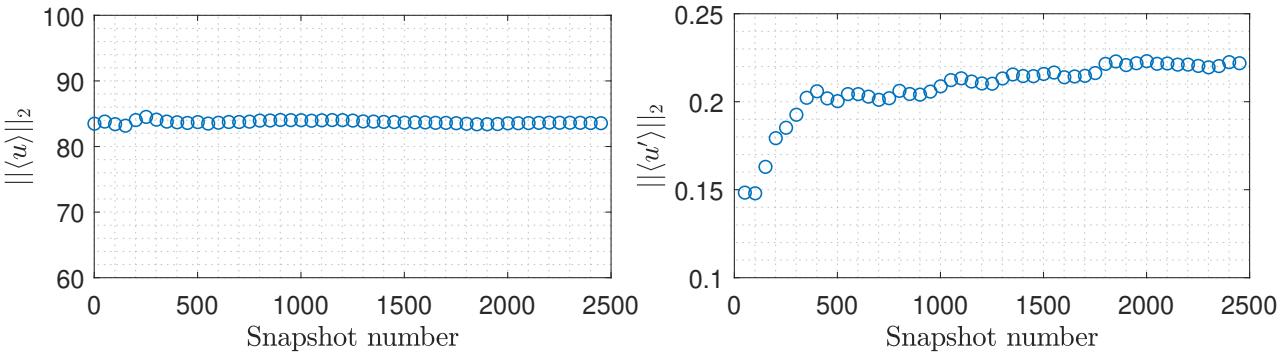

Figure 2.12: Convergence study undertaken for campaign I.

2.4.1 PIV experiment

In certain campaigns, the number of images required to be captured was calculated through a convergence study observing the mean and root-mean-squared (r.m.s.) velocity components. The snapshot number post which the Euclidean norm of the r.m.s. components were deemed to have converged, was used as a guide for the rest of the campaign. Figure 2.12 represents an example of a convergence study undertaken for campaign 1. The r.m.s. component, as expected, converges later than the mean velocity and therefore acts as the limiting factor. In this campaign, the number of snapshots to be acquired, $N_{aq} = 2000$.

Foucaut *et al.* (2004) classify uncertainties into 4 main categories. These follow as, errors that are physical (light sheet, particles and optical), errors that relate to the specificity of the flow (velocity gradient, out of plane motion, seeding etc.), instrumental errors and finally errors that are related to the analysis method. A few of the uncertainties that arise in PIV measurements are described in this section.

The particle image diameter is of importance to the PIV algorithm since, having particles that are too small result in displacements that are biased towards integer values (Raffel *et al.*, 2007). This effect is referred to as 'peak-locking'. Peak-locking is prevented by ensuring the particle diameter is not too small for the three point estimator (Raffel *et al.*, 2007). Westerweel (2000) state that 'peak-locking' can be reduced by ensuring that particle images had a minimum diameter of at least two pixels. This rule was followed during all of the conducted campaigns.

Background noise or background light intensity was kept to a minimum when possible however in the case where a background glow was still present, experiments were only conducted when a significant increase in bit count was observed for the particles. Raffel *et al.* (2007) showed that as long as quantization levels, $QL > 4$ bits per pixel, there was little effect on the r.m.s. error. Initial pilot campaigns that lacked good quality filters for the PIV cameras were subjected to this issue. Without complete removal of scattered light from the ejected dye, the PIV correlation algorithm was left to correlate bright continuous remnants of released dye. This meant that a clear correlation peak for each interrogation window was missing, rather an elongated peak in the form of a ridge transpired, leading to erroneous velocity vectors. The procurement and use of filters that better rejected light scattered from the dye meant that this source of error was alleviated in subsequent campaigns.

Error due to out of plane motion was inherently reduced as a fairly small dt was already in use in the majority of the campaigns. This may be quantified, since w, which is the out of plane velocity component in all but one campaign, was measured in campaign III. The root mean square (r.m.s.) of the out of plane component calculated in the case with the highest background turbulence intensity, equates to $0.096\,U_\infty$. Using the most common dt used during the campaigns, the out of plane displacement of the particles is calculated to be equivalent of 4.8% of the light sheet thickness (1 mm). The noise caused by the out of plane motion was therefore negligible.

Herpin *et al.* (2008) further classify the main sources of error as measurement random error, $\sigma(\epsilon_{int})$, and measurement bias error, $\langle\epsilon_{int}\rangle$. They specify that the r.m.s. error, $\sigma(\epsilon_{int})$ is an order of magnitude larger than the bias error, $\langle\epsilon_{int}\rangle$. Furthermore, they state that the random error must be compared to a lower limit of $\sigma(\epsilon_{int,floor}) = 0.06$ pixels, for an interrogation window size of 32 px × 32 px. Using the lower limit as a baseline, it may be converted to an equivalent velocity and for values taken from campaign II. The uncertainty based on this due to experimental noise is equivalent to 0.61% of the velocity components. Furthermore, this is equivalent to 11% of the r.m.s. fluctuations of the flow. Note that these values are based on a sample run taken from campaign II.

Error in PIV measurements can arise due to various sources, such that their individual contributions can be hard to quantify. However, the cumulative error can be quantified by following the method set out by Romano *et al.* (1999). Their methodology follows that the auto-correlation function spikes at zero displacement of the probe for data gathered in a turbulent flow. The uncertainty may be quantified by comparing the extrapolated velocity variance with the value of the auto-correlation function at zero displacement. Evaluating the error in this manner produces errors that range from 4% to 12% of the r.m.s. velocity fluctuation based on the region of the flow being measured. The higher end of the errors found, arise due to the time separation between PIV exposures, being optimised to measure the highly sheared interfacial and wake regions of the flow.

2.4.2 PLIF experiment

Since the objective of this study is to use the PLIF experiment to demarcate the wake fluid from the free-stream, a quantitative analysis of the scalar is not necessary. Therefore, the main source of error for the PLIF experiment originates from the secondary fluorescence phenomenon. Secondary fluorescence from bright parts of the dye adds a significant "halo" around the dye region, thereby complicating the interface identification. Failure to make considerations for this phenomenon will lead to significant errors in the perceived location of the wake boundary. The secondary fluorescence effect has been combated through two main avenues. Firstly, the concentration and the aperture of the PLIF camera were tuned to ensure significant regions of high intensity scalar were not captured. However, this was not easily possible for the campaigns that observed the flow around the immediate vicinity of the cylinder. The second instrument to reduce secondary florescence errors was to use an aggressive threshold on the boundary identification algorithm. Further details regarding this are provided in §3.2.1.

Chapter 3

Turbulent entrainment in the far wake of a circular cylinder

The work in this chapter has been published: ***J. Fluid Mech*** (2020) 905, A35, "Turbulent entrainment into a cylinder wake from a turbulent background"

3.1 Introduction

This chapter reports on an experimental campaign, (campaign II), conducted in the far wake of a circular cylinder with an aim to investigate the interfacial region between two bodies of turbulent fluid as well as to establish the effects of free-stream turbulence on the entrainment process (see *questions* 1, 2 and 3 in §1.3).

The remainder of this chapter is laid out as follows. The following section (§3.2) details the experimental methodology used. We highlight the process of wake boundary identification in (§3.2.1) along with the verification of the methodology (§3.2.2). §3.3.1 provides details on the behaviour of the interfacial region when subjected to background turbulence and investigates if a turbulent-turbulent interface exists through the use of interface conditioned statistics. Section 3.3.2 analysing the geometry of the wake boundary itself. The entrainment flux calculation as

well as the effects of free-stream turbulence on entrainment behaviour are discussed in §3.3.3. §3.3.4 aims to deduce the relative influences of background integral length scale as well as turbulence intensity on entrainment behaviour. Finally, §3.3.5 provides a scale by scale analysis on the effects of free-stream turbulence on the entrainment process.

3.2 Methodology

The experimental methodology consisted of simultaneous particle image velocimetry (PIV) and planar laser induced fluorescence (PLIF) experiments, and these were conducted in a water flume with a working section length of 9 m and a cross-section of 600 mm × 600 mm, located at Imperial College London. A Reynolds number, based on the diameter (d) of the circular cylinder, Re_d, of approximately 4000 was achieved, hence, placing the flow around the cylinder in the sub-critical regime (Williamson, 1996).

In this investigation, the incoming free-stream turbulence incident on the circular cylinder was produced by turbulence generating grids placed upstream of the circular cylinder. Further details regarding the turbulence generating grids used are provided in §2.2.2. The flow downstream of all four grids was fully characterised and therefore the cylinder could be strategically placed at varying downstream distances so as to independently vary a single parameter in the background turbulence whilst the other remained constant. This followed the methodology of Melina *et al.* (2017).

A fine resolution of approximately 3η (0.49 mm), is necessary to capture the entrainment process in the inter-facial regions as this process is controlled by small-scale dynamics that scale with the Kolmogorov length scale (η).

Simultaneous PIV and PLIF experiments allowed for the scalar boundary to be used to identify the location of the wake boundary, from which conditional statistics were calculated. The process of interface identification is described in the sections below.

3.2.1 Interface identification and treatment

The metric used for interface identification in this study relies on the magnitude of the gradient of light intensity present in the PLIF image. To use a simple light intensity threshold, as is seen in literature, is not sufficient, since doing so assumes a consistent ejection of the dye at the nominal concentration along with a consistent power output from the laser source. These conditions are not usually met and result in a few eddies being illuminated with a greater brightness than others in the same field of view (FOV). Furthermore, a 'halo' effect caused by secondary fluorescence of the dye results in illumination of regions around highly concentrated blobs of the dye. This problem is highlighted and algorithmically resolved by Baj *et al.* (2016). However, due to the nature of this phenomenon the 'halo' regions present a gradual variation in light intensity around bright spots. Hence, to avoid false detections, an identification metric that utilises the light intensity gradient magnitude as its input was deemed to be appropriate. This is mathematically defined as, $|\nabla\phi|$, where, ϕ is the light intensity of the PLIF image. Figure 3.10(a) depicts a typical image and the identified interface. The `contour` function in MATLAB is used to identify the longest continuous contour that satisfies the chosen threshold on the gradient metric. Similar to the interface treatment methodology of Mistry *et al.* (2016), pockets of scalar that are detached from the wake (as seen in the top right corner of figure 3.10(a)) are not considered in any further calculations. The ensemble of points that are used for conditional analysis arrive from regions along an interface contour that satisfy a condition which prevents it from doubling back on itself. For each x-position, the contour is only allowed to exist at a single y location. In the case when multiple y-positions exist for a single x-position, only the data point that is furthest away from the turbulent core is used. This creates an 'envelope' of the interface and defines the ensemble of points used for further analysis.

3.2.2 Methodology verification and threshold selection

As with any study that utilises a threshold based method for interface identification, it is necessary to conduct a sensitivity study in order to appropriately select the threshold that faithfully identifies the interface. Figure 3.1(a) plots the mean value of enstrophy available in

the regions not considered to be part of the wake for respective threshold values. Note that this result is for the test case of no grid, that is a TNTI, where we would expect to find minimal out of wake enstrophy. A jump in this value can be clearly seen in the range of threshold values that lie between -6 and -5. Note that the red line identifies the chosen threshold value of -5. This value is on the aggressive end of the range previously specified. Furthermore, choosing an aggressive yet appropriate threshold is necessary to combat and disregard the effects of secondary fluorescence. In order to further verify that the chosen threshold is appropriate, the conditional jump of enstrophy (ω^2) with respect to the normal distance away from the interface is plotted for several threshold values in figure 3.1(b). The enstrophy plotted in this conditional jump is averaged over the length of the interface present within the field of view (ξ) and also time-averaged over the ensemble of snapshots. Data processed in this manner are denoted with the following symbology, $\langle\rangle_I$. Note that γ represents the coordinate normal to the wake boundary, with positive γ representing the direction into the free stream. This coordinate transform from the laboratory coordinate system to the interface coordinate system is depicted in figure 3.2. The transformed coordinate system is then used in the calculation of all statistics that are conditioned by their distance to the wake boundary. Returning to figure 3.1(b), good convergence is seen in the region of the chosen threshold on the free-stream side of the wake boundary. Most importantly, the sharp jump in enstrophy is captured at the $\gamma = 0$ position, thereby confirming that the wake boundary has been accurately captured by our methodology. Furthermore, the successful implementation of our methodology over all experimental runs conducted in this study can be confirmed by referring to the conditional jump of light intensity (ϕ) with respect to the normal distance away from the interface. This plot is depicted in figure 3.1(c) and highlights the ability of the used methodology to capture the sharp rise in scalar at the $\gamma = 0$ position. After combining this result with that of the conditional enstrophy jump, it is possible to claim that this methodology is robust. Finally, it is to be noted that averaging over ξ is considered appropriate, since it is possible to associate a level of homogeneity with the background turbulence over the size of the field of view. From a Lagrangian perspective, in the far wake one might consider the turbulence to be somewhat "homogeneous" over the distance advected during one eddy turnover time, $\tau \sim L_{12}/u'$, i.e. distance $\mathcal{L}_H \sim U_c\tau$, where U_c is the

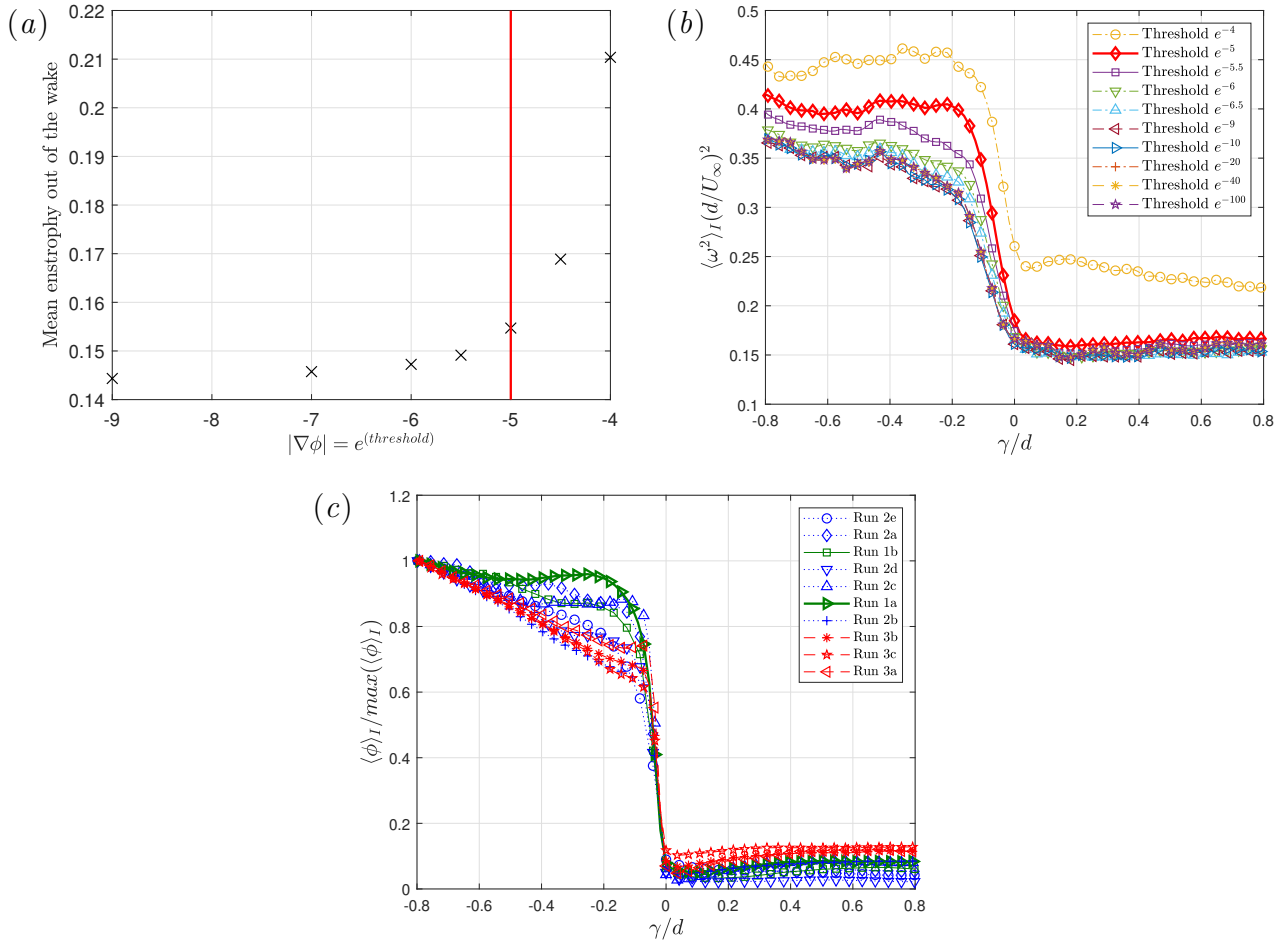

Figure 3.1: Threshold sensitivity study. Note, (a,b) refer to the no-grid case. (a) Plot showing the mean normalised enstrophy considered to be outside of the wake for varying gradient threshold values. (b) The variation of interface conditioned enstrophy jump for various threshold values. The thick red line represents the chosen threshold. Note that the boundary contour is different for each threshold value as the location of the contour is dependent on the threshold. (c) Interface conditioned plot of PLIF light intensity normalised by the maximum value for $-0.8 < \gamma < 0.8$, calculated using the chosen threshold value.

mean convection velocity. Taking $U_c = U_\infty$ and all constants of proportionality to be unity, the "homogeneity length scale" $\mathcal{L}_H$ for all cases is larger than both dimensions of the field of view size ($\sim$ 3cm x 5cm). The smallest correlation distance that occurs in a background turbulence case equates to approximately 7cm. Since this is sufficiently larger than the field of view size, we may be able to claim that the field of view is subjected to a level of homogeneity in all subjected background turbulence cases.

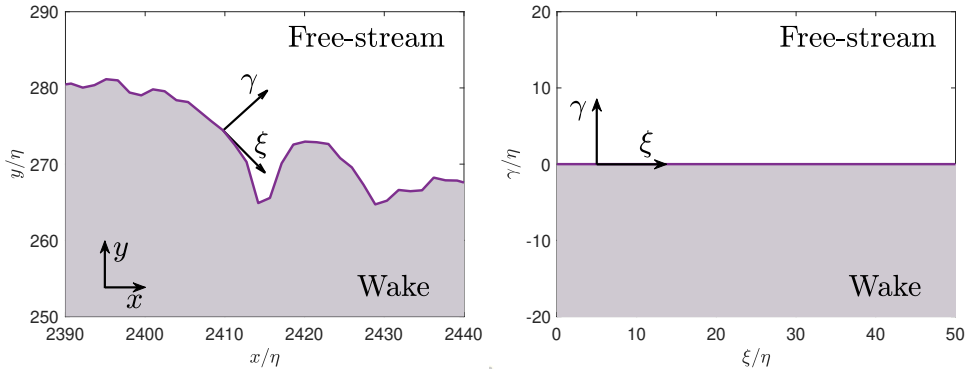

Figure 3.2: Schematic illustrating the coordinate transform employed to evaluate interface conditioned statistics.

3.3 Results and discussions

The effects of free-stream turbulence are twofold. On the one hand, the near field is affected since the shedding mechanism of the cylinder is disrupted by the incoming turbulence (Kwok, 1986; Sadeh & Brauer, 1980). Additionally, L and u' in the free stream, also have a direct effect on entrainment into the wake, downstream of the near-wake region. This chapter will focus on the latter. The near field effect is discussed in chapter 5.

Experiments were conducted in the far wake ($37 \leq x/d \leq 41$) in order to quantify the effects of free-stream turbulence on the entrainment process. Figure 3.3 illustrates the free-stream turbulence parameter envelope of this study. Note that the background free-stream turbulence intensity of the facility is equal to 1.4%, and is representative of the amount of residual turbulence intensity in our control case ('no grid' run 1a). The nine remaining runs span a turbulence intensity, TI, space from 2% to 14%, with length scales varying from 0.3 up to 2.6 cylinder diameters. In addition to describing the parameter space, figure 3.3 also highlights the three main groups that have been distinguished amongst all conducted runs. Runs have mainly been categorised as a result of their entrainment behaviour and also the incoming free-stream turbulence intensity. The characteristics of each of these groups will be discussed in §3.3.3. However, it is useful to introduce these groups at this stage of the thesis. It should be noted that the naming convention used to identify each run indicates both the group the run belongs to, as well as the relative strength of the background turbulence intensity. The former is described by the numeral indicating the group number (run #x). Whereas the strength of

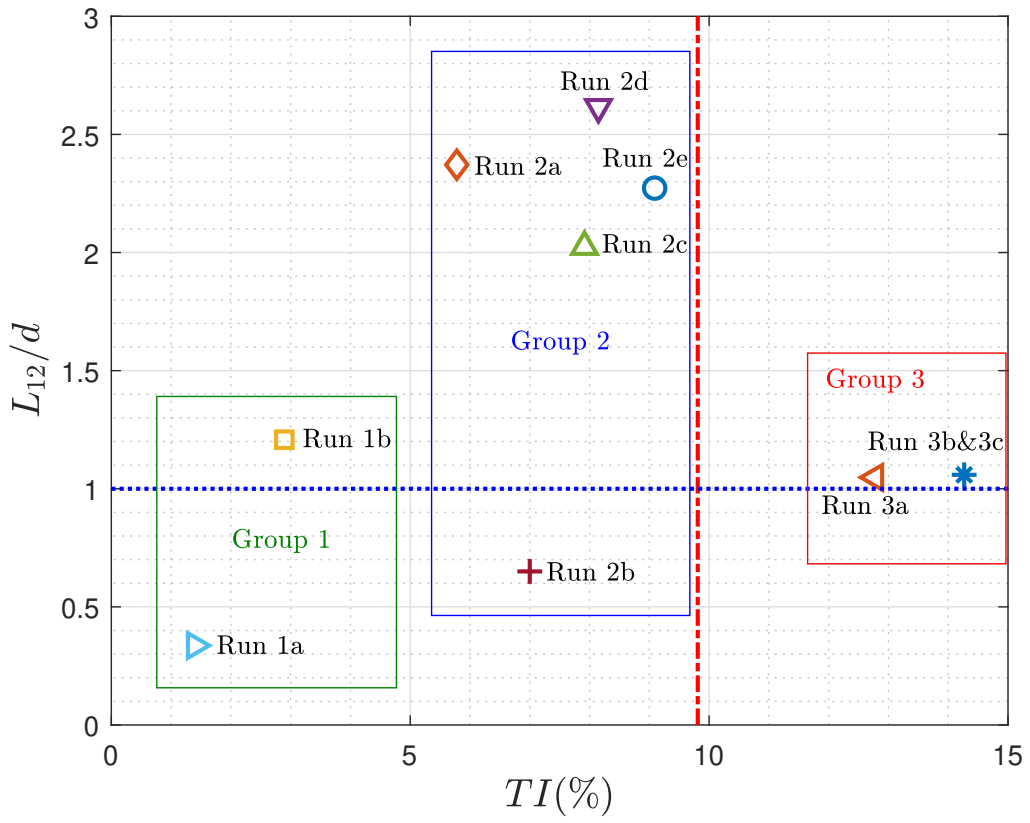

Figure 3.3: Free-stream turbulence parameter envelope. Note that the red dot-dashed line indicates the turbulence intensity near the centreline of the wake in the no-grid case, whereas the dotted blue line indicates a length scale equal to 1 cylinder diameter.

the incoming turbulence intensity subjected to the cylinder is depicted in hierarchical order within each group using a single letter of the Latin alphabet (run #x). It is important to note that the term, 'run #x', is used to define the background turbulence conditions available at the location of the field of view. At any point in this thesis, a reference to a particular run allows the reader to ascertain the available background turbulence conditions.

3.3.1 Evidence for the existence of the turbulent-turbulent interface: Interface conditioned statistics

Figures 3.4 and 3.5 depict interface conditioned statistics as a function of distance normal to the wake boundary (γ). (Note that the wake boundary is analogous to the turbulence/irrotational boundary in the case of a TNTI and is defined as the edge of the scalar extent. It corresponds to

$\gamma = 0$.) As explained in §3.2.2, data presented in these figures are averaged over ξ over the extent of the field of view and also time-averaged over the ensemble of snapshots, thereby represented with the following symbology, $\langle\rangle_I$. Figure 3.1(c) depicts the light intensity in the near vicinity of the wake boundary. The sharp increase in intensity around $\gamma = 0$ indicates a successful implementation of the gradient based interface identification methodology. For all runs the scalar boundary is successfully identified and further used to calculate interface conditioned statistics. Figures 3.4 and 3.5(a), depict mean normalised enstrophy and streamwise velocity as a function of distance normal to the wake boundary. The no-grid control case reproduces expected behaviour for both interface conditioned enstrophy as well as the streamwise velocity jump [1] (da Silva *et al.*, 2014). The base level of enstrophy rests at a non-zero value in the free-stream. This is as a result of the residual free stream turbulence present in the facility. With the introduction of background turbulence, we find that the classical TNTI result of an enstrophy jump at the interface is still present when turbulence is available on both sides of the interface. This is a crucial result as it goes to show that analogous to the TNTI, there exists a turbulent/turbulent interface at which enstrophy adjusts between the two fluid regions. As expected, the base level of enstrophy, as seen on the free-stream side of the interface, increases with added background turbulence intensity. For a majority of the grid turbulence cases, an extension to the magnitude of the enstrophy jump across the interface is seen. When the background turbulence becomes extreme and the intensity becomes greater than that of the wake, as is the case for runs 3a, 3b and 3c, an enstrophy jump is still present and the interface does not break down in a mean sense. Although the magnitude of this jump across the interface reduces in size as a severe increase is observed in the enstrophy available in the free-stream side of the interface.

Figure 3.5(a) depicts the mean streamwise velocity jump across the interface. As long as the turbulence is not too dominant, an increase in the mean shear rate by 40% relative to the no-grid case is observed at the turbulent-turbulent interface. This value represents the mean increase in linear gradients that are evaluated by fitting to data points that reside inside the wake ($\gamma/d < 0$), calculated for runs that lie in groups 1 and 2. When rotational fluid is available

[1] Please note that the thickness of the identified turbulent/non-turbulent interface is discussed in appendix C.3.

on both sides of the interface, we expect the only consistent fluidic 'marker' of the wake to be time-averaged low momentum fluid. However, in runs 3b and 3c this property is no longer seen due to the extreme nature of the free-stream turbulence. Despite the loss of a mean-momentum jump across the interface in these cases, it is interesting to observe that an enstrophy jump is still present even though the turbulence intensity in the free stream is higher than in the wake. The nature of these cases that reside in group 3 will be explained further in the following sections.

The conditional jumps of turbulent kinetic energy are depicted in figure 3.5(b). It is possible to note that none of the jumps are explicitly stronger than the no-grid case. Furthermore, these jumps disappear for the group 3 cases. Therefore, it may be possible to speculate that transport is the major source term of turbulent kinetic energy in the vicinity of the wake boundary, be it pressure strain or turbulent diffusion. However, this is simply speculation at this stage as it lacks requisite evidence.

In a study examining the turbulent/non-turbulent interface, Buxton *et al.* (2019) showed an increase in small-scale anisotropy in the interface region. They examined the behaviour of the anisotropy ratio, Σ, as defined by, $\Sigma = <(du'_\gamma/d\gamma)^2>/<(du'_\xi/d\xi)^2>$ on the turbulent side of the boundary. The velocities represented in this equation are in the interface coordinate system, with u_γ and u_ξ corresponding to the velocity perpendicular to and parallel to the wake boundary, respectively. In isotropic flows this ratio is equal to unity. Hence, any deviation from unity reflects anisotropy in the flow. Figures 4.5(a) and 4.5(b) depict the behaviour of Σ for runs that belong to groups 1 & 2 and group 3, respectively. The no-grid case, as described by run 1a, produces results that are similar to those of Buxton *et al.* (2019), with an increase in anisotropy being observed near the wake boundary on the wake side of the interface. A very gradual increase in the anisotropy ratio is also observed on the free-stream side of the wake boundary, however, the magnitude of this increase in not comparable to the behaviour inside the wake.

Free-stream turbulence cases in both groups 1 and 2 express similar behaviour to the no-grid case, although, the anisotropy level very close to the wake boundary is at a higher level

when compared to the value inside the wake. The asymmetry caused by an increased bias to anisotropy on the wake side of the boundary is maintained in cases that belong to groups 1 and 2. However, this does not apply for group 3 turbulence, as can be seen in figure 4.5(b). A greater level of symmetry is evident in the anisotropy gain on both sides of the wake boundary. This may be expected due to the nature of the highly turbulent ambient flow in these three cases. As will be further explained in §3.3.3, cases in group 3 consider an extreme case of incoming turbulence intensity as they examine the intersection of the cylinder wake with a strong wake created by the turbulence generating grid. The presence of strong turbulent wake-like behaviour on both sides of the wake boundary leads to a symmetrical increase in anisotropy as we approach the boundary. This behaviour is hypothesised to be responsible for the jump in enstrophy that is seen at the wake boundary for all tested cases, even when the intensity in the background is greater than the turbulence intensity inside the wake. This jump is hypothesised to be caused by the strong vorticity-strain interactions that manifest due to the increased anisotropy, which itself is a result of the increased strain rate in the interface normal direction within the vicinity of the wake boundary. The increased local strain rate naturally leads to an increase in the inviscid vortex stretching term of the enstrophy transport equation which can lead to it acting as an additional source of enstrophy which would not exist in a non-turbulent background. Mathematically, the vortex stretching term is defined as, $\omega_i S_{ij} \omega_j$, where, ω_i, ω_j are components of the vorticity vector and S_{ij} refers to the strain-rate tensor. Furthermore, it is highly likely the increase in anisotropy on both sides of the interface is only part of the story. It is not simply the magnitude of the strain-rate tensor, but also the alignment between the strain-rate tensor and the vorticity vector that determines the level of inertial enstrophy production. To show this, Betchov (1956) decomposed the production term as, $\omega_i S_{ij} \omega_j = \omega^2 s_i \left(\hat{\boldsymbol{e}}_{\boldsymbol{i}} \cdot \hat{\boldsymbol{\omega}}\right)^2$, where $\hat{\boldsymbol{e}}$ and $\hat{\boldsymbol{\omega}}$ are unit vectors pointing in the direction of the strain-rate eigenvectors and the vorticity vector respectively. It is then possible to explain that the enstrophy production is determined by the cosines of the alignment angle between the principal axes of the strain-rate tensor and the vorticity vector. In the case of a turbulent/non-turbulent interface, Elsinga & da Silva (2019) show preferential alignment of the vorticity vector and the most stretching strain direction at the irrotational boundary. Watanabe *et al.* (2014) also highlight boosted enstrophy

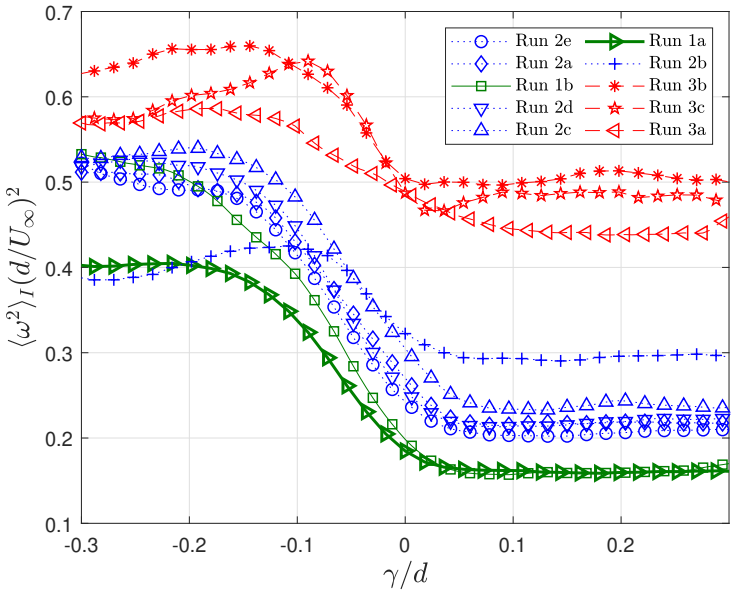

Figure 3.4: Interface conditioned normalised enstrophy as a function of normal distance away from the wake boundary. Note, throughout the manuscript run 1a (in bold) refers to the no-grid case.

production in the vicinity of the interface when turbulent fluid moves toward the TNTI. Bearing this in mind, it is possible to postulate that the vorticity in the wake is more likely 'organised' than in the background, leading to an increased enstrophy production despite the symmetrical anisotropy distribution. This could therefore be the mechanism by which the enstrophy jump is preserved in strongly turbulent background conditions. These ideas are further explored in chapter 4.

3.3.2 Tortuosity

Tortuosity defines the level of contortion of the interface. Mathematically, we define this as the ratio of the length of the wake boundary to the distance between its two ends (see figure 3.7). A sensitivity study to the input parameters reveals the dependence of the tortuosity value on the turbulence intensity. An increase in intensity of the incoming free-stream turbulence resulted in a more tortuous interface. Figure 3.8 displays the scatter with respect to subjected integral length scale and turbulence intensity. Reviewing the probability density functions, PDFs (figure 3.9), shows wider peaks that are shifted to the right in the presence of any

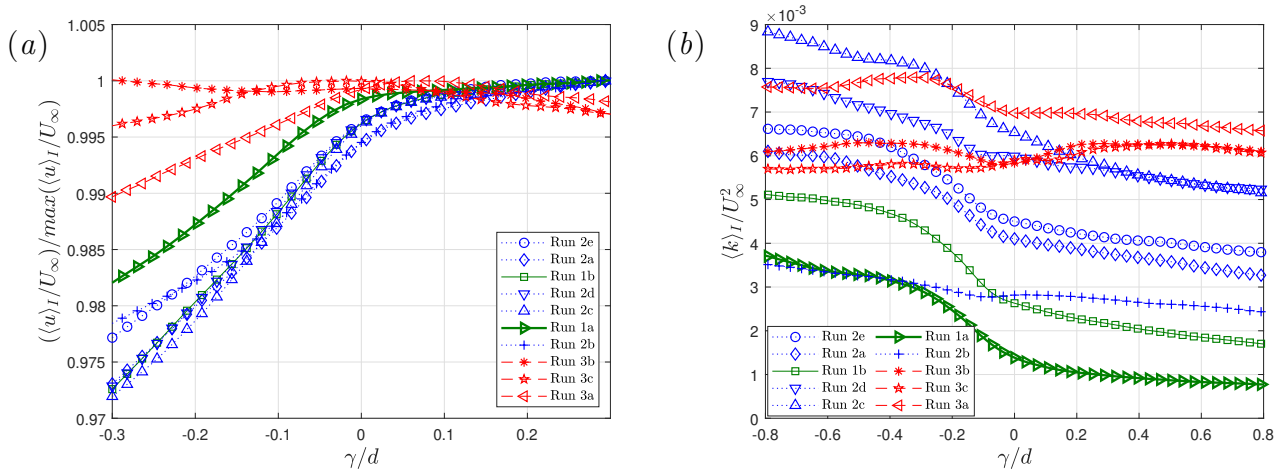

Figure 3.5: Interface conditioned statistics as a function of normal distance away from the wake boundary. (a) Normalised mean velocity; u and U_∞ refer to the streamwise velocity and the streamwise mean velocity, respectively. (b) Turbulent kinetic energy, k, normalised by U_∞^2.

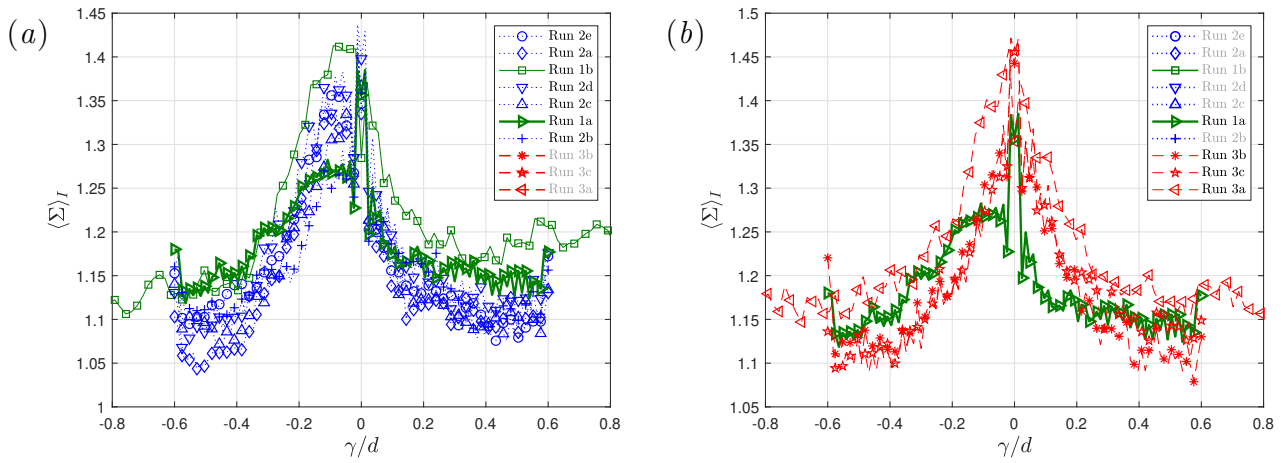

Figure 3.6: Interface anisotropy for turbulence cases in (a) groups 1 and 2 and (b) group 3.

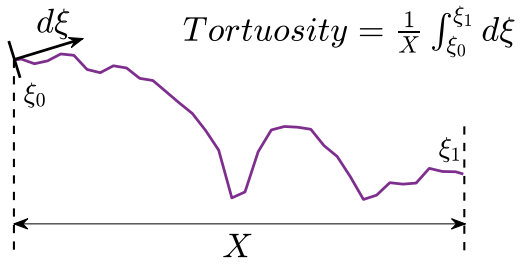

Figure 3.7: Illustration of methodology used to calculate tortuosity.

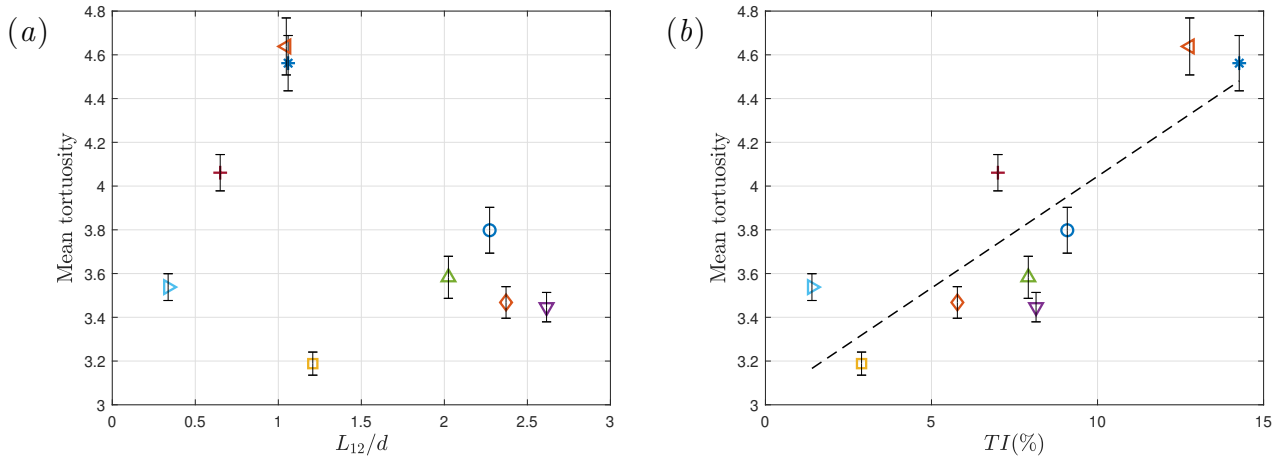

Figure 3.8: Plots depicts the variation of interface tortuosity as a function of subjected turbulence's (a) integral length scale and (b) intensity. The dashed line indicates a linear regression fit. The error bars represent a 95% confidence interval.

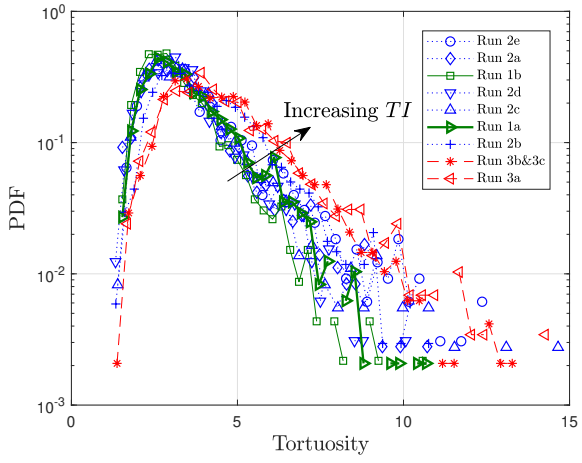

Figure 3.9: Probability density function for interface tortuosity for all subjected turbulence cases.

incoming grid turbulence, highlighting the prevalence of intermittent high magnitude events along with a modal shift towards a higher tortuosity value. Hence, this result goes on to suggest an increased interface surface area with added background turbulence. It is important to note that the tortuosity calculations have been conducted on the 'un-treated' wake boundary. In other words, the conditionality that prevents the contour from doubling back on itself does not apply here. This ensures that the result being presented in figures 3.8 and 3.9 are not unduly biased by any interface treatment methodologies that are in place to facilitate the calculation of the entrainment mass flux.

3.3.3 Entrainment mass flux

The motion of the interface is governed by two distinct phenomena. On the one hand, local fluid advects turbulence in space, whereas fluid from the background is also entrained into the wake, causing it to grow in size. The latter is controlled by the local entrainment velocity, $\mathbf{V}_\gamma$, the calculation of which, requires knowledge of both the time-resolved instantaneous location of the interface as well as the background fluid velocity. The process to evaluate the entrainment velocity is similar to the one used by Mistry *et al.* (2016) and the steps are listed below. Figure 3.10 graphically depicts the process.

1. Local fluid velocity u_0: the local fluid velocity is acquired from the nearest grid point for each point along the contour at time t_0 (see figure 3.10a).

2. Advection subtraction: contour at time, t_1, ($\mathbf{C}_1$), is identified and subtracted for local advection. Each point in $\mathbf{C}_1$ is subtracted by the vector $\Delta t\mathbf{u}_0$, where Δt is the time interval between two snapshots (see figure 3.10b).

3. Entrainment velocity: the normal distance with respect to the original contour, $\mathbf{C}_0$, to the advection subtracted contour, $\mathbf{C}_1 - \Delta t\mathbf{u}_0$, is used to calculate the entrainment velocity. A graphical method, as illustrated by figure 3.10 is used to ascertain the normal distance from each point on the original contour to an interpolated point along the advection subtracted contour. Note: in addition to this graphical approach, a point to point based

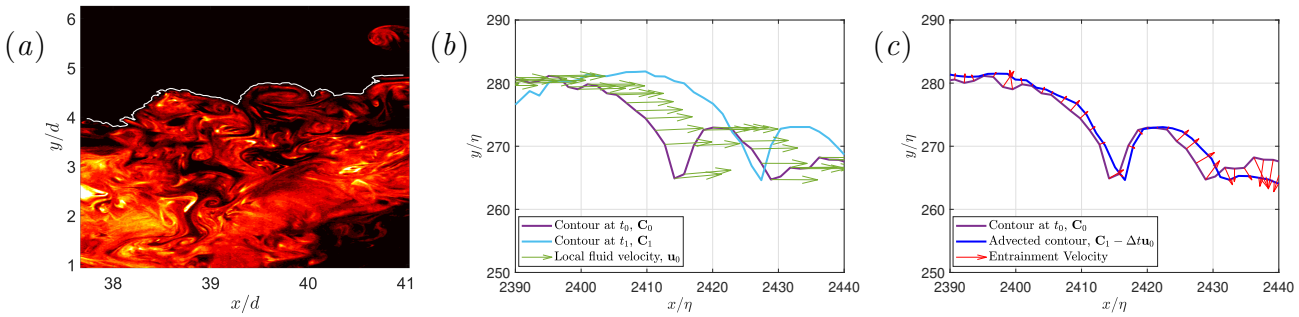

Figure 3.10: (a) A typical PLIF image. The solid white line represents the interface as identified by the gradient metric. (b) & (c) Plots depict the entrainment velocity calculation process. Note that η represents the Kolmogorov length scale. Also note that the (two-dimensional) velocity vectors in (b) & (c) are arbitrarily scaled.

methodology to calculate the entrainment velocity was also trialled and both methods produced comparable results.

Integrating the entrainment velocity along the interface produces a value for the mass flux entrained into the wake (see eqn. (3.1)). Note that this value is normalised by the cylinder diameter, d, and the incoming free-stream velocity, U_∞. Since the fluid in the flume is incompressible, the density term has been neglected from the equation below.

$$Normalised\ Mass\ Flux = \frac{1}{d \times U_\infty} \int_0^s V_\gamma . d\xi \tag{3.1}$$

Entrainment flux is calculated as a mean over the entire ensemble of captured snapshots for each turbulence case and the behaviour is examined against the input turbulence parameters. Figure 3.11(a) depicts the variation of the mean flux with input turbulence intensity. Considering all cases, a negative correlation can be observed, leading to an assertion that an increase in background turbulence intensity acts to reduce the rate at which background fluid is entrained into the wake. This seems to be an unintuitive progression, following on from the tortuosity result. We observe a reduction in entrainment flux despite the increased interface surface area (due to increased tortuosity) when the cylinder is subjected to incoming grid turbulence. This information alone proves that turbulent diffusion is not solely responsible for entrainment in the turbulent-turbulent entrainment paradigm. However, an explanation to this counter-intuitive

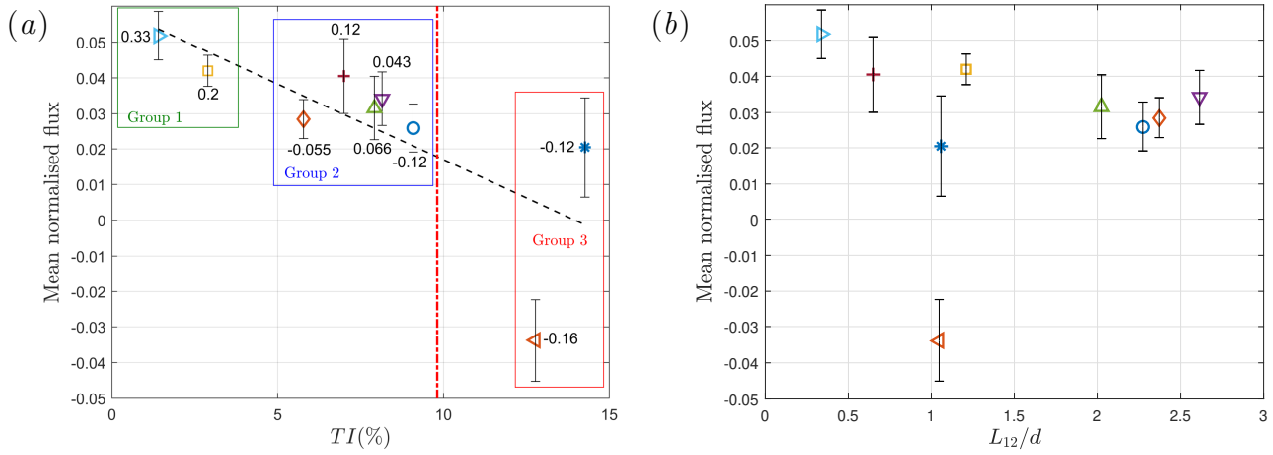

Figure 3.11: Entrainment mass flux as a function of (a) subjected free-stream turbulence intensity and (b) length scale (positive value indicates entrainment into the wake from the background). The dashed line indicates a linear regression fit. Text next to each data point indicates the skewness of the respective dataset.The error bars represent a 95% confidence interval. The red dot-dashed line indicates the turbulence intensity near the centreline of the baseline (no grid) wake.

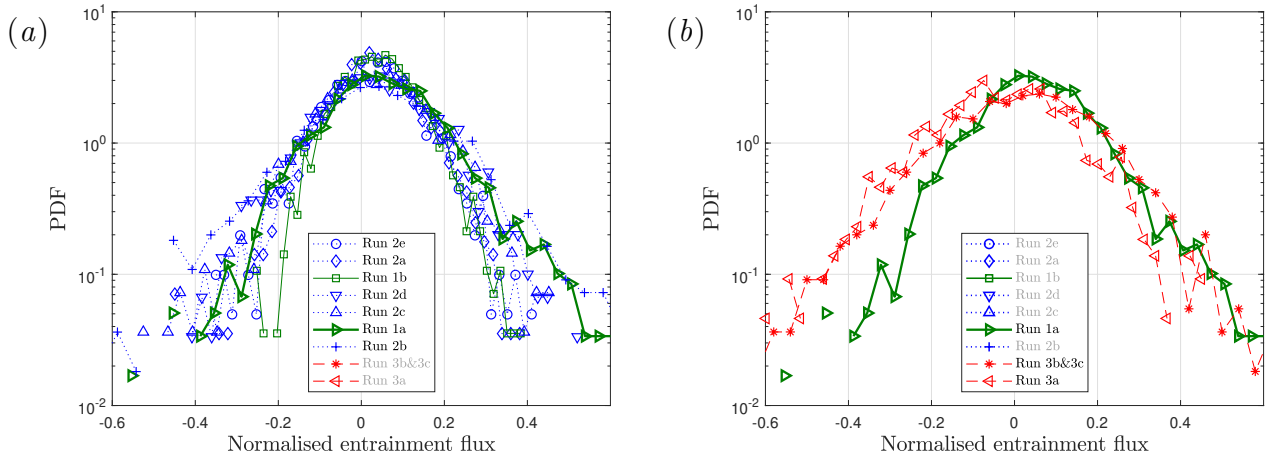

Figure 3.12: Probability density function for entrainment flux for (a) groups 1 and 2 and (b) group 3.

behaviour can be attained by examining the probability density function of the normalised flux (see figure 3.12). The collection of subjected turbulence cases can be split into three distinct groups. Group 3, as highlighted in figure 3.11(a), represents extreme cases of incoming turbulence intensity. These cases have a severely reduced amount of entrainment into the wake, with run 3a displaying net negative entrainment (detrainment). The reduction in net entrainment can be explained by examining the balance between the highly intermittent, positive and negative, extreme entrainment events. A balance between these intermittent events is essential in maintaining a net positive-entrainment rate. Graphically, these events are represented by the tails of the flux PDF, shown in figure 3.12(b). All runs in group 3 witness a substantial boost to powerful negative-entrainment (detrainment) events. Furthermore, in the case of run 3a, there is also evidence of slight suppression of positive extreme entrainment events, which is not present for runs 3b & 3c. The significant amount of background turbulence that is available for cases in group 3 tip this balance towards the negative side. Thereby overcoming the increased amount of entrainment that should be expected due to the increased interfacial surface area, hence resulting in a large reduction in net entrainment. Evidence for such behaviour is also present in the reduced skewness values for both these cases in group 3. It is to be noted that the large amounts of background turbulence results in a wake that is highly intermittent, causing the location of the wake boundary to move significantly in the transverse coordinate. Therefore, due to the particularly small field of view used in this experiment, the sample size of snapshots that capture the wake boundary in full is significantly reduced (the percentage of valid snapshots for run 3a which lies in group 3 is equal to 30%, which is significantly lower than the no grid case that boasts 67% of its total snapshots to be valid. Appendix C.4 details how a snapshot is considered to be valid or invalid.). This phenomenon, along with the large intermittency found in this group, is responsible for the large confidence intervals for this group. Furthermore, it is to be noted that the mean value here is not a fully converged statistic as it will be highly dependent on the number of powerful intermittent events that are captured within the short acquisition time.

When the background turbulence intensity is not as overpowering as in group 3, the behaviour is slightly different. Group 2 presents a slight loss in entrainment, however, the wake still has

a net positive mean entrainment mass flux (see figure 3.11(a)). Observing the PDFs for group 2 as depicted in figure 3.12(a), it can be seen that all cases in this group, with the exception of run 2b, display suppressed right tails. Whereas the left tail remains similar to that of the no-grid case. Furthermore, all cases in this group also present a substantially reduced skewness value. Hence, highlighting a slight shift in balance towards detrainment events, explaining the reduction in mean entrainment mass flux. Note, although run 2b does present a lower mean entrainment value when compared to the no-grid case (run 1a), it does not share the PDF behaviour highlighted above. Additionally, the larger confidence intervals also indicate a larger standard error. Visual inspection of the PLIF images reveals the possibility that both of these characteristics are a result of increased entrainment in the out of plane component.

Finally, group 1 consists of cases that provide a low amount of incoming free-stream turbulence intensity, including the no-grid case. This group is characterised by a large and positive value of skewness and a net positive-entrainment mass flux into the wake.

Runs 3a, 3b & 3c display a negative and a largely reduced mean entrainment flux respectively. This remains a physical result as the geometry of these cases place the field of view in a region that investigates the interaction between two strong wakes. Figure 3.13 displays the turbulence intensity profile downstream of the regular grid as well as the location of the field of view for runs 3b & 3c. All three cases are in the near vicinity ($x/\mathcal{L}_0 < 7$) of a square regular grid, meaning that the wakes shed from the bars of the regular grid have a turbulence intensity that is greater than that of the cylinder wake. Hence, the field of view (FOV) investigates a region where two wakes are competing against each other to entrain fluid from one and another, a process such as this is highly intermittent (c.f. Baj & Buxton (2019)) and results in much greater variation of mean flux. This suggests a larger number of shedding cycles need to be experimentally captured in order to attain convergence. Furthermore, the role of the turbulence intensity level in the wake could be to act as a critical point, beyond which a net mass detrainment is possible.

The behaviour of flux with respect to subjected length scale is much less clear and is seen as a secondary parameter with regards to its influence on entrainment flux. The lack of correlation is

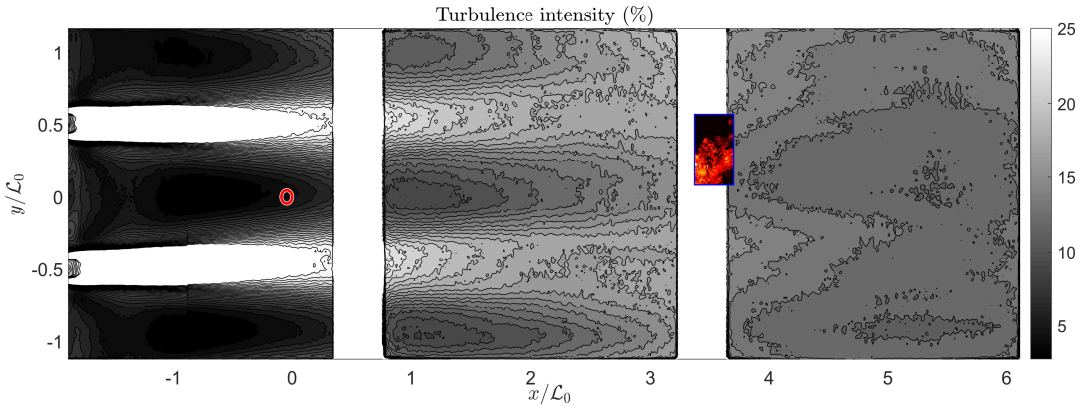

Figure 3.13: Turbulence intensity profile downstream of a square regular grid with $\mathcal{L}_0 = 111$ mm. The overlay represents the investigated FOV. The positioning of the grid, cylinder and the experimental FOV is consistent with that of runs 3b & 3c. Note that similar figures depicting the flow downstream of all grids used in this study can be found in appendix C.1.

evident in figure 3.11(b). The group 3 cases are the most noticeable as they display a significant variation in the mean flux value for nearly the same integral length. This is mainly down to the extreme background turbulence that these runs are subjected to. The large observed variation in flux for these group 3 cases is due to the lack of convergence, as explained in the previous paragraph.

3.3.4 Turbulence parameter

Several investigators in the past have used the turbulence parameter in an attempt to reconcile the effects of both length scale and turbulence intensity in a single form. A slightly modified version of the original parameter initially used by Taylor (1936), is

$$T_p = (TI)^m \left(\frac{L_{12}}{d}\right)^n \tag{3.2}$$

Running an optimisation algorithm to calculate the best linear correlation between T_p and mean normalised flux produces the coefficients, $m = 1.28$ & $n = -0.11$. An increase of only 2% in the coefficient of determination is achieved when comparing it to a linear fit based on the turbulence intensity alone. Therefore, it is clear to see that the dependence of entrainment behaviour in the far-wake region is mainly on turbulence intensity of the incoming free-stream

turbulence. The optimal coefficients clearly encourage the influence of TI, whilst providing only a weak inverse correlation to L_{12}. Hence, this clears the hazy dependencies suggested in previous literature.

3.3.5 Multi-scale effects of free-stream turbulence

The box counting method (Mandelbrot, 1983) was utilised to investigate the scale by scale behaviour of the wake boundary under the influence of incoming free-stream turbulence. This method involves counting the number of boxes that are covered by a contour in a range of grids with increasing box sizes. Figure 3.14(a) presents results of the box counting method for the wake boundary. Note that Δ represents the length of one side of the square box. It was previously shown that an increase in the intensity of the background turbulence leads to an increased interfacial tortuosity. With respect to group 3, figure 3.14(a) shows an increase in length of the wake boundary as a result of the background turbulence occurs at all length scales and no single part of the spectrum is especially affected. It can also be seen from figure 3.14(a) that runs in groups 1 and 2 remain similar to the no-grid case with respect to the length of the wake boundary. The gradient of this plot can be used to evaluate the fractal dimension. Fractal dimensions lie between 1.14 and 1.23 for all runs and tend to increase with increased background turbulence intensity (figure not shown for brevity). Note that these values are similar to a fractal dimension of 6/5 that has been previously reported by Zhou & Vassilicos (2017) and Breda & Buxton (2019) for TNTIs.

In order to establish the effects of free-stream turbulence on entrainment on a scale by scale basis, a multi-scale analysis based on filtering of the high resolution dataset was conducted. A methodology inspired by that of Mistry *et al.* (2016) was implemented to do the same, which is illustrated in figure 3.15. The spatial filtering of the velocity data was conducted as per the procedure of Philip *et al.* (2014). The velocity fields were spatially filtered using box filters in the range $0.02d \leq \Delta \leq 0.60d$. With respect to the Taylor length scale (λ) calculated using the no-grid case, the box filter sizes were in the range $0.1\lambda_{no\ grid} \leq \Delta \leq 2.6\lambda_{no\ grid}$. Note that the Taylor scale has been calculated using the following expression, $\lambda_{no\ grid} = \sqrt{10\nu k/\varepsilon}$, where

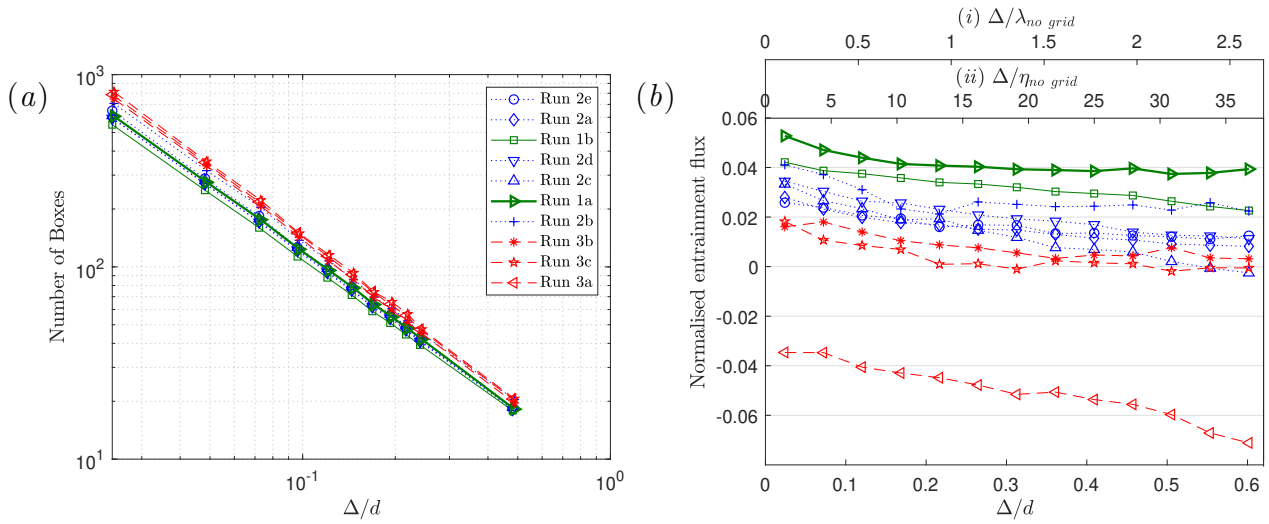

Figure 3.14: Multi-scale analysis. (a) Number of boxes covered by the wake boundary as a function of the box size used. (b) Scale by scale normalised entrainment flux. Note, the two axes on the top of the plot represent the filter size normalised by (i) the Taylor length scale (λ) and (ii) the Kolmogorov length scale (η) found inside the wake, when calculated for the no-grid case.

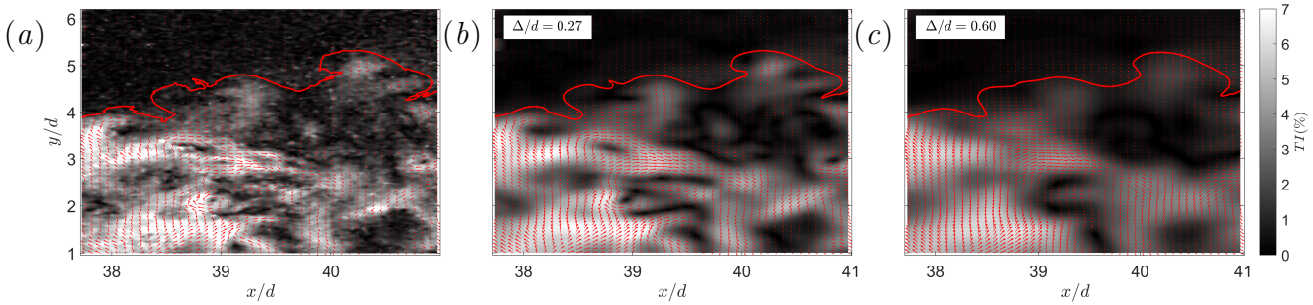

Figure 3.15: Illustration of the filtering process conducted for the multi-scale analysis. Plots depict the turbulence intensity field superimposed by velocity vectors and the wake boundary for the no-grid case. Note that only one in three velocity vectors are displayed for clarity. (a) Unfiltered (b) Filter size, $\Delta/d = 0.27$ (c) Filter size, $\Delta/d = 0.60$

k is the turbulent kinetic energy and ε is the dissipation rate calculated using an assumption of local axisymmetry. To obtain the quoted value, the equation is averaged both spatially and temporally for all points that lie inside the wake. Furthermore, the wake boundary, as identified from the unfiltered PLIF light intensity data, was filtered using a moving average filter of span, Δ, to produce a filtered wake boundary. Examples of the filtered velocity fields superimposed by the filtered wake boundary can be found in figure 3.15 for three different filter sizes. Figure 3.15(a) depicts the unfiltered case, whereas figures 3.15(b), 3.15(c) show the same for increasing filter sizes. Upon conducting the spatial filtering, the entrainment mass flux relative to the filtered wake boundary was calculated in the same manner as described in §3.3.3 and the scale by scale flux result is depicted in figure 3.14(b). Firstly, examining the no-grid case, the mean entrainment mass flux remains at a constant level across the range of scales with a slight drop being witnessed at the smallest scales. This result correlates well with the analysis of Mistry *et al.* (2016) and demonstrates a largely constant rate of entrainment across all length scales. The remaining runs in groups 2 and 3 do show a gradual yet slight reduction in normalised entrainment flux as filter size is increased. However, in the global picture, this slight reduction is not significant when compared to the turbulence effect on entrainment and it is safe to say that the free-stream turbulence affects entrainment through all scales and is not limited to the energy containing scales. This perhaps explains the weak dependence of the total entrainment flux on the integral length scale of the free-stream turbulence.

3.4 Conclusions

The effects of length scale and turbulence intensity in the background turbulence on the entrainment process as well as the bounding interface were evaluated using simultaneous PIV and PLIF experiments conducted in the far wake of a circular cylinder. The classical result from turbulent/non-turbulent interfaces of an enstrophy jump at the interface can still be seen when turbulent rotational fluid is available on both sides of the interface, therefore proving the existence of the turbulent/turbulent interface, something that was questioned in the review of da Silva *et al.* (2014). Additionally, background turbulence does act to increase the shear rate

at the interface as long as the incoming turbulence is not too overpowering (does not reside in group 3). Furthermore, it was found that the entrainment process is largely sensitive to turbulence intensity of the incoming grid turbulence. An attempt to collectively analyse the effects of length scale and turbulence intensity through the use of the turbulence parameter resulted in power coefficients that greatly promoted the influence of TI, whilst being inversely correlated in a weak manner to L_{12}. We thus clear the hazy dependencies as suggested in the literature, showing that background turbulence intensity is the dominant parameter in influencing entrainment behaviour in the far wake.

Despite the presence of background turbulence leading to an increase of interface surface area, a net reduction in entrainment flux is observed with increased background turbulence intensity. By showing that an increased level of background turbulence concurrently leads to an increased interface surface area yet also a reduced entrainment rate, it was possible to discount the process of turbulent diffusion as being solely responsible for entrainment in the TTE paradigm. Rather, the reduction in entrainment was found to be an action of high intermittency. This was mainly through the stimulation of large, intermittent, but infrequent detrainment events that reside in the left tail of the mass flux PDF, as well as a suppression of similar net positive-entrainment events. In the most extreme case, where the background itself consisted of a strong wake, net detrainment was found to occur. The increase in entrainment that could be expected for the increased interfacial surface area is overbalanced towards the detrainment side by the highly infrequent yet highly powerful entrainment and detrainment events. The altered entrainment behaviour when free-stream turbulence intensity is greater than that of the wake itself is similar to the behaviour noticed by Ching *et al.* (1995) in the case when applied background turbulence intensity was comparable to the plume convective velocity. Finally, it was found that the influence of free-stream turbulence on entrainment behaviour is not just limited to the energy containing length scales, instead the effect is seen across all length scales thus justifying the weak dependence on L_{12} and showing that turbulent/turbulent entrainment is truly a multi-scale phenomenon.

Chapter 4

Turbulent/Turbulent interface

The work in this chapter was presented at the iTi conference conducted in 2021. Part of the work presented in this chapter has been published as a book chapter: ***Progress in Turbulence IX. iTi 2021*** (2021), Springer Proceedings in Physics, vol 267, "Turbulent/turbulent entrainment". The majority of the work in this chapter is under revision with ***J. Fluid Mech.***, under the title, "On the Physical Nature of the Turbulent/Turbulent Interface".

4.1 Introduction

In the previous chapter, free-stream turbulence was shown to decrease the mean entrainment mass flux into the far wake of a circular cylinder relative to the non-turbulent case. The rate and process by which this entrainment occurs is governed by small-scale turbulent dynamics within an interfacial layer adjacent to the outermost boundary between the two regions of fluid. This chapter aims to investigate the mechanisms by which this entrainment process occurs. In the special case where the background fluid is non-turbulent this layer is known as the turbulent/non-turbulent interface (TNTI).

The nature of the TNTI is best explained by examining the behaviour of the terms of the

enstrophy budget equation (see eqn. (4.1)) (Pope, 2000).

$$\frac{\mathrm{D}}{\mathrm{D}t}\frac{\omega^2}{2} = \omega_i\omega_j s_{ij} + \nu\frac{\partial^2(\omega^2/2)}{\partial x_j \partial x_j} - \nu\left(\frac{\partial \omega_i}{\partial x_j}\right)^2 \tag{4.1}$$

A key distinguishing feature of turbulent flow is that it is vortical, i.e. $\omega^2 = |\nabla \times \boldsymbol{u}|^2 \neq 0$, where $\boldsymbol{u}(\boldsymbol{x})$ is the velocity field and $\boldsymbol{\omega}$ is the vorticity, whereas non-turbulent flow is usually irrotational, $\omega^2 = 0$. Accordingly, the outermost boundary between the turbulent and non-turbulent fluid, the irrotational boundary, is an iso-surface of $\omega^2 = 0$. Corrsin & Kistler (1955) thereby first postulated the existence of a viscous superlayer at the outer edge of the TNTI. They argued that inside the superlayer, the viscous diffusion term of the enstrophy budget equation, $\nu\frac{\partial^2(\omega^2/2)}{\partial x_j \partial x_j}$, solely dominates and hence viscosity takes complete responsibility for enstrophy $(\omega^2/2)$ production and facilitates the transfer of vortical motions to the surrounding fluid. This is necessitated by the fact that $\omega^2 = 0$ at the irrotational boundary ensuring that the inertial vortex stretching term $\omega_i\omega_j s_{ij}$ must drop to zero here. Viscosity thus remains the only method by which vorticity may be transferred to the irrotational background, thereby growing the turbulent flow via entrainment.

Using dimensional arguments, Corrsin & Kistler (1955) further deduced that the thickness of this layer, where vorticity is diffused into the surrounding fluid, must scale with the Kolmogorov length scale and furthermore, the defining velocity scale in this region is the Kolmogorov velocity scale. Here the Kolmogorov length η and velocity u_η scales characterise the smallest, dissipative motions in turbulence and are formed from the rate of dissipation of turbulent kinetic energy per unit mass ε and kinematic viscosity of the fluid ν, i.e. $\eta = (\nu^3/\varepsilon)^{1/4}$ and $u_\eta = (\nu\varepsilon)^{1/4}$. Many years later, these scalings were experimentally verified by Holzner & Lüthi (2011).

The TNTI is considered to encompass the layer of fluid in which the enstrophy adjusts from zero, in the background, to the bulk value within the turbulent flow in a conditional mean sense. Many subsequent studies have shown the TNTI to be substantially thicker than simply the viscous superlayer (da Silva *et al.*, 2014; Van Reeuwijk & Holzner, 2013). Once the enstrophy level within the TNTI becomes non-negligible the inertial vortex stretching term $\omega_i\omega_j s_{ij}$ takes over as the dominant source of enstrophy production (da Silva *et al.*, 2014; Watanabe *et al.*,

2014). Van Reeuwijk & Holzner (2013) coined this region of the TNTI the turbulent buffer layer and defined the thickness of the viscous superlayer to be the point at which the enstrophy production via viscous diffusion decays to insignificance. Throughout the TNTI the viscous dissipation acts as a constant sink of enstrophy.

Whilst the behaviour of these terms and their contribution to turbulent entrainment is well established for a TNTI, an understanding of the mechanisms of entrainment is lacking when rotational fluid is present on both sides of the bounding interface, despite the fact that the majority of environmental and industrial flows occur within a turbulent background. The literature is scarce and the physics of the turbulent/turbulent interface (TTI) are as yet unknown.

This gap in the knowledge left behind some profound questions which we aim to address in this chapter. This chapter builds on the work reported in chapter 3 and aims to investigate the physics of the turbulent/turbulent interface. In the case of turbulent/turbulent entrainment the intuition of Corrsin & Kistler (1955) breaks down, since a TTI is unlikely to be an isosurface of $\omega^2 = 0$ and hence all three source terms on the right hand side of eqn. (4.1) are non-zero, including the inertial vortex stretching term. Answering this question is vital to more accurately modelling turbulent flows spreading into a turbulent background since existing modelling strategies are often based around the assumption that diffusion plays the dominant role.

An experimental campaign was conducted to analyse the turbulent/turbulent interface (TTI) in detail with an aim to understand the physical processes that exist in the vicinity of the interface. In a similar vein to campaign II, a parametric study was conducted in the far wake of a circular cylinder that is subjected to cases of grid-generated background turbulence, in which the length scale, L_{12}, and intensity, TI, of the background turbulence were independently controlled. Simultaneous, cinematographic stereoscopic particle image velocimetry (PIV) (Ganapathisubramani *et al.*, 2007) and planar laser induced fluorescence experiments (PLIF) were conducted approximately 40 diameters downstream of the rear face of the circular cylinder. In order to examine the interface it is necessary for the experimental setup to achieve a near Kolmogorov scale spatial resolution. A combination of a 12mm extension tube mounted

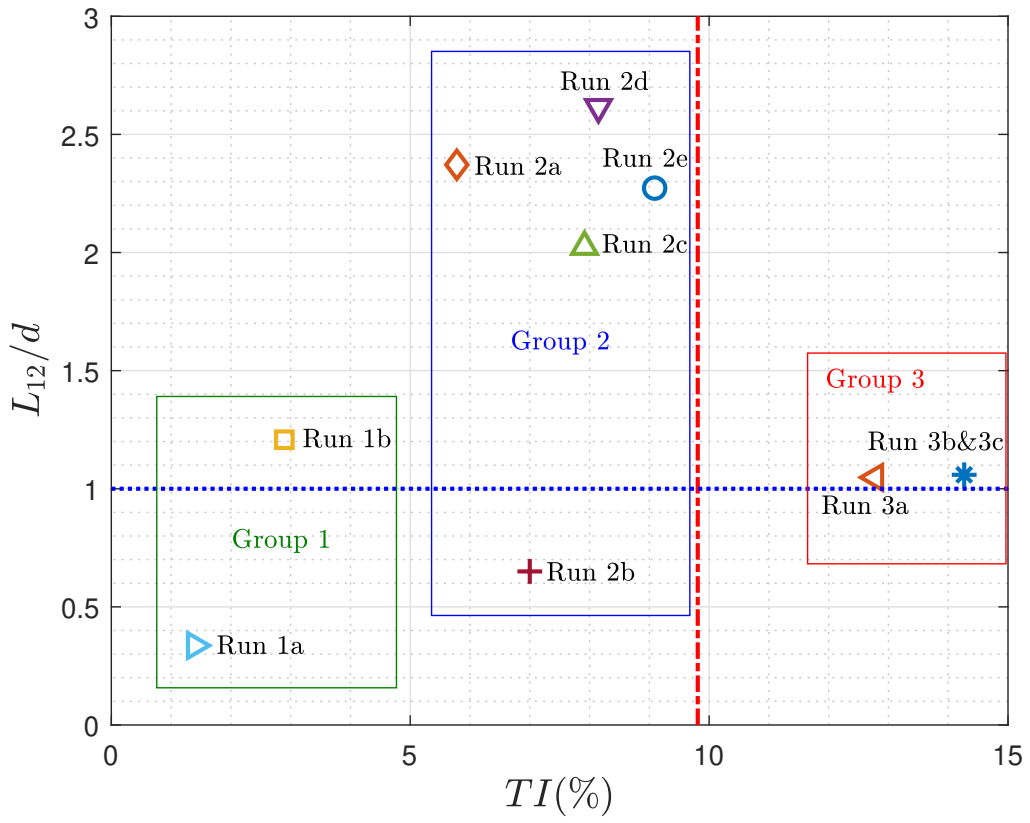

Figure 4.1: Experimental envelope of the campaign highlighting the background turbulence parameters for all conducted runs. Note that the blue dotted line represents a value equal to one cylinder diameter. The red dot-dashed line indicates the turbulence intensity found inside the wake for the no-gird case at the location of the field of view.

onto a Nikkor 200mm lens was utilised to achieve a spatial resolution of approximately 3.6η which is comparable to direct numerical simulation (DNS) resolution. An illustration of the setup used in the experimental campaign is depicted in figure 2.2. Runs conducted in this campaign, (campaign III), exactly matched those from the previous campaign and therefore this particular campaign shares the same parametric envelope. This experimental envelope has been reproduced in fig 4.1 in-order to aid the reader. Further details regarding the naming convention used are provided in §3.3.

4.1.1 Divergence correction

As with any experimentally obtained data-set for an incompressible flow, a non-zero divergence error, i.e. $\nabla \cdot \boldsymbol{u} \neq 0$, exists within the raw data. A divergence correction scheme as laid out

by de Silva *et al.* (2013) was implemented on the data-set. A brief summary of the scheme is given below. The scheme utilises an optimisation algorithm, which aims to minimise the level of added noise to the velocity components whilst maintaining the $|\nabla \cdot \boldsymbol{u}_c| < \mathcal{X}$ constraint, where $\mathcal{X}$ is a user defined tolerance. Note that u_c refers to the corrected velocity. Equation 4.2 defines the objective function that is to be minimised, where $\boldsymbol{u}_e$ is the experimentally measured velocity.

$$F = \frac{1}{N} \sum_{\text{allpoints}} \left[(u_{1_c} - u_{1_e})^2 + (u_{2_c} - u_{2_e})^2 + (u_{3_c} - u_{3_e})^2 \right] \tag{4.2}$$

The divergence was calculated using a second order finite difference scheme and at the boundary of the spatial domain, a first-order scheme was utilised. The finite difference equations were rearranged into a linear system and added as a constraint to the solver. A threshold on the divergence error of 10s^{-1} was placed. The divergence correction scheme was implemented using in house MATLAB codes and the optimisation was conducted using a constrained non-linear multi-variable solver, *fmincon*. The optimisation was done over several overlapping pseudo-volumes each 7 snapshots in size. The scheme was successful in significantly reducing the divergence error whilst ensuring that the magnitude of the "correction noise",

$$\frac{\langle |(\boldsymbol{u}_c - \boldsymbol{u}_e)| \rangle}{U_\infty} < 1\%, \tag{4.3}$$

added to the data-set was below 1% of the mean free-stream velocity, i.e. to within the existing experimental uncertainty. All of the results presented in this chapter have been calculated using data-sets that have been corrected for divergence error.

4.2 Entrainment mechanisms within the TTI

The turbulent/turbulent interface is now further investigated through the lens of the enstrophy budget equation (see eqn. (4.1)) to ascertain the relevant flow physics. Analysis of this manner

for turbulent/non-turbulent interfaces can be found in previous literature (e.g. Van Reeuwijk & Holzner (2013); Buxton *et al.* (2019); Silva *et al.* (2018)). The outer edge of the viscous superlayer in a turbulent/non-turbulent interface is defined as an enstrophy iso-surface of $\omega^2 = 0$. This holds true in a TNTI as the free-stream is irrotational. The lack of rotational fluid in the free-stream is also the condition that forces the inertial term to be insignificant in the viscous superlayer, thereby defining the important role of viscosity in the outer regions of the TNTI. For a turbulent/turbulent interface, rotational flow is readily available on both sides of the boundary, therefore lifting the constraint that ensures inertial enstrophy production decays to zero. We therefore question, **what is the role of viscosity in a turbulent/turbulent interface?** Figures 4.2, 4.3 and 4.4 depict the interface conditioned behaviour of the inertial production and viscous diffusion terms for all of the runs conducted in the present experimental campaign. It is important to highlight the behaviour of run 1a. The turbulent/non-turbulent interface that this run captures, reproduces results that are remarkably similar to the TNTI results found in literature, notably from direct numerical simulation of the governing Navier-Stokes equations (eg. Silva *et al.*, 2018). The complete lack of any enstrophy production on the background/free-stream side of the wake boundary ($\gamma > 0$) is clearly evident with respect to both the inertial as well the viscous diffusion terms. With added background turbulence, the inertial term is no longer constrained to be zero at $\gamma = 0$ and is free to contribute to enstrophy production **throughout the entire thickness of the interface**. All runs exposed to background turbulence see an increase in enstrophy production across the whole of the interface. Runs in group 3 especially see significantly greater production through the inertial term, which should be expected considering the extreme conditions in the background turbulence that are present for these runs.

In order to ascertain the role of viscosity, the viscous diffusion term has been plotted for groups 1 and 2 and for group 3 in figures 4.3 and 4.4 respectively. With respect to the no-grid case, the behaviour observed in direct numerical simulation studies, including the characteristic peak in production near the outer edge of the interface (viscous superlayer), is reproduced e.g. (da Silva *et al.*, 2014). Viscous diffusion acts as a source of enstrophy near $\gamma = 0$ but it quickly reverts to a sink for small values of $\gamma < 0$ (within the wake). The viscous diffusion term acts in a similar

manner to the no-grid case for runs in groups 1 and 2 with minimal activity in the free-stream followed by source-behaviour at the outer edge of the interface. All cases with background turbulence exhibit increased noise which may be expected since fewer usable snapshots are captured (i.e. where the interface spans the entirety of the field of view). However, even with the increased noise the underlying behaviour can be established for groups 1 and 2. This is not the case for runs that lie in group 3 where all of the similarity to the no-grid case is lost. The level of noise is also greater as the characteristic production peak is no longer distinctly visible. Most importantly, the magnitude of the viscous diffusion term is insignificant when compared to the amount of enstrophy produced through vortex stretching for cases with free-stream turbulence.

Our results show that the role of viscosity is much reduced in a turbulent/turbulent interface, to the point of insignificance. We clearly showed the existence of an interfacial layer between the background turbulence and that within the wake, which manifests itself as a discontinuity/jump in enstrophy. However, viscosity is no longer the only mechanism through which enstrophy may be produced in the outer regions of the interface. The availability of turbulent vorticity/strain rate uncages the inertial term which thereby acts as the main producer of the enstrophy that yields this discontinuity, and allows it to participate in the turbulent/turbulent entrainment process. This has implications for the arguments pertaining to the scaling of the thickness of the TTI, since there is no longer a relevant physical argument to suggest that a TTI's thickness scales with the viscous Kolmogorov length scale. Further, it has connotations for numerical modelling of turbulent/turbulent entrainment since it is inertia and not viscous diffusion that is active within the TTI.

Previous work (Kankanwadi & Buxton (2020); Buxton *et al.* (2019); Cimarelli *et al.* (2015)) showed that the presence of a turbulent interface introduces a strong, small-scale anisotropy into the flow; enhancing strain-rates in the interface-normal direction somewhat analogously to a wall in wall-bounded turbulence. This is further verified in this chapter in figure 4.5. Here, interface conditioned anisotropy has been calculated two-dimensionally in the transverse $(y-z)$ plane considering only the v and w velocity components. Mathematically, we define the anisotropy in the context of a ratio of interface-normal velocity gradient to interface-parallel

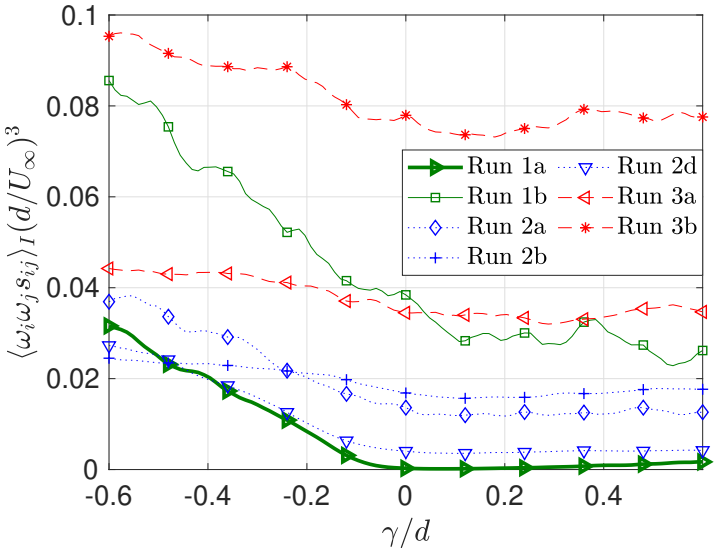

Figure 4.2: Intertial term of the enstrophy budget equation as a function of normal distance away from the interface.

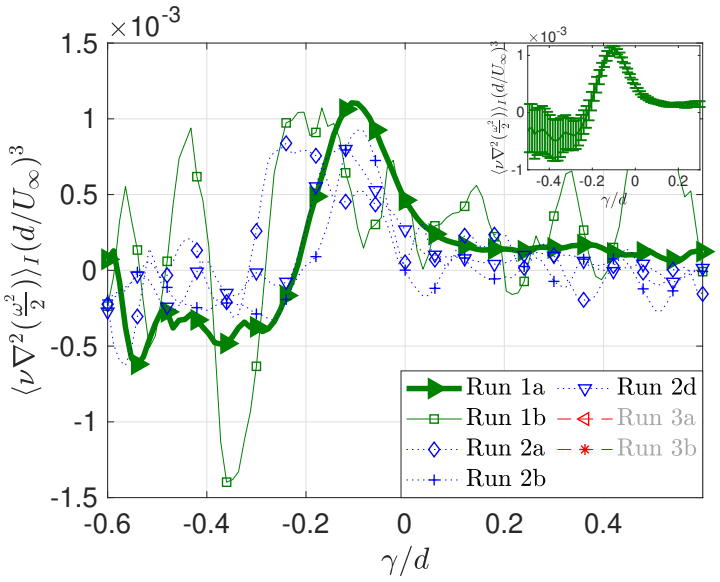

Figure 4.3: Interface conditioned plot of the viscous diffusion term of the enstrophy budget equation for cases in groups 1 and 2. Inset displays 95% confidence intervals for the no grid case.

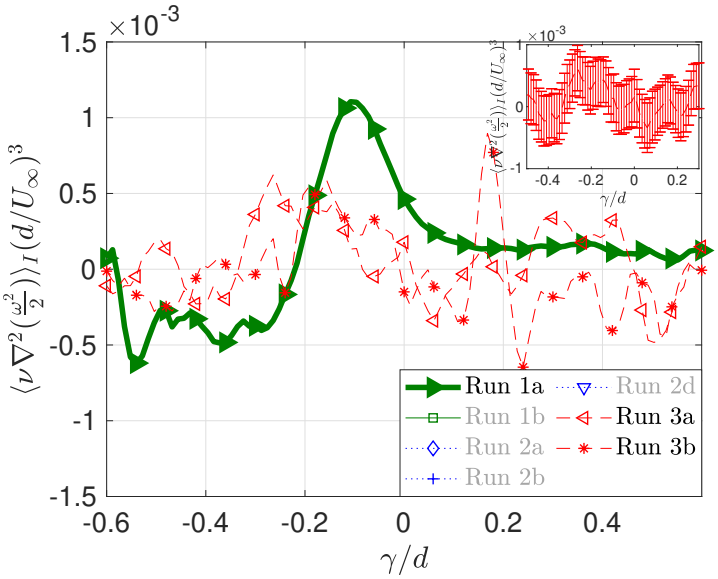

Figure 4.4: Interface conditioned plot of the viscous diffusion term of the enstrophy budget equation for cases in group 3. Inset displays 95% confidence intervals for run 3a.

velocity gradient magnitudes, $\langle\Sigma\rangle_I = \langle\left(\frac{du'_\gamma}{d\gamma}\right)^2\rangle / \langle\left(\frac{du'_\xi}{d\xi}\right)^2\rangle$. Here, γ and ξ represent interface-normal and interface-parallel coordinate directions, with u'_γ and u'_ξ representing fluctuating velocity components in this interface coordinate system. Far away from the interface $\langle\Sigma\rangle_I$ is close to unity (i.e. isotropy) but a peak in this anisotropy metric in the vicinity of the wake boundary denotes disproportionately larger velocity gradients (strain rates) in the interface-normal direction within the TTI. These enhanced strain rates offer a potential explanation for the enhanced enstrophy production, and hence enstrophy jump, in TTIs. However, inertial enstrophy production depends not only on the magnitude of the strain-rate tensor and vorticity vector but also the alignment between the two. If the vorticity is somehow more "organised" in the wake than the freestream, i.e. exploiting this enhanced interface-normal strain rate and more efficiently aligning itself with the extensive strain-rate that yields $\omega_i s_{ij} \omega_j > 0$, then enhanced enstrophy production will be found on the wake-side of the TTI. Such an argument also offers an explanation for the conditional mean enstrophy jump occurring even for group 3 cases, in which the intensity of the turbulence in the background is greater than in the wake.

We test this hypothesis by examining the relative contribution of the strain rate normal to the interface to the overall enstrophy production $\omega_i s_{ij} \omega_j$. We choose to do this by deconstructing the inertial term using the Betchov decomposition (Betchov, 1956), $\omega_i s_{ij} \omega_j = \omega^2 s_i (\hat{\mathbf{e}}_\mathbf{i} \cdot \hat{\omega})^2$, where

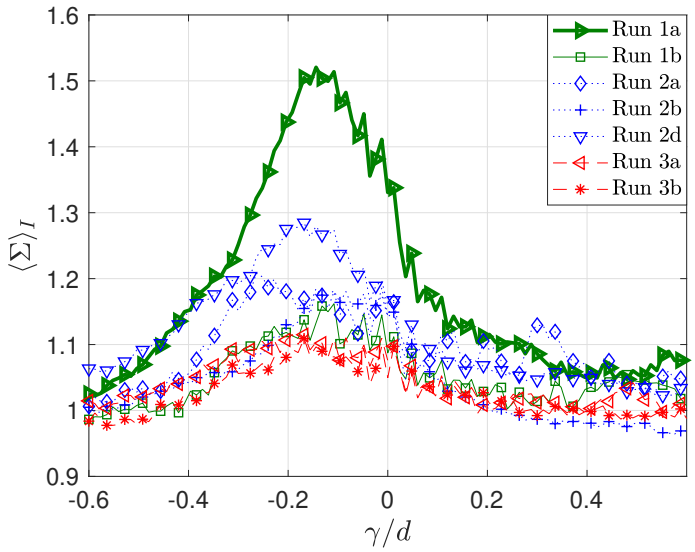

Figure 4.5: Interface conditioned plot of anisotropy in the vicinity of the interface.

s_{ij} and s_i are the strain-rate tensor and the eigenvalues of the strain-rate tensor respectively. This decomposition illustrates that it is not simply the magnitude of the strain-rate tensor (and vorticity), but also the alignment between the strain-rate eigenvectors and the vorticity vector that determines the level of inertial enstrophy production ($\hat{\mathbf{e}}_\mathbf{i}$ and $\hat{\omega}$ represent unit vectors pointing in the direction of the strain-rate eigenvectors and the vorticity vector respectively).

We now examine the contribution to $\omega_i s_{ij} \omega_j$ from the principal strain-rate that is most aligned with the interface normal vector that was extracted $\hat{\gamma}$. Prior to examining the results, it is important at this stage to address a couple of assumptions made during the analysis. The current analysis is independent of the particular orientation of the strain-rate eigenvectors, ie. no distinction is made between vectors pointing in a particular direction or a direction rotated by π. Mathematically, the alignment angle is redefined as, $\theta_i = min(\theta_i, \pi - \theta_i)$. Furthermore, it is important to note that the interface is assumed to be two-dimensional in the cross-stream plane (i.e. the streamwise component of $\hat{\gamma}$ is constrained to be equal to zero). This assumption is necessary since not every snapshot is considered to be valid, as the interface may leave the field of view. Returning to the analysis, in isotropic turbulence the contribution of the inertial terms corresponding to the three principal strain directions that have been decomposed through the Betchov decomposition should be all of equal magnitude. However, this does not hold true in the vicinity of the interface due to the small-scale anisotropy created by the presence of the

interface. Figure 4.6 plots the fraction of enstrophy produced through the term most aligned with the interface-normal direction ($\max\{|\hat{\mathbf{e}}_\mathbf{i} \cdot \hat{\gamma}|\}$), with respect to the total inertial enstrophy production. Mathematically, this is represented as, $\omega^2 s_{aligned}(\hat{\mathbf{e}}_{aligned} \cdot \hat{\omega})^2/\omega_i s_{ij} \omega_j$. Similarly to the previous plots, this figure shows this behaviour as a function of distance normal to the interface γ. It should be noted that only the values inside the wake have been plotted for the no-grid case, since the inertial term is negligible in the free-stream for this case. It is clear to see from the figure that on the wake side of the interface the aligned contribution is significantly larger than the expected 1/3 ratio thereby supporting the initial hypothesis that vorticity inside the wake is more "organised" allowing for increased enstrophy production.

Elsinga & da Silva (2019) examine the turbulent/non-turbulent interface in a data-set obtained using direct numerical simulation (DNS) of a planar jet. They show that at the irrortational boundary, there is preferential alignment of the most compressive strain-rate eignevector and the interface normal direction. Whilst, at first sight this seems a contradiction to increased aligned contribution to interial enstrophy production that is observed here, it may be possible to explain this result. Elsinga & da Silva (2019) observe the preferential alignment of the most compressive strain-rate eignevector and the interface normal direction at the irrotational boundary itself ($\gamma = 0$). This preferential alignment of the most compressive eigenvector is seen to decrease at positions further into the wake side of the interface, as the alignment of the most stretching term is seen to increase. In our study, the observed peak of aligned contribution occurs in a region that is offset into the wake side of the boundary ($\gamma \lesssim 0$). The peak in the aligned contribution observed in figure 4.6 occurs approximately between $0.2d$ to $0.3d$ into the wake side of the interface. This translates to $-0.7\lambda_{no\,grid}$ and $-1.1\lambda_{no\,grid}$ respectively, where $\lambda_{no\,grid}$ is the Taylor length scale calculated for the no-grid case. Note that the Taylor scale is calculated using the following relation, $\lambda_{no\,grid} = \sqrt{10\nu k/\varepsilon}$, where k is the turbulent kinetic energy and ε is the dissipation rate. Elsinga & da Silva (2019) explain that vortex stretching maintains a large magnitude in this region, which lies in the turbulent sub-layer. Furthermore, da Silva & dos Reis (2011), who examine coherent structures at the TNTI, explain that large scale vortical structures that scale with the Taylor microscale exist in the interfacial region and are in-turn responsible for the producing the vorticity jump. Therefore,

it is likely that aligned peak witnessed in this study is a by-product of the large scale vortical structures highlighted by da Silva & dos Reis (2011). An alternative explanation may be to do with the role of viscosity. Results in this chapter have shown the the role of viscosity is not significant in a turbulent/turbulent interface. In a turbulent/non-turbulent interface, it may be possible that viscosity acts as a damper for the turbulent strain at the irrotational boundary, which may favour compressive strain rate rather than extensive strain rate. With the subdued role of viscosity in the turbulent/turbulent interface, this mechanism will not apply. In the turbulent/non-turbulent case, the sharp rise in the aligned contribution occurs approximately 1λ into the wake side of the interface. This metric however continues to rise, although it is thought to be a result of the insignificant magnitude of the inertial term near the irrotational boundary, producing large ratios.

Lastly, the underlying actors responsible for the increased aligned contribution to enstrophy production are visually depicted in figure 4.7. Plotted is the joint probability density function of the cosine of the most aligned angle between principal strain rate and the interface-normal direction, $\cos(\theta_{min}) = \max\{|\hat{\mathbf{e}}_\mathbf{i} \cdot \hat{\gamma}|\}$ as well as the corresponding eigenvalue ($s_{\theta_{min}}$). A positive value of $s_{\theta_{min}}$ corresponds to vortex stretching (extension), whereas, $s_{\theta_{min}} < 0$, reflects compression. In the interest of brevity only a single joint PDF of run 2d has been shown. However, this is a typical example of what can be observed for runs subjected to free-stream turbulence. In the wake side of the interface a clear bias can be seen toward extension across the range of alignment angles, thereby boosting enstrophy production in this region ($\omega_i s_{ij} \omega_j > 0$). Such skewed behaviour is no longer present on the free-stream side of the interface. Whilst a slight bias towards extension still exists as is expected for homogeneous turbulence (Taylor, 1938), it is not comparable to what is seen on the wake side of the interface. We thus conclude that introduction of the small-sale anisotropy in the TTI coupled to the preferential alignment of the vorticity vector with the interface-normal direction is responsible for producing the enstrophy jump observed in a TTI.

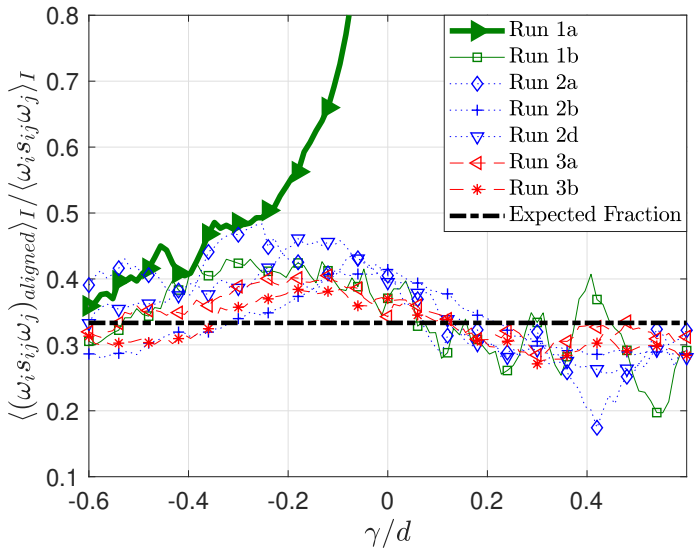

Figure 4.6: Interface conditioned plot of the interface-normal aligned contribution of the overall inertial production term. Note that the black dot-dashed line represents the expected fraction in isotropic turbulence.

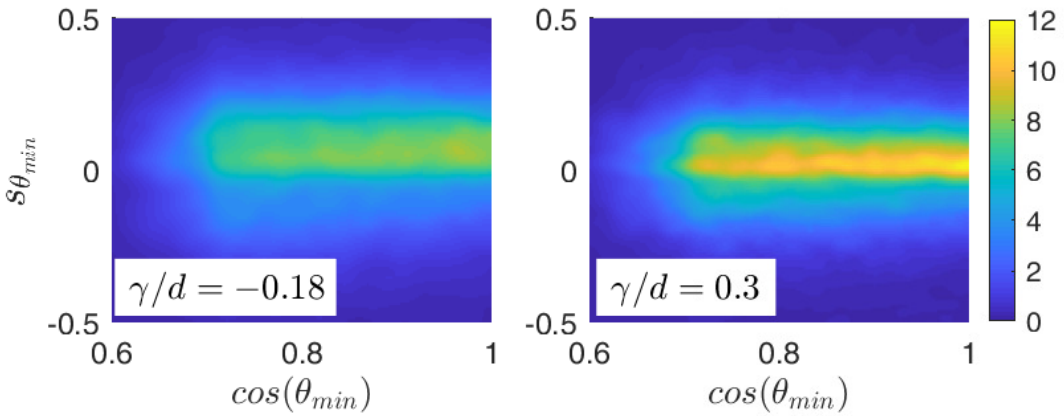

Figure 4.7: Joint PDF of the most aligned strain-rate eigenvalue and cosine of the alignment angle between said strain rate and the interface-normal direction for run 2d.

4.3 Conclusions

The turbulent/turbulent interface was examined in detail through interface-conditioned statistics of the enstrophy budget terms. The role of viscosity is known to be of critical importance in the TNTI, as it is the sole mechanism by which enstrophy is imparted to the background fluid across a TNTI. However, with rotational fluid available in the free-stream side of a turbulent/turbulent interface, the inertial term is free to contribute to enstrophy production throughout the entire thickness of the interface. Results showed that the magnitude of enstrophy production through the inertial term dwarfed that of the viscous term throughout the entire interface and therefore it is possible to conclude that in a turbulent/turbulent interface the role of viscosity is reduced to insignificance as the inertial term takes over responsibilities for the enstrophy production. Further, similarly to a wall in wall-bounded turbulence the turbulent/turbulent interface acts to enhance strain-rates in the interface-normal direction close to the boundary. Finally, decomposing the inertial term into three terms corresponding to the three principal strain directions highlighted that the component most aligned to the interface-normal direction contributes to a large share of inertial enstrophy production on the wake side of the interface. This is indicative of better "organised" vorticity on the wake side, thereby taking advantage of the strong interface-normal strain rates to produce the enstrophy jump observed in a turbulent/turbulent interface. These results have important implications with regards to modelling entrainment behaviour in a turbulent environment as the role of inertia is instrumental in the entrainment process, something typically neglected when only considering entrainment from a non-turbulent background.

The results presented in this chapter lead to open questions regarding the phenomenology of a turbulent/turbulent interface. The structure of a TNTI is well known, as there are distinct layers in which, respectively, viscous and inertial processes dominate the flow physics. For example, it is possible to claim that the viscous super-layer is bounded between the irrotational boundary and the location where the inertial term produces a larger share of enstrophy than the viscous term (Taveira & da Silva, 2014). However, these bounds lack any physical relevance when applied to the turbulent/turbulent interface. The internal structure of the tur-

bulent/turbulent interface must therefore be further investigated. It is interesting to note that the even with turbulence available in the background, the viscous diffusion term for groups 1 and 2 produces a production peak similar to the no-grid case. Hence, it is possible to raise the question, if this is a remnant of a defunct viscous super-layer? Additionally, with a diminished role of viscosity, there is also no longer a relevant physical argument supporting the scaling of the thickness of the turbulent/turbulent interface with the Kolmogorov length scale. The scaling of the turbulent/turbulent interface is therefore also an open question.

Lastly, it should be noted that by considering the far wake (i.e. a fully-developed turbulent shear flow) in chapters 3 and 4, it is assumed that the generality of the study is increased, with the analysis being more applicable to other flows, such as jets and even boundary layers (Silva *et al.*, 2018; Watanabe *et al.*, 2018). Whilst it is not possible to claim any universality, since that would require experiments conducted over a large range of Reynolds numbers using several flow types, the results are robust within the extensive parametric envelope that was investigated. Free-stream turbulence conditions that were considered had length scales both larger and smaller than the wake-generating object as well as intensities smaller and larger than within the wake.

Chapter 5

Near wake

5.1 Introduction

This chapter focuses on the near-field of a cylinder wake, where the flow field is investigated up to a streamwise distance of approximately 6 diameters downstream of the rear face of the circular cylinder. Experimental campaigns conducted for this study were done with a circular cylinder of diameter equalling 30 mm. The Reynolds number with respect to the cylinder diameter is $Re_d \approx 12000$. This places the cylinder in the shear layer transition regime (Williamson, 1996). An updated experimental envelope, re-normalised with the appropriate cylinder diameter and turbulence intensity averaged over the field of view used for this campaign, is provided in figure 5.1. Additional groups have been introduced in this figure, which will be explored later in the chapter. It should be noted that continuity of the naming convention persists with regards to the previous chapters. Equivalent run names continue to depict the same background turbulence conditions as they did in the previous chapters. Length scales depicted in figure 5.1 differ simply as a result of being normalised by a larger cylinder diameter.

The initial part of the chapter lays out the methodology used during this study. The results are split into two main parts. The first, addresses wake growth in the near field under the influence of background turbulence. Whereas the latter, focuses on intermittent events that significantly impact near-wake behaviour.

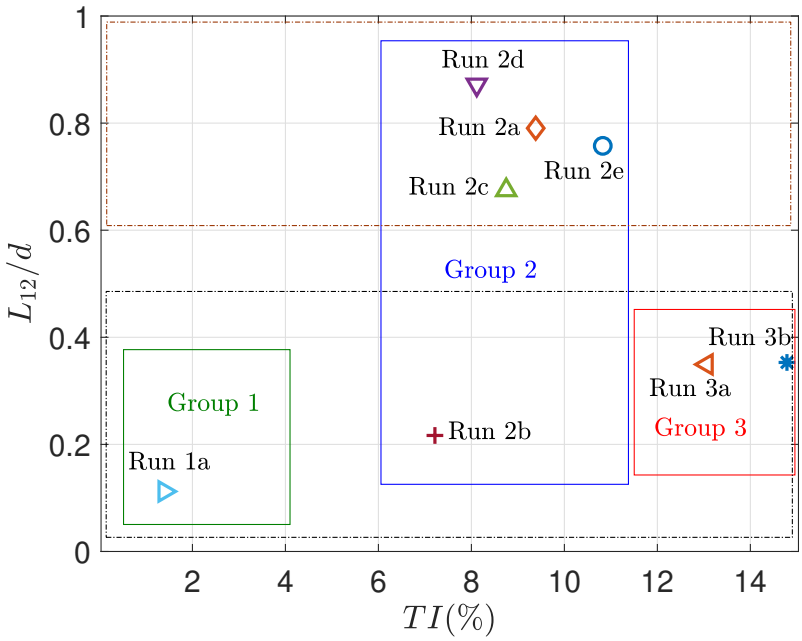

Figure 5.1: Experimental envelope for the near-wake study. The length scales in this plot have been normalised with the cylinder diameter used in the near-wake study. Additionally, two new groupings have been proposed (dot-dashed boxes). These classify 'large' and 'small' length scale runs.

5.1.1 Wake identification methodology

The methodology used to identify fluidic regions that belonged to the wake in the near-field is based on a similar light intensity gradient based scheme used previously in this chapter. However, instead of relying on one continuous contour, two of the longest contours in the field of view are identified and used as the boundaries of the wake region. The region that lies in between the two contours are classified to be inside the wake (later referred to as 'in-wake'). Figure 5.2 depicts this process pictorially. This process was repeated for all snapshots in the run and thereby, a complete map of the development of the wake in the near-field was obtained.

Alternative wake identification methodologies such as the Canny edge detection scheme (Canny, 1986) were also implemented. However, the light intensity gradient scheme laid out in chapter §3 was used due to its ability to use an aggressive threshold to combat secondary fluorescence. In the near-field, especially in the vicinity of the rear face of the cylinder, the halo effect due to secondary fluorescence is highly prevalent either side of highly concentrated regions of the dye. With the Canny scheme being somewhat of a black box, rejecting edges from fluid regions

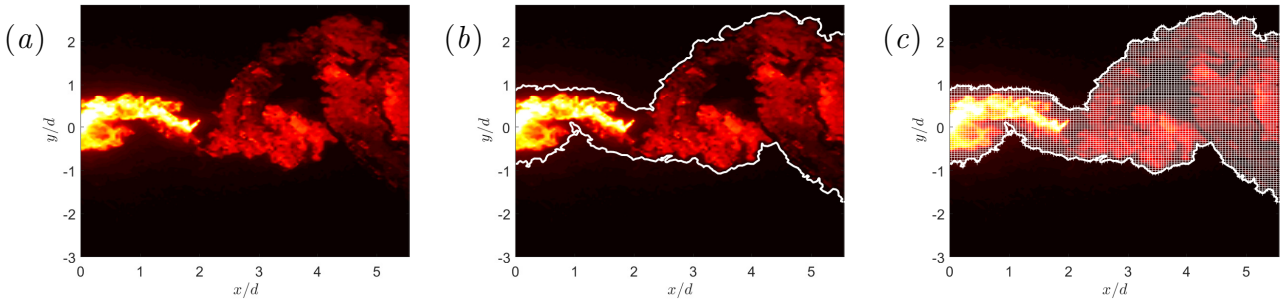

Figure 5.2: (*a*) A typical PLIF image. (*b*) The solid white lines represent the wake boundary as identified by the gradient metric. (*c*) All points within the identified contours are considered to be 'in-wake'.

lit due to the halo effect was problematic. Therefore, the gradient based method was used in the near-field as well. It should be noted that for all of the flow configurations presented in this chapter, a separated threshold study was conducted for each of then and a gradient was appropriately chosen. The methodology of the threshold study is the same as that described in §3.2.2.

It is interesting to note that a large pocket of fluid that does not have a significant scalar presence is considered to be part of the wake in figure 5.2. This follows from the adopted methodology to consider all regions of fluid within the identified contours to be 'in-wake'. This pocket represents a region of engulfed background fluid and is a typical example of the engulfment process, which is of great importance in the near field (Dahm & Dimotakis, 1987, 1990; Burridge *et al.*, 2017). In most far-field analysis, it is possible to ignore entrainment that happens through engulfment, since the proportion of growth through engulfment may be considered negligible. Mistry *et al.* (2016) show that in their analysis of a jet, at a streamwise distance of 50 diameters, engulfed fluid only amounts to 0.44% of the jet area. Similar liberties may not be taken in the near-field since engulfment potentially has a more pronounced role in the entrainment process.

5.1.2 Triple decomposition

The flow field being examined is dominated by coherent structures that are periodically shed by the cylinder. It is therefore useful to decompose the velocity field into a periodic and stochastic

component. This follows the triple decomposition method outlined by Reynolds & Hussain (1972). A part of the derivation has been recreated below for reference. The method is based on decomposing the fluctuating velocity component $s'(\mathbf{x}, \mathbf{t})$, into, a coherent fluctuation, $\tilde{s}$, and a stochastic fluctuation s''. The total variable, s is described by the sum in equation (5.1). Note that equation (5.2) represents the numerical implementation of the same. k is the chosen phase(ϕ) sub-population, whereas p depicts the selected time snapshot.

$$s = \bar{s} + \tilde{s} + s'' \qquad (5.1) \qquad\qquad s_{\phi=k,\ n=p} = \bar{s} + \tilde{s}_{\phi=k} + s''_{n=p} \qquad (5.2)$$

For a population of size N, with samples, s_n, an average over the population can be defined in two ways. Both of which are described by eqs. (5.3) and (5.4). Note that $\langle s \rangle$ represents the phase average and is evaluated as a mean over a sub-population of samples that correspond to the same phase angle.

$$N\bar{s} = \sum_{n=1}^{N} s_n \qquad (5.3)$$

$$N_i\langle s \rangle = \sum_{\nu=1}^{N_i} s_\nu \quad (i = 1, 2, ..., \text{ Number of phase sub-populations}) \qquad (5.4)$$

The periodic component, $\tilde{s}$ can then be calculated as,

$$\tilde{s} = \langle s \rangle - \bar{s} \qquad (5.5)$$

Complexity arises in assigning a phase value for each time snapshot of the signal. Investigators in the past have tackled this using a collection of methods, of which, the most widely used, are described below. Hussain & Reynolds (1970) knew a priori the instantaneous phase value of their signal, hence allowing them to sample at specific phase values. This method has been coined as conditional point averaging. Due to the requirement of having prior knowledge of the phase signal, this method has very specific use cases. Cantwell & Coles (1983) proposed a

more general method of phase averaging, often referred to as bin averaging. They made use of a pressure sensor mounted on the front face of their circular cylinder in order to record vortex shedding phase. It is then trivial to bin each sample into a collection of phase sub-populations. However, due to the lack of a pressure sensor in our experiment to provide a phase reference, a phase averaging method without this requirement is needed. Perrin *et al.* (2006) utilised proper orthogonal decomposition in order to separate the coherent part of the flow behind a circular cylinder, $\tilde{s}$. They show that the first two modes contain 60% of the total fluctuating energy at that particular Reynolds number and the first 10 modes are sufficient to obtain the features of the large scales. For the purposes of this study, a method developed by Baj *et al.* (2015) will be utilised. They make use of optimal mode decomposition (OMD), a technique developed by Wynn *et al.* (2013), to evaluate modes that are associated to vortex shedding. The following paragraph aims to provide an overview of the method. For a more thorough description, the reader is advised to refer to references Wynn *et al.* (2013); Baj *et al.* (2015).

Optimal mode decomposition: OMD is a snapshot based technique that exploits a linear dependency between successive snapshots. A time-invariant matrix $\mathbf{D}$, of size, $\mathbf{D} \in \mathbb{R}^{m \times m}$, determines the system dynamics that transform $\mathbf{q}^n$ to $\mathbf{q}^{n+1}$, where $\mathbf{q}$ is a collection of 2D PIV snapshots reshaped into a 1D vector ($\mathbf{q} \in \mathbb{R}^{m \times 1}$). Note that m depicts the snapshot size. The system is said to be represented appropriately when equation (5.7) is minimised.

$$\mathbf{q}^{n+1} \simeq \mathbf{D} \cdot \mathbf{q}^n \tag{5.6}$$

$$\min_{\mathbf{D}} ||[\mathbf{q}_2, \ldots, \mathbf{q}_N] - \mathbf{D} \cdot [\mathbf{q}_1, \ldots, \mathbf{q}_{N-1}]||^2 \tag{5.7}$$

However, the difficulty of finding a solution to equation (5.7) arises due to the number of unknowns present in the problem, m^2. OMD aims to alleviate this problem by approximating $\mathbf{D}$ using a lower order matrix of arbitrary rank, r, represented by $\mathbf{L} \cdot \mathbf{M} \cdot \mathbf{L}^T$. The problem statement is then described by equation (5.8). The matrix $\mathbf{L}$ acts as a low dimensional subspace of the flow field, whereas $\mathbf{M}$ contains the dynamics of the system.

$$\min_{\mathbf{L},\mathbf{M}} ||[\mathbf{q}_2,\ldots,\mathbf{q}_N] - \mathbf{L}\cdot\mathbf{M}\cdot\mathbf{L}^T\cdot[\mathbf{q}_1,\ldots,\mathbf{q}_{N-1}]||^2, \quad \mathbf{L}\in\mathbb{R}^{m\times r},\ \mathbf{M}\in\mathbb{R}^{r\times r},\ \mathbf{L}\cdot\mathbf{L}^T=\mathbf{I}. \tag{5.8}$$

Upon the optimisation of the independent variables, $\mathbf{L}$ and $\mathbf{M}$, the OMD eigenvalues, λ_n^{OMD}, and modes, $\Phi_n^{OMD}(\mathbf{x})$ can be evaluated as per eqs. (5.9) and (5.10).

$$\lambda_n^{OMD} = \frac{\ln\lambda_n(\mathbf{M})}{\Delta t} \tag{5.9}$$

where, $\Delta t = \frac{1}{Fs}$, ie. the time difference between consecutive velocity fields. The OMD modes can then be calculated as follows. Note that, $\mathbf{z}_n$, is the eigenvector corresponding to $\lambda_n(\mathbf{M})$.

$$\Phi_n^{OMD}(\mathbf{x}) = \mathbf{L}\mathbf{z}_n \tag{5.10}$$

The flow field, $s'(\mathbf{x},t)$ can then be reconstructed using the following relationship.

$$s'(\mathbf{x},t) \simeq \sum_{n=1}^{r} c_n \Phi_n^{OMD}(\mathbf{x}) e^{\lambda_n^{OMD} t} \tag{5.11}$$

Coefficients, c_n, are required as the OMD modes are normalised to follow, $||\Phi_n^{OMD}||^2 = 1$.

The triple decomposition method outlined by Baj *et al.* (2015), and also the one used in this study, uses the optimal mode decomposition technique to evaluate OMD modes that represent the shedding of the cylinder. Shedding mode identification is done by considering the damping of the OMD modes; the least damped mode corresponds to the shedding mode of the cylinder at the frequency of interest. Since the modes are complex, an instantaneous phase value, $\phi_n(\mathbf{t})$, can be calculated for a particular mode. The angle of the complex coefficients corresponding to the shedding mode of the cylinder, $\angle c_{shedding}$, acts as the instantaneous phase signal for the triple decomposition of the velocity field.

Upon establishing the instantaneous phase signal for vortex shedding, collected samples were binned into a total of 20 sub-populations. Each phase bin had a size, $\Delta\phi = \pi/10$. In a

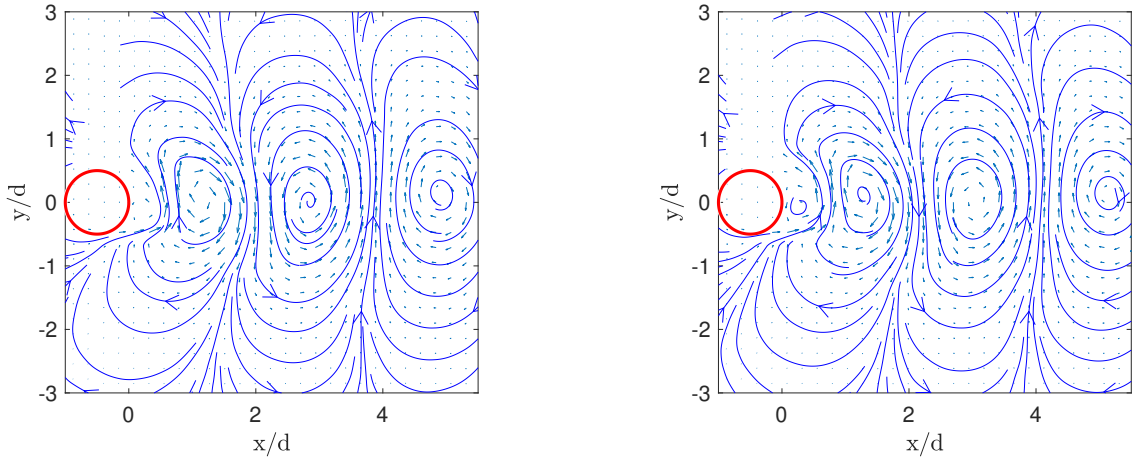

$(a)\ \phi = 0.45\pi$ $(b)\ \phi = 0.55\pi$

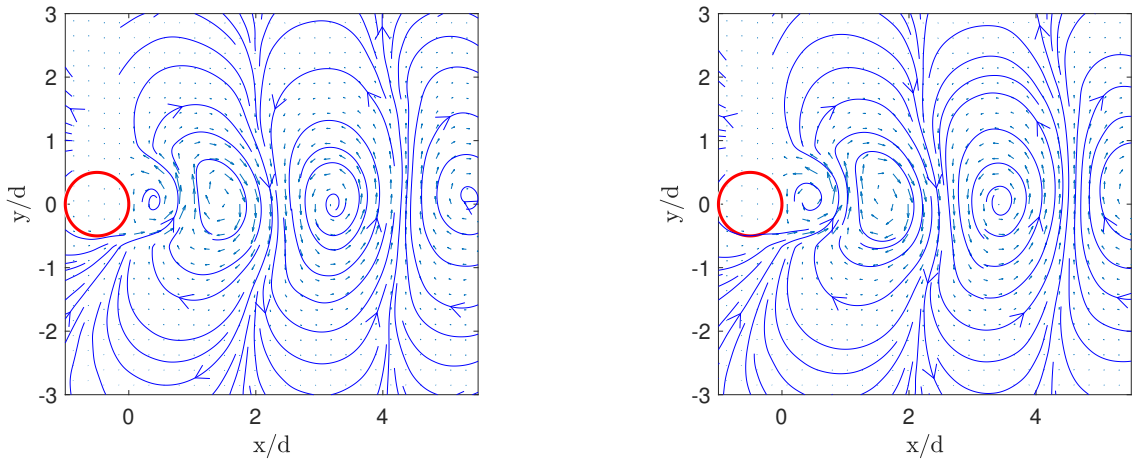

$(c)\ \phi = 0.65\pi$ $(d)\ \phi = 0.75\pi$

Figure 5.3: Plots of phase averaged velocity across four consecutive phase bins produced from a data set of the No-grid case. Superimposed on top of quiver plots of $\tilde{u}\,\&\,\tilde{v}$ are plots that depict streamlines.

typical run that had a total of 2537 snapshots, each phase bin consisted of approximately 127 snapshots. Figure, 5.3 provides typical examples of the periodic component of velocity over a few consecutive phase bins for the no-grid case. These plots depict both the formation of a vortex in the immediate vicinity of the cylinder and also the advection of shed vortices downstream of the cylinder. Comparing these results with literature (Cantwell & Coles, 1983) confirm a successful implementation of the methodology.

5.2 Wake growth

The near-field development of a cylinder wake in the presence of background turbulence has been briefly examined in literature. Bearman & Morel (1983) examined the effects of free-stream turbulence on the mean flow over bluff bodies in the near-field. They summarised the main effects to be accelerated transition to turbulence, and enhanced mixing and entrainment. Furthermore, they highlighted the importance of coherent structures on initial shear layer development and speculated on the effect that free-stream turbulence will have on them. Lastly, they outlined the fact that the mechanisms by which free-stream turbulence affects spreading rate were not yet well understood.

Eames *et al.* (2011) addressed the problem more recently. They developed a theoretical model of wake spreading downstream of a cylinder in ambient turbulence. They report that wake spreading gets affected by free-stream turbulence when the velocity deficit has decayed sufficiently that it becomes comparable to the background turbulence intensity. Their model predicts that when the wake width is smaller than the integral length scale, the wake grows linearly with streamwise distance ($\sim x$). Whereas when the wake width is larger than the integral length scale, the wake is predicted to grow diffusively ($\sim x^{1/2}$). The authors also conducted a laboratory run of flow past a cylinder in intense ambient turbulence (18%) that consisted of a large integral length scale (9.5d). They reported a velocity deficit result to show good agreement with their model. However, the model was only developed for instances where either very weak or very strong turbulence intensity was subjected to the cylinder. It does not aim to predict instances where both, internal and external regions of turbulence are significant to the spreading process. The authors conclude by stating that further research is required to understand the spreading of a plane wake under the effect of various levels of free-stream turbulence.

Near wake growth is of critical importance in wind turbine applications where deciding on wind farm layouts is critical. Empirical models are used to model the growth of a wind turbine wake. An example of such an empirical model is reported by Niayifar & Porté-Agel (2016). They adapt the model laid out by Bastankhah & Porté-Agel (2014), to incorporate the effects of turbulence intensity. The proposed empirical model obtained from large-eddy simulations,

consists of a linear fit that increases the growth rate of the wake with applied turbulence intensity. Whilst, the geometry of the wind turbine is significantly different to the cylinder considered in this study, the fidelity of models used to model wake growth under free-stream turbulence is important to consider.

It is clear to see that even in the near field of a cylinder wake, a conclusive understanding of the effects of free-stream turbulence is still lacking. This chapter aims to address these concerns with a parametric study exploring the near-field development of a cylinder wake.

The development of the wake in the near field can be separated into two distinct components. These can be identified as (a) the growth of the wake through entrainment and (b) the induced 'meandering' of the wake downstream of the cylinder. Simply relying on the mean coverage of the scalar to comment on wake growth is not reliable, since the growth of a wake in the near-field is an amalgamation of the true growth through entrainment and an illusion of increased wake width in a time-averaged sense due to meandering. Meandering is termed as the transverse oscillations of the shed vortical structures. Figure 5.4 provides an illustration of a meandering wake, where both growth mechanisms are realised. The following analysis aims to decouple the two phenomena to gain a clearer understanding of wake growth mechanisms when subjected to turbulent free-streams.

However, prior to this distinction being made, the wake growth is presented as a time average of the extent of the wake. This is important to include, since most literature refers to wake growth in this manner (example: empirical wind turbine wake growth (Jensen, 1983)). In order to evaluate this metric, the time average of the points that are considered to be in the wake is first calculated. A user defined threshold is then applied to the time-averaged field in order to establish the wake width. The chosen threshold represented a probability of 18% that a given point was considered to be within the wake over a time series. It was ensured that results were independent of the chosen threshold following a sensitivity study, described in appendix D.1. The chosen threshold probability of 18% is arbitrary. A methodology such as this is acceptable since the aim is to assess the trends of various runs with respect to each other. Figure 5.5 depicts the result of this process as it plots the wake width established using an "in-wake" threshold,

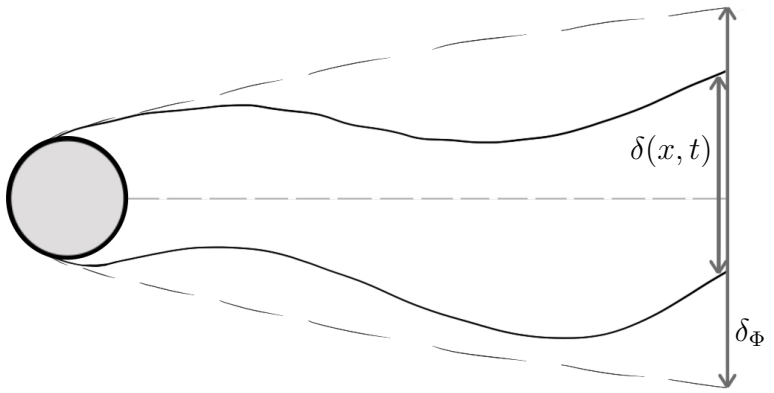

Figure 5.4: A meandering wake. Cartoon highlights both the instantaneous wake width, $\delta(x,t)$, and the time averaged scalar extent of the wake, $\delta_\Phi(x)$

δ_Φ, as a function of streamwise distance. The figure establishes that an increase in this metric is observed for cases with subjected free-stream turbulence. At $x = 5d$, group 3 cases display the largest wakes, followed by cases in group 2 and the baseline no-grid case presents a wake with the least width. This result is consistent with the traditional understanding of increased entrainment and mixing in the near-field due to background turbulence (Bearman & Morel, 1983), hence resulting in wider wakes.

Before progressing to the decoupled analysis, the lack of data between streamwise positions of $3 \lesssim x/d \lesssim 4$ must be addressed. Data in this region has been deliberately omitted from the analysis in this chapter to prevent an experimental artefact from unduly influencing the presented results. The artefact arises from the presence of bright reflections in the background of images taken by the PLIF camera. Analysis that relies on the PLIF experiment are therefore compromised and hence data collected in this region is omitted from any further analysis. Attempts to remove the background reflection using image processing, whilst promising, were largely unsuccessful.

Wake growth through entrainment is investigated by examining the temporal mean of the instantaneous wake width. This metric is depicted in figure 5.6 as a function of streamwise distance downstream of the cylinder. This result is intriguing since background turbulence is seen to both promote wake growth (group 3 cases) and also to diminish the same (group 2 cases). Close inspection reveals that there may be a link to the length scale of the subjected

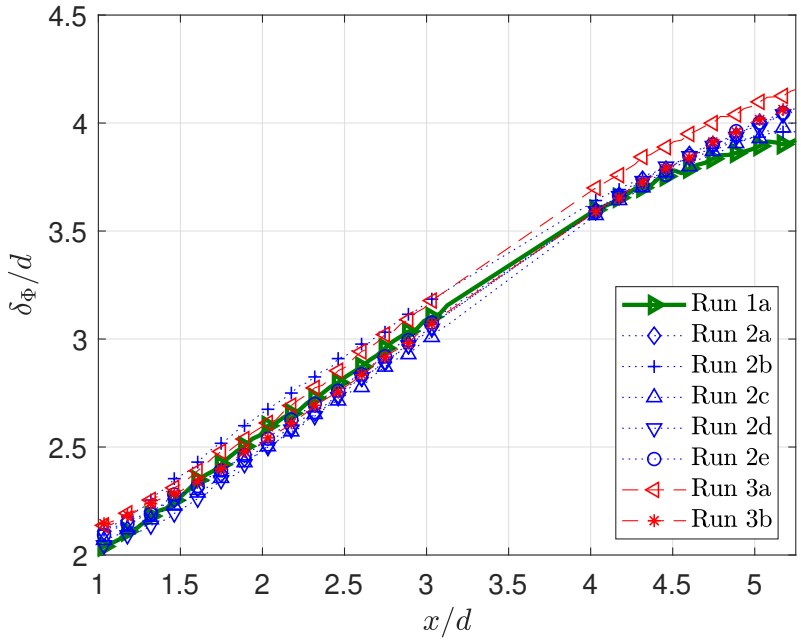

Figure 5.5: Time-averaged wake width obtained using a threshold on the total extent of the wake. Note that the region between $3 \lesssim x \lesssim 4$ has been omitted due to an experimental artefact (see discussion in the text).

background turbulence as all of the runs with stunted entrainment in the near-field have an increased background integral length scale. The slope of the instantaneous wake width may also be qualitatively compared since this provides an indication of the entrainment into the wake. Should wake growth be simplified to a linear model, $\delta = mx + c$, m may be considered to represent the entrainment rate whilst c accounts for the other near-wake effects. The gradient may be estimated by applying a linear regression for points that lie between $2.5 < x/d < 5$. For these x-positions, group 3 cases present the largest mean gradient, whereas the mean gradient for the no-grid case is equivalent to group 2.

Furthermore, background turbulence is also seen to have a defining effect on the 'meandering' observed in the near-wake. Figure 5.8 aims to quantify this effect by plotting the paths taken by vortex centres as they are advected downstream of the cylinder. To achieve this, vortices were tracked and analysed in a phase averaged sense. For each phase bin, vortex centres were identified and tracked by applying a threshold on enstrophy and velocity magnitude on the periodic component of fluctuating velocity, $\tilde{u}$ & $\tilde{v}$. Such an approach was possible since the phase averaging significantly reduced the level of noise. Thresholds ensured that regions of

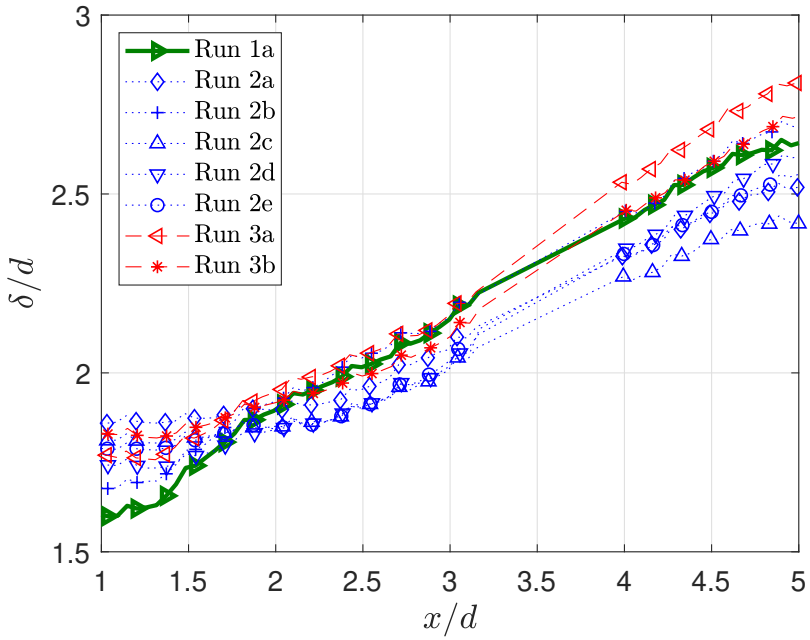

Figure 5.6: Temporally averaged instantaneous wake width as a function of streamwise distance downstream of the cylinder.

highest enstrophy combined with the lowest velocity magnitude were appropriately identified. A clustering scheme was then employed over the identified points, allowing for the centre of the vortex to be evaluated. Figure 5.7 illustrates the methodology. Depicted are a couple of typical phase averaged velocity fields in the form of red vectors for two different cases. It should be noted that not all vectors are plotted in the interest of clarity. The quiver plot is superimposed on top of a contour plot of the enstrophy field. Following the application of the vortex identification methodology described above, the identified vortex centres are highlighted in the figure. These results were also compared with the approach outlined by Vollmers (2001), which involved examining the λ_2 criterion for two-dimensional data. Vollmers (2001) explains that vortices appear for non-real eigenvalues of the velocity gradient tensor, $\mathcal{G}$. The discriminant, λ_2, separates vortices from other structures. Mathematically, this is defined as, $\lambda_2 = (\mathrm{trace}\,\mathcal{G})^2 - 4\det(\mathcal{G})$. Regions where this metric is negative represents vortical structures. Vortex centres can then be identified as the centroid of each region where $\lambda_2 < 0$. Results using both methods were found to be similar.

Identified vortex centres are depicted as individual data points in figure 5.8. It is clear to see that free-stream turbulence significantly increases the transverse location relative to the

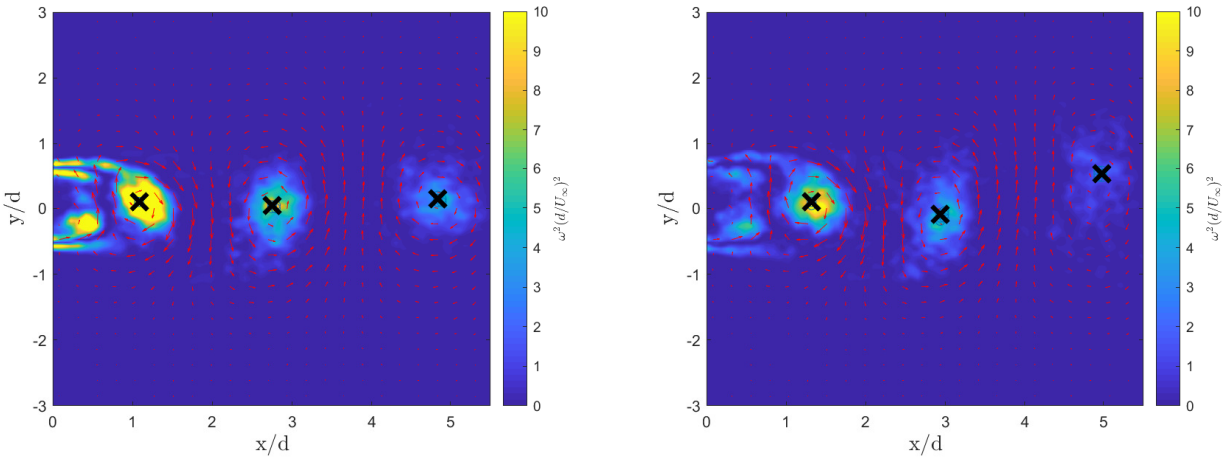

(*a*) Run 1a - No-grid case (*b*) Run 3a

Figure 5.7: Plots depict typical phase averaged velocity fields superimposed on top of the underlying enstrophy field. Identified vortex centres are highlighted with the black cross.

centreline of these coherent structures. This leads us to the conclusion that applied free-stream turbulence increases the level of meandering of the wake. It is also interesting to note that length scale of the background turbulence yet again plays a part; all of the cases that display heavily increased meandering originate from runs that have an increased integral length scale. Run 2d is an outlier as it displays only a slight increase in meandering despite the background turbulence housing a large integral length scale.

The two decoupled sets of analysis may be reconciled with the traditional wake width result. In order to do this it is helpful to re-categorise the runs with respect to length scale. Runs in group 3, group 1 and run 2b may be classed as runs that have a small background integral length scale. Whereas the remaining runs in group 2 as classified as runs with large background length scale (see figure 5.1). In general, it is found that cases with a small integral length scale see an increase in both instantaneous width and the level of meandering resulting in the largest temporally averaged wake widths (δ_ϕ). Cases with large background length scale on the other hand are seen to display a reduction in instantaneous wake width. However, this is compensated for by the significant increase in the level of meandering, thereby resulting in a small increase in time-averaged wake width compared to the no-grid case.

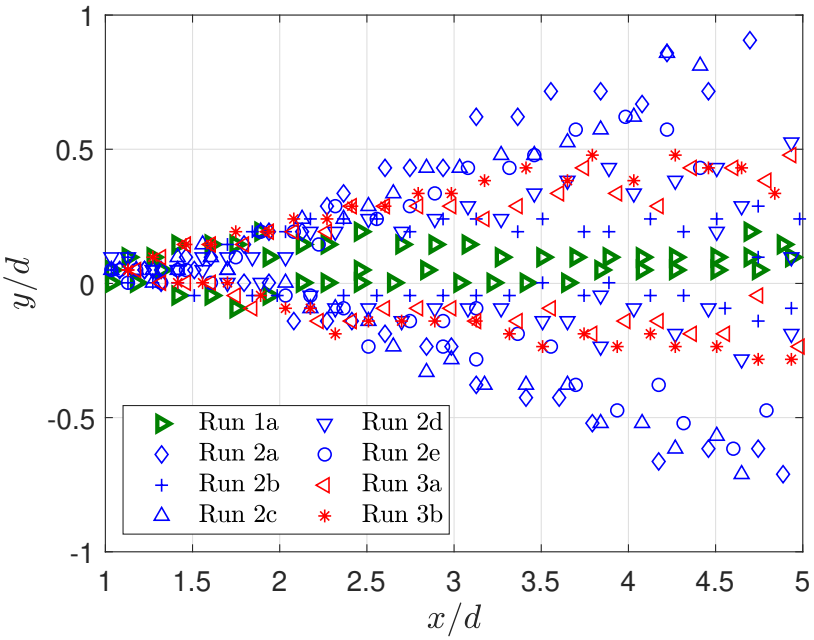

Figure 5.8: Vortex centres extracted from the phase-averaged velocity ($\tilde{u}\,\&\,\tilde{v}$).

5.2.1 Splitter plate

As the evolution of large-scale coherent structures are the main mechanism by which a wake develops in the near-field, a control experiment was designed with the aim of analysing the effect of free-stream turbulence on a flow field where these structures have been suppressed. Such an experiment will allow us to isolate the effects of meandering as well as establish the effects of large scale coherence on near-field entrainment. To this end, a splitter plate was designed and manufactured to prevent the two shear layers, shed from opposite sides of the cylinder, from immediately interacting. The suppression of coherence was achieved through the use of an 'infinitely long' splitter plate that was attached to the rear of the cylinder. The 'infinitely long' condition is said to be achieved when the reattachment point is on the splitter plate itself, since a further increase in length of the splitter plate has no effect on the flow pattern. This is illustrated through a flow schematic provided by figure 5.9. Apelt & West (1975) show that this condition occurs when $L/d > 5$ for a circular cylinder. Where, L, is the length of the splitter plate and d, is the diameter of the circular cylinder. They also mention that for an 'infinitely long' splitter plate, vortices that form over the plate are small and random, no coupling between the two sides of the splitter plate was witnessed, and that the shed wake was

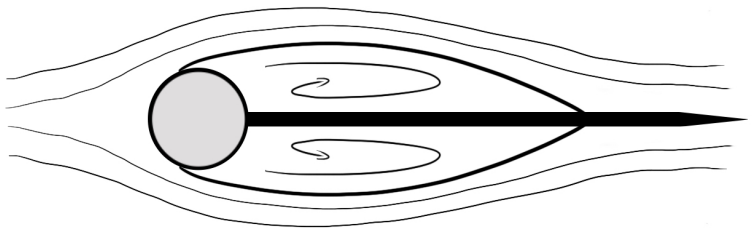

Figure 5.9: Schematic of a splitter plate satisfying the 'infinitely' long condition.

narrower and more steady. By installing such a splitter plate, regular vortex shedding from the cylinder was eliminated. However, Apelt & West (1975) noticed a well developed vortex street formed far downstream ($\sim 17d$) even with a long splitter plate such as this. They associated this behaviour to the cylinder/splitter plate combination giving rise to it's own unique vortex street.

Appendix A.1 provides details of the design of the splitter plate. Due to the need for the splitter plate to house a 2.39 mm hypodermic tube to transport fluorescent dye in an intial design, the thickness, t, of the splitter plate had to be increased to 5 mm. Investigators in the past have tended to stick to a thickness to diameter ratio, $t/d \lesssim 0.1$ (Apelt & West, 1975; Bearman, 1965; Roshko, 1961). Due to the increased thickness in our experiment $t/d \approx 0.17$, a streamlining section was added to the trailing edge of the splitter plate to prevent vortex shedding from the same. The diffuser angle for the streamlining section was designed to equal 3° to prevent any flow separation. The complete length of the splitter plate was therefore equal to, $L/d = 6.59$. However, the initial method of releasing dye into the wake from the trailing edge of the splitter plate was not successful. This was because the dye was not released in a recirculation zone and hence meant the that it was unable to fully mix and could not cover the full extent of the wake. In the second iteration of the experiment, the dye release point was altered and was instead released from the rear face of the cylinder. Two pumps connected to two separate holes, was the design choice. This allowed the dye to be released into both of the recirculation zones on either side of the splitter plate and hence allowed the dye to fully mix and cover the complete extent of the wake. The following section details the spectral signature of the flow field downstream of the splitter plate. The entrainment characteristics of the wake are then considered.

Coherence suppression

Prior to analysing results of the wake downstream of a splitter plate, it is imperative to investigate whether the coherence has been successfully suppressed. To this end, the spectral signature of the wake was extracted and analysed downstream of the trailing edge of the splitter plate. Figures 5.10(a) and 5.10(b) depict the frequency-time domain magnitude scalogram of the continuous wavelet transform of the transverse fluctuating velocity, v', for runs with and without the splitter plate installed respectively. Note that the transform was conducted using a Morse wavelet. The velocity is probed at the location defined by the white cross in figure 5.10(c). It is clear to see that no clear shedding band is visible in the magnitude scalogram across the whole time series in the wake of a splitter plate (see 5.10(a)). This result is in agreement with the results published by Roshko (1961), who comment on the fact that there is no peak in the spectrum when a splitter plate is installed. This is in complete contrast to the spectral signature when no splitter plate is installed. As expected, a strong shedding band is visible in figure 5.10(a) for the entire duration of the run. This is a clear indication that the splitter plate was successful in suppressing coherent structures in the near-field of the cylinder-splitter wake.

Furthermore, examining the phase signal of the least damped mode as identified by OMD analysis, similarly shows the lack of coherence in the flow field downstream of a splitter plate.

Wake development downstream of a splitter plate

Figure 5.11 outlines the temporal average of the instantaneous wake width downstream of the cylinder with an attached splitter plate. It should be noted that data for $x/d < 6.59$ is calculated differently to the methodology used downstream of this x-position. For data-points within $x/d < 6.59$, only one half of the wake is visible to the cameras, since the splitter plate casts a shadow over the far side of the wake and therefore the laser sheet is unable to illuminate the full wake. Due to this constraint, for the region $x/d < 6.59$, two times the temporal average of the instantaneous half wake width has been plotted in figure 5.11.

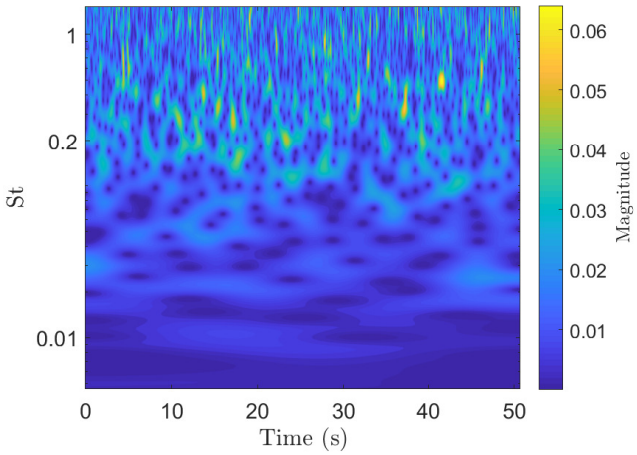

(*a*) With splitter plate

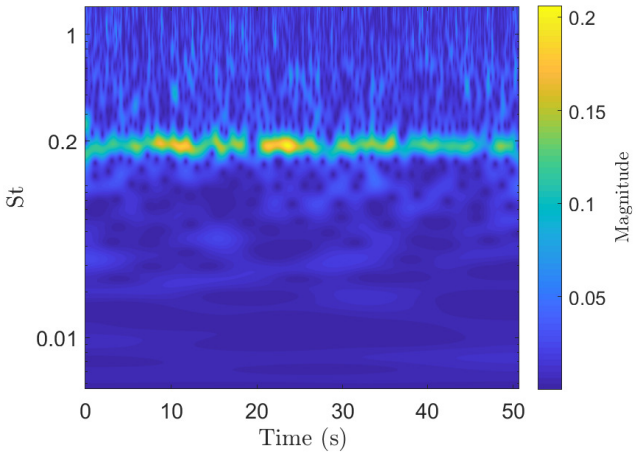

(*b*) Without splitter plate

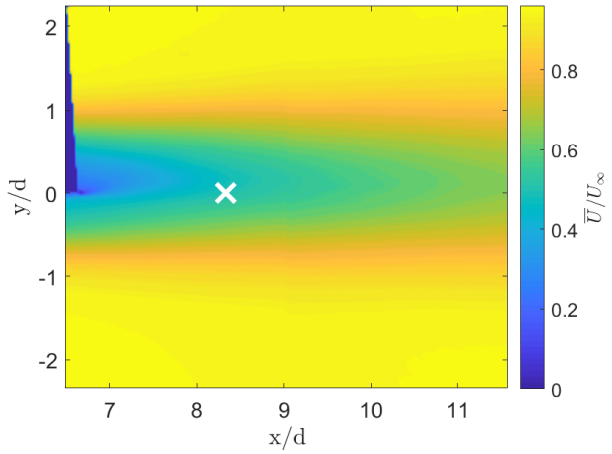

(*c*) Velocity probe location

Figure 5.10: (*a*) Magnitude scalogram of the wavelet transform of v' at the probe location taken during a run with the splitter plate installed. (*b*) Represents the same scalogram, although this time for a clean cylinder without a splitter plate. (*c*) The white cross defines the location of the probe where the spectral signature is analysed. The background field is the mean velocity in the streamwise direction for the run with the splitter plate installed.

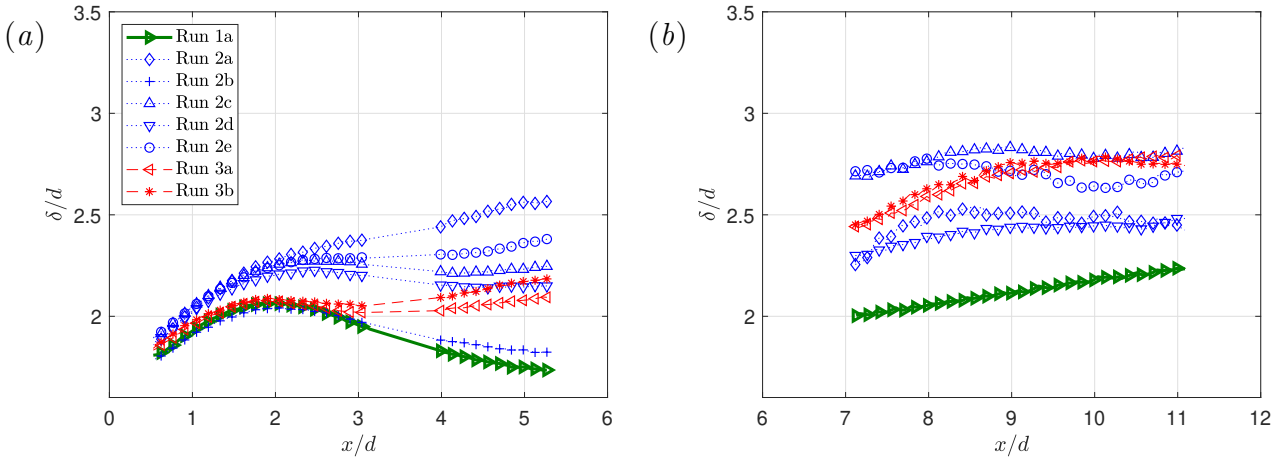

Figure 5.11: Temporal average of the instantaneous wake width downstream of the cylinder splitter plate combination. Plots (a) and (b) represent the upstream and downstream data set respectively.

It is evident from figure 5.11(a), that the mean coverage of the wake is greatly affected by the incoming background turbulence. Every case of subjected turbulence acts to increase the mean extent of the wake when the splitter plate is installed. The departure in behaviour of background turbulence cases with respect to the no grid case occurs in the region where the splitter plate is still present ($x/d < 6.59$). Whilst, the no-grid case observes a reduction in mean width in the region of the reattachment point and further downstream on the splitter plate, similar behaviour is not observed for cases with free-stream turbulence. The wake in these cases usually tends to continually increase in width as the x-position is increased, as seen in figure 5.11(a). The behaviour in the upstream set of data is dominated by reattachment of the flow.

Free-stream turbulence has a large influence on the reattachment point of the separated flow back onto the splitter plate. Bearman & Morel (1983) report on similar results for a rectangular cylinder with a splitter plate and show a decrease in reattachment length with increasing turbulence intensity. This behaviour is recreated here for a circular cylinder, with the group 3 cases showing a significant decrease in the reattachment length (see figure 5.12). In this context, the reattachment length is defined as the point where the metric calculated in a similar manner to the mean wall shear stress changes sign at the closest available y-position to the surface of the splitter plate. This is the best available indicator of the behaviour at the splitter plate surface.

The reduction in reattachment length is mainly driven by the intensity of the background turbulence rather than the length scale, which is in agreement with results reported in Bearman & Morel (1983). Only group 3 cases, which have a significant intensity in the background show a reduction in the reattachment length. Group 2 cases have a reattachment length that is largely similar to the no-grid case.

In the downstream set of data (figure 5.11(b)), the wake tends to develop quickly once both halves of the wake have merged downstream of the trailing edge of the splitter plate. This is also the region where the early influences of the far-field effect of entrainment are visible. Assessing the gradients of each plot, the wake in the no-grid case continues to grow at a steady rate downstream of the splitter plate. Cases that are exposed to background turbulence, generally see an initial jump in the wake width as the two sheared regions merge. However, entrainment effects of the free-stream turbulence quickly act, causing a sharp decline in measured gradients across all cases with background turbulence. This is especially evident upon applying a linear regression to points that lie between $9 < x/d < 11$. The no-grid case in this region continues to present a positive gradient, whereas cases in both groups 2 and 3 display a gradient close to zero.

It is clear to see that in the early developmental stages of the wake, free-stream turbulence has a very large impact and increases wake width. It is possible that this is associated with the increased importance of entrainment through engulfment in the near-wake of a circular cylinder, as evidenced by the splitter plate experiment. After switching off meandering with the use of the splitter plate, it was shown that background turbulence acts to increase entrainment in the region of the recirculation zone, until the sheared regions from both sides of the splitter plate interact. Following this downstream location the wakes tend to develop quickly and the far-field entrainment effects of background turbulence take over. The analysis in this section clearly highlights the spatial influence on entrainment effects of background turbulence, an avenue of research that requires further work.

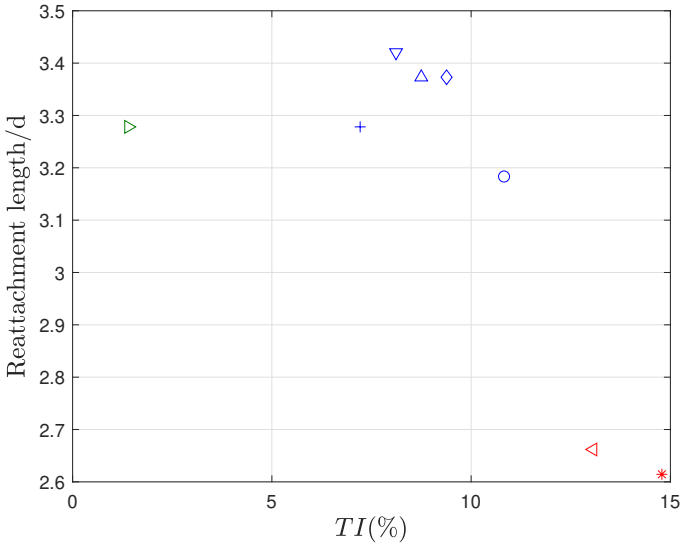

Figure 5.12: Reattachment length along the splitter plate, as a function of incoming turbulence intensity

5.3 Identity loss events

In the previous sections of this chapter, near-field effects of free-stream turbulence were assessed in a mean sense. The final section aims to analyse a dynamic phenomenon that has implications to instantaneous entrainment. During the course of analysing near-wake data, it was noticed that free-stream turbulence prompted several phases of severe disruption of the wake where the regular shedding pattern and entrainment rate in the near-wake were affected. During these intermittent events, there was a complete loss of structure in the wake and hence they are referred to as 'identity loss' events.

Figures, 5.13 and 5.14, respectively highlight the near wake during regular shedding in an undisturbed background and during an altered shedding event noticed under the influence of free-stream turbulence. These events where the shedding mechanism seemingly seems to be altered are identifiable as 'phase hiccups' in the phase signal of the shedding mode. Noting that the phase signal is obtained by evaluating the angle of the time dependent complex coefficients required to reconstruct the shedding mode in the optimal mode decomposition (OMD) technique (see §5.1.2). Figures 5.13(c) and 5.14(c) highlight the OMD phase signal during each event. The departure from periodic fluctuation of the phase is evident during an altered

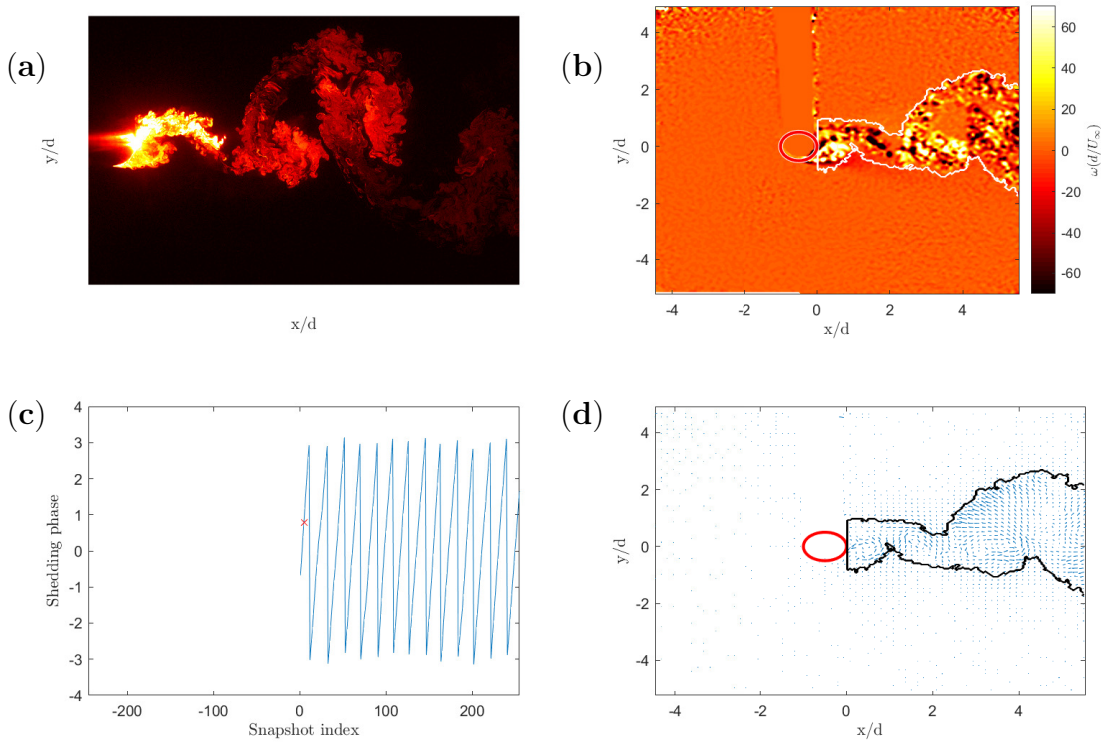

Figure 5.13: Regular shedding for a cylinder subjected to an undisturbed free-stream. The figures show details of a single investigated snapshot. (**a**) Raw PLIF image of the investigated snapshot. (**b**) Normalised vorticity, $\omega_z/(U_\infty/d)$, is plotted as the background (U_∞, is the free-stream velocity and d, is the cylinder diameter). Note the solid white contour line represents the scalar interface. (**c**) Phase signal for the reconstructed shedding mode, obtained using optimal mode decomposition (Wynn *et al.*, 2013). The red cross represents the snapshot being examined in this figure. (**d**) Instantaneous fluctuating velocity. Note the overlayed contour represents the scalar interface.

shedding event. Therefore, the OMD phase signal was used to identify occurrences of these events within all the runs conducted in this campaign.

Rather than periodically shed vortices as observed in a von Kármán vortex street, an incoherent shear layer is shed as the wake of the cylinder during an identity loss event. This in-turn gives rise to Kelvin-Helmholtz type vortices on both shear layers either side of the centreline. As can be observed in figure 5.14(d), the instabilities develop into a counter-rotating pair of vortices and cause significant back-flow near the wake centreline. Therefore, the implications with regard to instantaneous entrainment rate are significant and are likely to largely impact applications that rely on uniform mixing. Furthermore, it is highly likely that a sudden intermittent change to the

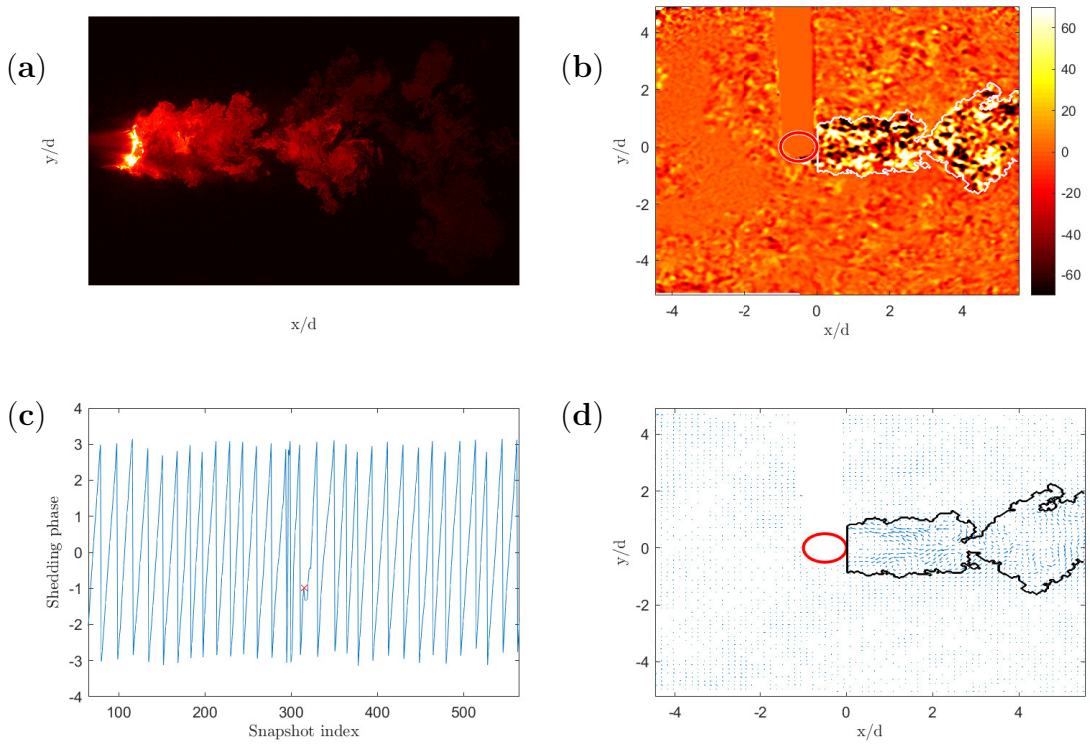

Figure 5.14: A snapshot of an Identity loss event, an example of altered shedding experienced by a cylinder in the presence of free-stream turbulence The figures show details of a single investigated snapshot. (**a**) Raw PLIF image of the investigated snapshot. (**b**) Normalised vorticity, $\omega_z/(U_\infty/d)$, is plotted as the background (U_∞, is the free-stream velocity and d, is the cylinder diameter). Note the solid white contour line represents the scalar interface. (**c**) Phase signal for the reconstructed shedding mode, obtained using optimal mode decomposition (Wynn *et al.*, 2013). The red cross represents the snapshot being examined in this figure. (**d**) Instantaneous fluctuating velocity. Note the overlayed contour represents the scalar interface.

shedding mechanism of the cylinder may have consequences with respect to the instantaneous load placed on the cylinder.

The plots in figure 5.15 depict the methodology employed to automate the identification of these events. Note that these plots are typical examples taken from Run 2e. Figure 5.15(a) is a plot of the typical phase signature of an altered shedding event. Reversal of the phase signal as well as a significant shift in instantaneous shedding frequency are characteristic indications of underlying identity loss events. Phase reversals were identified by scanning for a change in gradient over the time series after accounting for the discontinuities in phase at the end of each cycle. This technique was combined with spectral analysis that allowed for the identification for frequency change events. To this end the phase signal was analysed using a continuous wavelet transform. Figure 5.15(b) depicts the magnitude scalogram of the shedding phase transformed using a Morse wavelet. Clear departures in the magnitude at the shedding frequency are evident in the figure. The amplitude within the shedding band can be extracted and is plotted in figure 5.15(c). A user defined threshold may then be used classify snapshots where the in-band amplitude drops below the threshold as part of an identity loss event. In this case, an amplitude threshold of 0.7 was selected. Snapshots that passed either of the two tests, phase reversal or frequency shift, were deemed to be of interest. These snapshots were then clustered into distinctive events using a subtractive clustering methodology. Clusters of snapshots are depicted in figure 5.15(d) where they are superimposed over the unwrapped (cumulative) phase signal.

Further investigation into these altered shedding events highlights the similarity to the shear layer instability phenomena, which develops through the action of a Kelvin-Helmholtz mechanism. Prasad & Williamson (1997) conduct a detailed investigation of this phenomenon in the near-wake of a cylinder subjected to laminar flow. The vortices that form in the separating shear layer generally scale with the thickness of the shear layer and are visually similar to those found in a plane mixing layer between two streams of differing velocity. These similarities stretch across to phenomena observed in this study. Prasad & Williamson (1997) show that shear layer development is significantly influenced by three-dimensional near-wake phenomena such as parallel and oblique shedding conditions. Note that these conditions refer to vortex

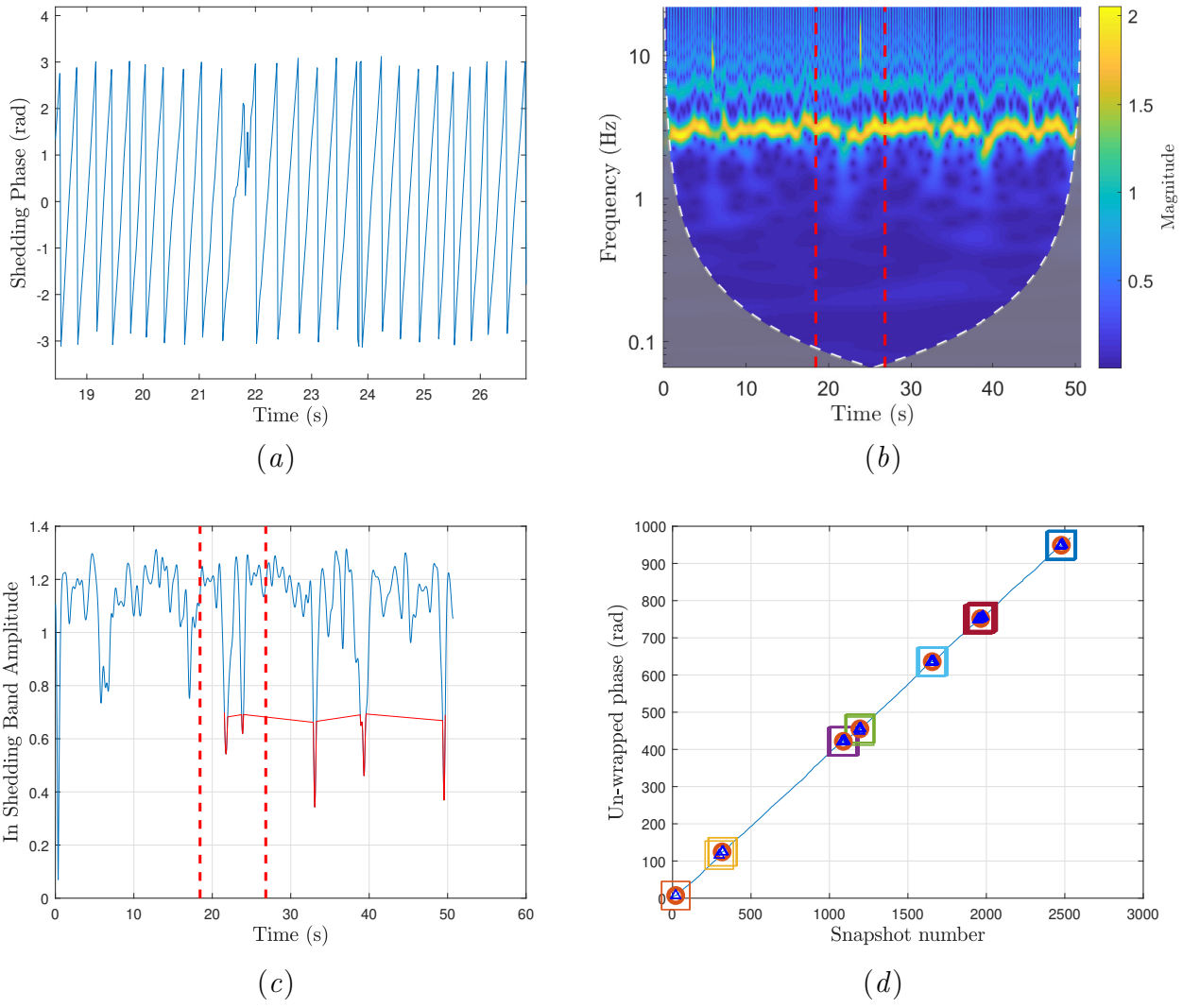

Figure 5.15: Plots describing the methodology to identify ID loss events. (a) Example of the phase signature of the OMD shedding mode during an ID loss event. (b) Magnitude scalogram of the continuous wavelet transform of the phase signal. (c) Amplitude within the shedding band as a function of time. The parts highlighted in red indicate regions of shifted frequency. The red dotted line in (b) and (c) outline the time window displayed in the top-left plot. (d) Clusters of identified ID loss events are superimposed on top of the cumulative phase.

tubes being shed either parallel to the cylinder axis or at an oblique angle to the cylinder axis respectively. Typically the oblique shedding angles are between 15 - 20° (Williamson, 1996). Prasad & Williamson (1997) control the shedding conditions by forcing them into the required condition with the use of inclined endplates. A clear peak is visible at the shear layer frequency for parallel conditions, whereas, it is suggested that the instability is moderated by oblique shedding conditions. Akin to the altered shedding events observed in this study, the shear layer instability is also inherently intermittent. Prasad & Williamson (1997) show that intermittency increases with both Reynolds number and downstream distance of the probe. Furthermore, they highlight the distinct possibility of spontaneous generation of three-dimensional structures akin to structures referred to as mode B by Williamson (1996), to contribute significantly to the intermittency. Mode B structures indicate three-dimensional streamwise structures that have a typical span-wise wavelength of 1 diameter. The intermittency of the instability observed in this study is investigated in figure 5.16. Figure 5.16(a) depicts the number of identified events (clusters) during a run. Figure 5.16(b), on the other hand aims to quantify intermittency as a percentage of the time period that is spent within identity loss events with respect to the total time. Whilst no clear trend with respect to subjected turbulence intensity is to be seen, the incoming integral length scale has a defining influence. Both, the number of observed events as well as the fraction of time when instability events are present, generally increase as a function of integral length scale. Run 2d continues to be an outlier with significantly reduced manifestation of identity loss events. It is likely that free-stream turbulence conditions with length scales of the order of 1 cylinder diameter cause an excitation of the instability similar to the previously discussed mode B structures.

Finally, it is possible to comment on three-dimensional flow structures downstream of the cylinder during the instability by utilising data collected by Marangon Cicolin (2020). They investigate flow downstream of cylinder control rod configurations, through planar PIV experiments on dual planes that are orthogonal to each other, allowing the collection of u, v and w velocities. Identity loss events can also been observed in their data-set. OMD analysis can be used on the data collected in the $x - y$ plane to identify instances of the altered shedding events. Data from the $x - z$ plane can then be used to comment on any spanwise structures.

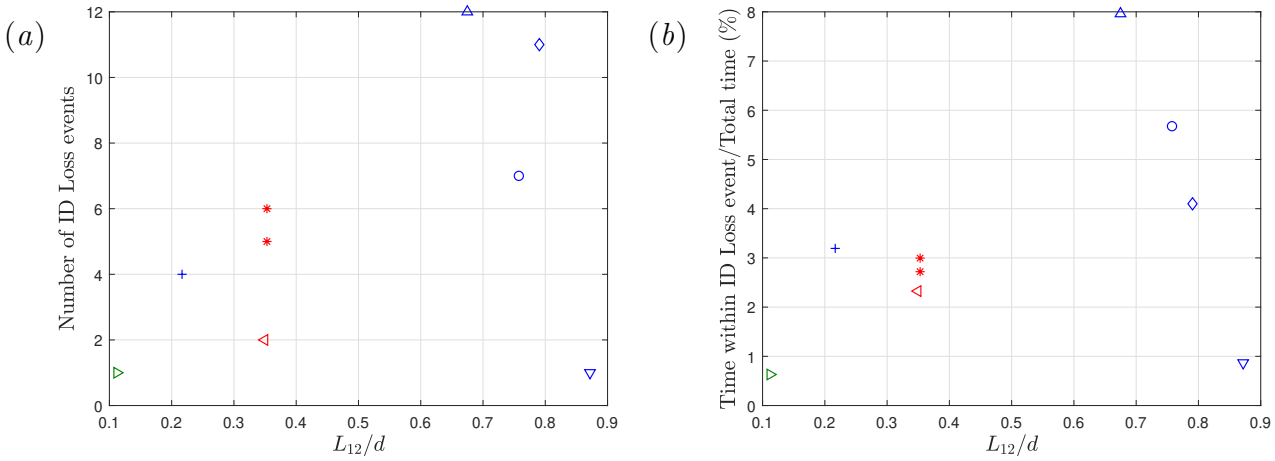

Figure 5.16: Intermittency as a function of subjected integral length scale. (a) Number of events where the instability occurred. (b) Percentage of time spent inside an ID loss event during the run.

Figure 5.17(a) depicts the flow-field during an identified altered shedding event. Dislocations in the spanwise component are clear to see, as it appears that the shedding mechanism is neither uniquely oblique or parallel during the event. On the other hand, 5.17(b) indicates the flow field during regular parallel shedding, where no dislocations are visible. This further adds to the evidence that manifestations of identity loss events are inherently controlled by three-dimensional structures. It is therefore plausible to reason that identity loss events are excited by the presence of length scale matched background turbulence as they provide an increased content of three-dimensional structures that are subjected to the cylinder.

Symmetrical vortex shedding behaviour that is observed during identity loss events is also very similar to the behaviour noticed by Barbi *et al.* (1986) and Konstantinidis & Balabani (2007) during their investigations of vortex shedding of a circular cylinder when subjected to oscillatory flow. Barbi *et al.* (1986) highlight the importance of lock-on behaviour by the subjected oscillatory flow that has a tendency of attracting the shedding frequency towards the driving frequency of the background for frequency ratios that are under the lock-on threshold. Most important to the current study, they show that for frequency ratios, $F_d/F_{s0} = 1$ (where F_d is the driving frequency and F_{s0} is the shedding frequency in steady conditions), two symmetric vortices are shed simultaneously for the cylinder in one cycle. Konstantinidis & Balabani (2007) specifically study this symmetrical shedding behaviour at a range of forcing frequencies. They

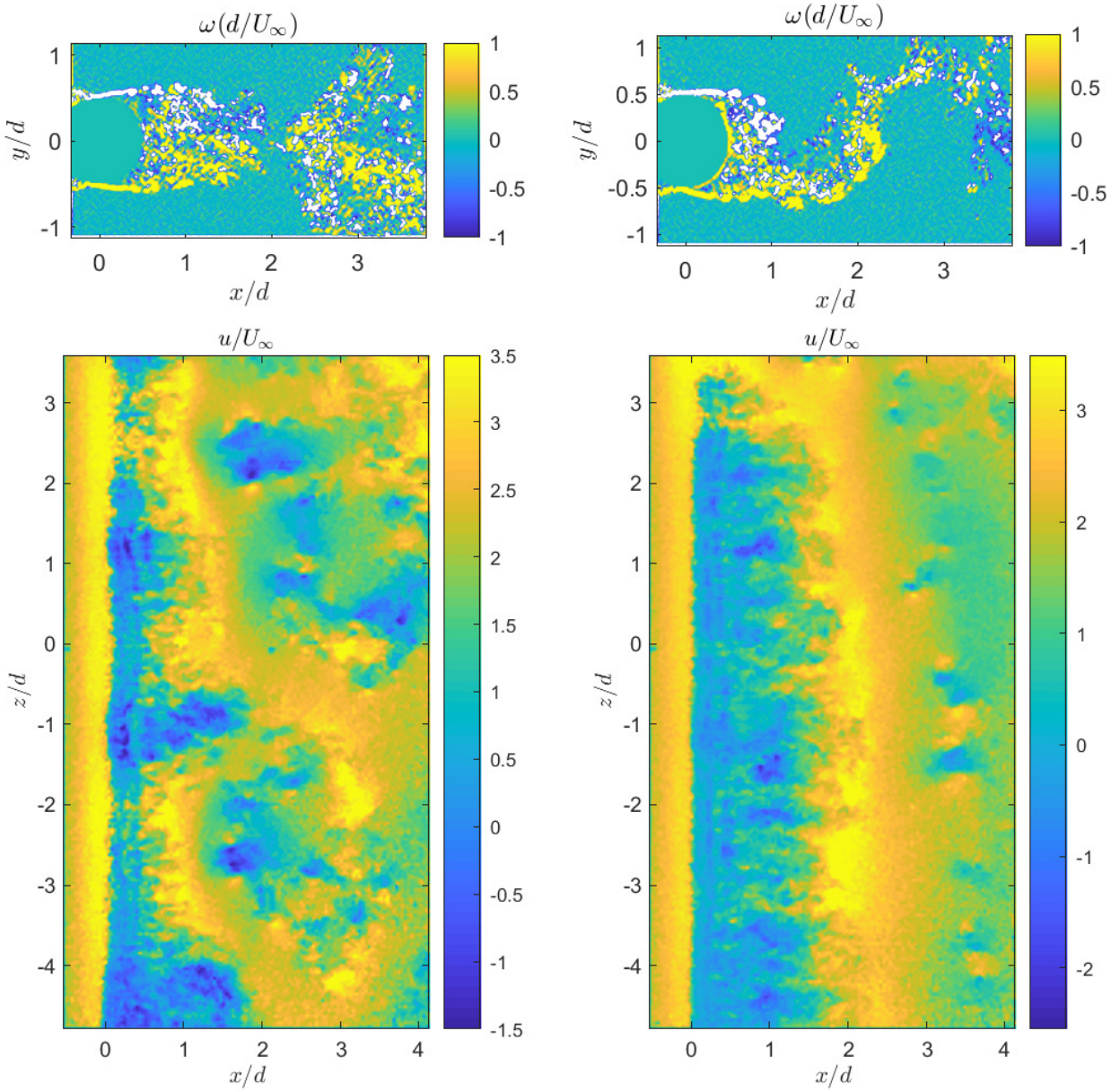

(*a*) Altered shedding event (*b*) Regular shedding

Figure 5.17: Spanwise flow structures during (*a*) an altered shedding event and (*b*) regular shedding. Note, the $x-z$ plane is located at $y=-0.5d$. Data obtained from Marangon Cicolin (2020)

show that symmetrical shedding is not stable and gives way to anti-symmetric shedding further downstream and also that the initial formation of the symmetric vortices on both sides of the cylinder is always phase locked to the subjected flow, thereby meaning that this behaviour is a direct consequence of the subjected symmetric perturbation. The subjected free-stream turbulence in this study is spectrally rich and it is possible that the upstream flow conditions may be conducive to conditions required to produce the symmetical shedding mode. It is however, imperative to highlight that Konstantinidis & Balabani (2007) lean on the shear layer instability behaviour outlined by Prasad & Williamson (1997) and state similarities between their two cases. The forcing flow (in their case) or the subjected free-stream turbulence (in this study) interacts with the separated shear layers to produce the observed phenomena.

The shear layer instability phenomena reported by Prasad & Williamson (1997) was observed to be on the whole, two-dimensional along the span and in phase across the wake. However, those experiments were conducted in a non-turbulent free-stream. Conditions in this study are unlikely to recreate the two-dimensionality observed by Prasad & Williamson (1997) due to the turbulent and dynamic nature of the flow subjected to the circular cylinder. Norberg (2003) provides a potential alternative explanation, should the altered shedding events not be two-dimensional along the span. They identify two shedding modes that co-exist within the sub-critical regime; namely, the "high quality" and "low quality" modes. They are named as such due to the spectral quality of the shedding frequency within each of the two modes. They explain that the *high quality* mode depicts fairly regular vortex shedding with only minor spanwise undulations of von Kármán shedding. Whereas, the *low quality* mode may be considered to be similar to identity loss events observed in this study. This mode is primarily governed by a Kelvin Helmholtz instability mechanism causing disruptions and random forcing to the vortex shedding process. Lastly, Norberg (2003) states that these disruptions lead to randomly positioned vortex dislocations along the span.

To summarise, the action of the incoming free-stream turbulence manifests itself through the formation of altered shedding events named as identity loss events due to the loss of similarity to regular vortex shedding. There are observed similarities to the shear layer instability phenomena and the action of incoming turbulence is seen to encourage the manifestation of these events.

More specifically, cases with higher length scale in the background turbulence are seen to increase the frequency at which the instability occurs. The intermittency of this behaviour is likely to be explained by the three-dimensional perturbations of the incoming flow. Structures with length scales that are similar to the diameter of the cylinder are likely to excite the observed phenomena. Finally, a couple of alternative explanations are also laid out for the reader.

5.4 Conclusions

The near-field development of a cylinder wake subjected to free-stream turbulence was experimentally examined using simultaneous PIV and PLIF experiments. The traditional conclusion of increased wake width in the near-field in the presence of free-stream turbulence was recovered when the time-averaged extent of the scalar was examined. However, this method lacked fidelity since it amalgamated the influence of both entrainment and meandering. It was shown that background length scale had a defining impact in the behaviour of near-field wake development. Cases with large length scales experienced a reduction in instantaneous wake width, whereas the increased level of meandering meant an overall increase in the traditionally averaged wake width compared to the no-grid case. Cases that had smaller length scales in the background turbulence experienced an increase in both entrainment and an increase in the level of meandering. This therefore resulted again in an overall increase in traditional wake width from a time-averaged perspective. It was shown that free-stream turbulence had a marked effect on both meandering as well as near-wake entrainment.

Secondly, the splitter plate experiment showed that an increase in instantaneous wake width was observed in the immediate vicinity of the cylinder even after vortex shedding was controlled in the wake. However, the shift in the effect of background turbulence on entrainment was clear to see as the wake continued to develop. Wake growth was stunted for $x/d > 8$ when background turbulence was introduced. This was not the case for the no-grid case, as the wake in this case, continued to grow steadily.

Lastly, altered shedding events that were named as identity loss events were investigated. Similarities with the shear layer instability phenomena were explored. It was found that cases with higher length scale in the background turbulence increased the frequency at which these events occurred. Finally, a potential excitation of the phenomena when encountered with structures with length scales similar to the diameter of the cylinder was discussed.

Chapter 6

Conclusion

6.1 Summary of Thesis Achievements

1. The turbulent/turbulent interface was identified for the first time, the existence of which was previously questioned in literature (da Silva *et al.*, 2014).

2. In the far wake of a circular cylinder, free-stream turbulence acts to suppress the entrainment rate into the wake. The main actor in this process is turbulence intensity as length scale is seen to only have a second order effect. The reduction in entrainment is driven by the action of high intermittency.

3. Entrainment mechanisms in the turbulent/turbulent interface differ from the turbulent/non-turbulent interface as the role of viscosity becomes insignificant when strain is introduced to the background. The inertial term is mainly responsible for the entrainment process in a turbulent background. Noting that the inertial term is also an intermittent quantity.

4. Background turbulence alters near-wake development by affecting both meandering as well as entrainment. Length scale of the background turbulence is pivotal in governing near-field behaviour, as the wake width calculated as a mean of the scalar extent increases when subjected to free-stream turbulence.

6.2 Future Work

The previous section aims to answer the main questions outlined as the objectives for this thesis in chapter 1. In the process of doing so, several other questions have inevitably been raised. These have been highlighted below and a brief explanation of the plan of action involved to answer each question has been suggested.

- *Is there a repeatable cause for the onset of extreme entrainment events that are of great significance in the far field?*

  This avenue of research aims to investigate extreme events that have a defining role in far-field entrainment. It may be possible to isolate these events and examine a potential correlation of instantaneous entrainment with the phase of the background flow (given that the flow has a phase signal that is discernible). Furthermore, local coherent structures in the background flow may prompt the onset of these extreme events. Therefore, an investigation into extreme entrainment events is suggested. Avenues of work that aim to analyse instantaneous entrainment are bound to be noisy and therefore a substantial sample size is required.

- *Can the investigation be spread to the entrainment of momentum and energy? What is the role of pressure?*

  The effect of background turbulence has been investigated on entrainment mass flux. However, when expanding this to momentum, the correlation of local fluid velocity, $\boldsymbol{u}$, and the local entrainment velocity, $\boldsymbol{V_\gamma}$, is of critical importance. Eddies that are locally present in the background flow will affect this relationship and thereby the entrainment process. Equation, 6.2, outlines this mathematically. Furthermore, the effect of pressure gradients on this process is also of interest.

$$Mass\ Flux = \rho \int \boldsymbol{V_\gamma}.d\boldsymbol{\xi} \tag{6.1}$$

$$Momentum\ Flux = \rho \int \boldsymbol{u}.\boldsymbol{V}_{\boldsymbol{\gamma}} d\boldsymbol{\xi} \tag{6.2}$$

- *Is it possible to quantify the rate of entrainment in the near wake of a circular cylinder?*

  It is known that the entrainment mechanisms in the near-wake are different to the mechanism in the far-field, due to the significant influence of the shed coherent structures. It has also been shown the effects of free-stream turbulence on an undeveloped wake are also rather different. In the presence of background turbulence, the wake sees an increased width in the near-field with the subjected length scale being the driving parameter. A high temporal resolution experiment in the near-field will allows us to ascertain the entrainment rate during the early stages of wake development. Along with a new experiment, algorithmic developments regarding how disconnected pockets of the wake, that readily appear in the near-field, need to be developed.

  Furthermore, scalar intensity analysis following a potential quantitative PLIF experiment may allow us to determine the extent of influence that engulfment has during wake infancy. Results provided in chapter 5 clearly highlight alternative mechanisms are key during wake growth in the near field. It is thought to be highly likely that in an intensely chaotic and coherent stage of wake development, engulfment plays a defining role. In order to quantify this, we propose to conduct a quantitative PLIF experiment to appropriately ascertain the scalar concentration along the full extent of the wake. Having access to this data will allow us accurately identify pockets of unmixed yet engulfed regions of fluid. Subsequent analysis could then lead to understanding the mechanisms of the engulfment process as well as the parameters of the background turbulence that are affecting it.

- *What are the effects of subjected three-dimensional structures on the shedding mechanism of the cylinder?*

  It has been asserted that the shedding mechanism of the cylinder is significantly influenced by three-dimensional structures in the vicinity of the cylinder. Evidence for this is presented both from literature as well as experimental data, and is reported in the final section of chapter §5. Having access to data on the $x - z$ plane as well as the $x - y$

plane will allow for careful interrogation of three dimensional structures at the onset of the instability.

- *Do identity loss events have a lasting impression on entrainment rate in the far-field?*

  The instantaneous entrainment rate was greatly affected by the onset of identity loss events in the near-field. This raises the question of whether these events have a lasting effect in the far-field. An attempt at evaluating this effect was undertaken during the project. However, it was not successful due to the existence of holes in the far-field entrainment data (see invalid snapshots: section C.4). The infrequent occurrences of identity loss events coupled with the lack of guaranteed far-wake entrainment data, meant that the sample size for any possible correlation was not large.

- *How does entrainment vary spatially?*

  The effects of free-stream turbulence have been investigated in the immediate vicinity of the cylinder as well as in the far wake approximately $40d$ downstream. It has been shown the entrainment effect is different for a wake that is still developing when compared to suppressed entrainment that is observed in the far wake. Results in §5.2.1 display the switch in the entrainment effect. A close investigation into the underlying causes of this change as well as broadening the measured spatial locations downstream of a wake is suggested.

Appendix A

Drawings

A.1 Splitter plate

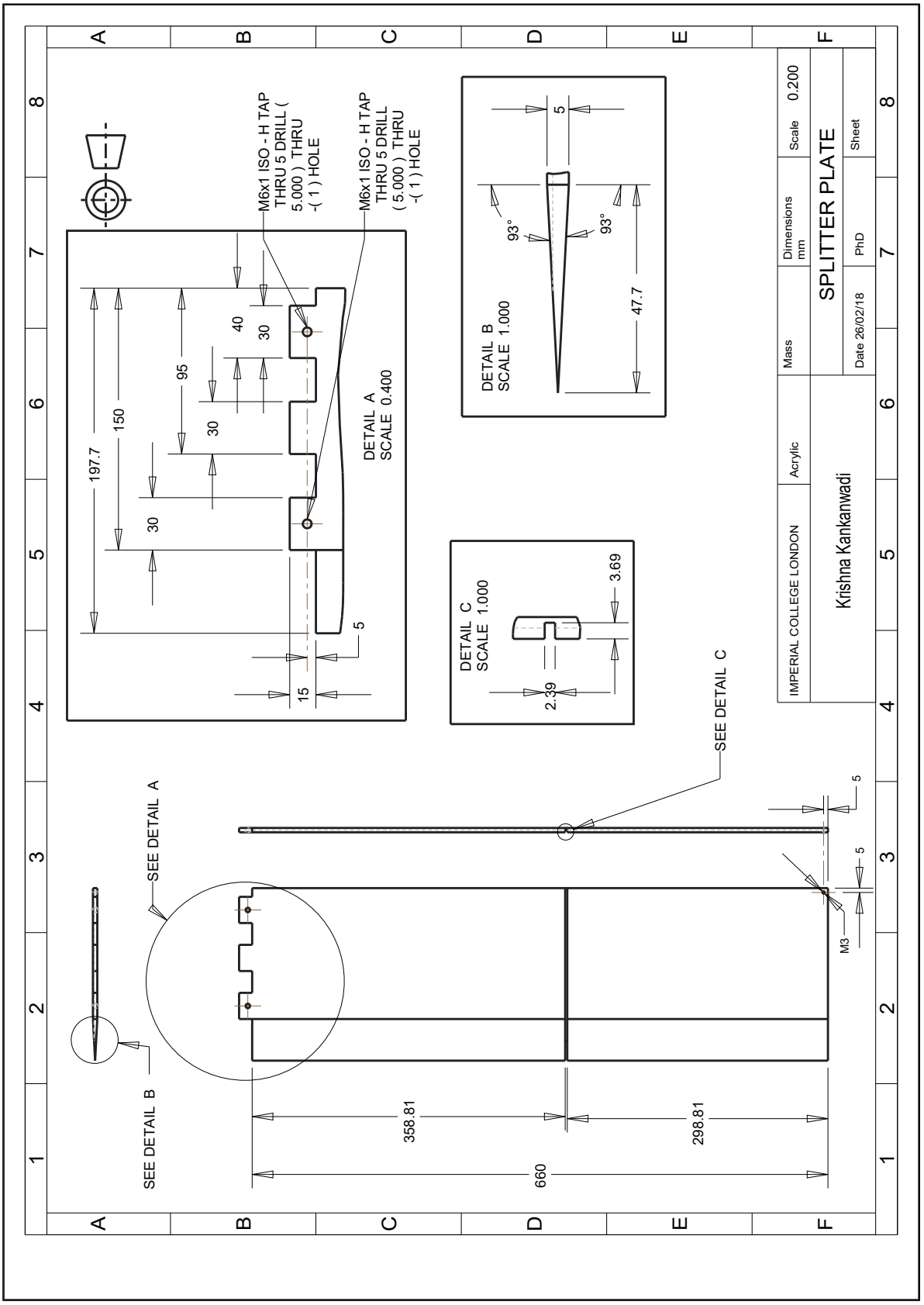

Engineering drawing of the splitter plate used for testing in campaign IV.

Appendix B

Grid characterisation pilot study

Three grids that resemble the turbulence generating grids used in this study, were first fully characterised in a previous study, reported in Kankanwadi (2017). These results have been reproduced here. However, these measurements were conducted at a slightly different Reynolds number, $Re_H \approx 2 \times 10^5$. Additionally, the external dimension was also reduced in these measurements since a slightly larger frame was used. The results of this pilot study are being presented as an appendix, since they allowed for a more focused grid characterisation campaign. This was especially true for the fractal grid SFG7. The equivalent grids are named with the suffix, '*'. The following figures depict the behaviour of length scale as well as turbulence intensity downstream of each equivalent grid. Note that these results were simply used as indicators to inform the grid characterisation campaign reported in §2.2.2. The same due care that was taken for processing results presented in §2.2.2 was not afforded here.

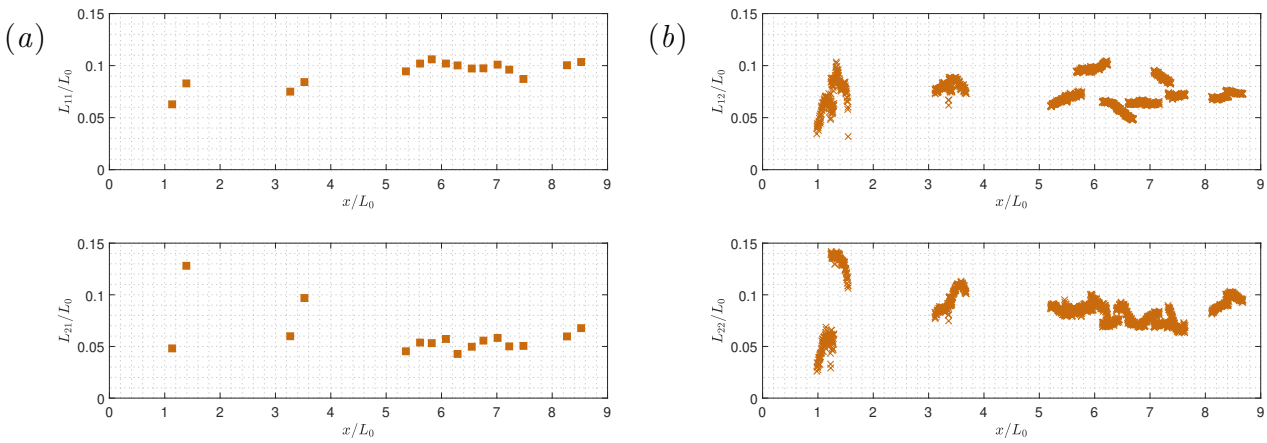

Figure B.1: SFG5* - Correlation length scale as a function of streamwise distance.

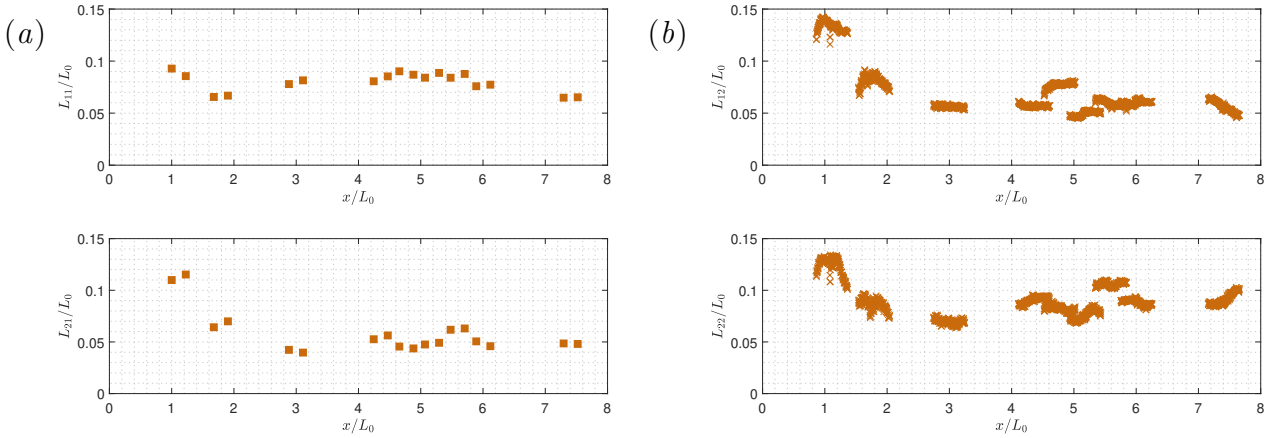

Figure B.2: SFG7* - Correlation length scale as a function of streamwise distance.

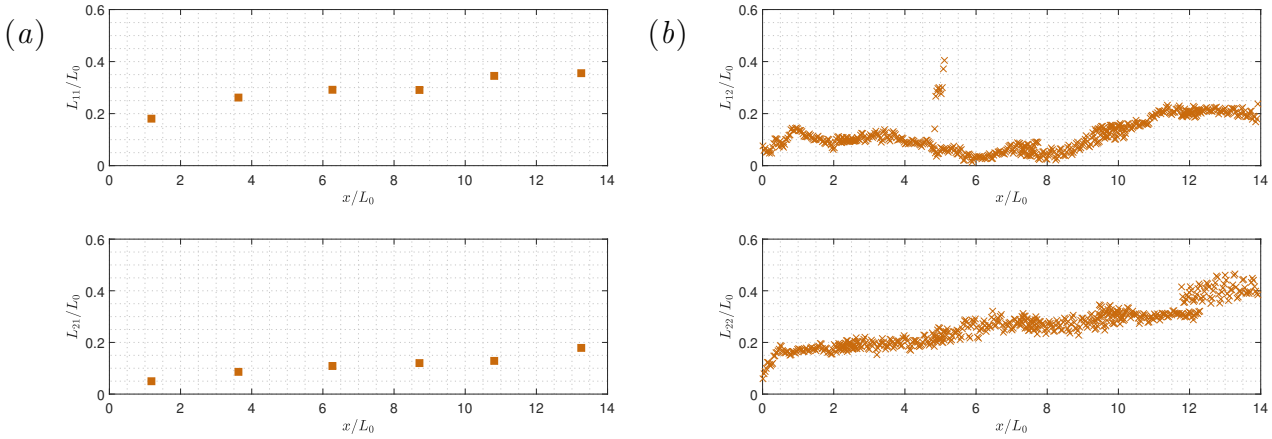

Figure B.3: SRG38* - Correlation length scale as a function of streamwise distance.

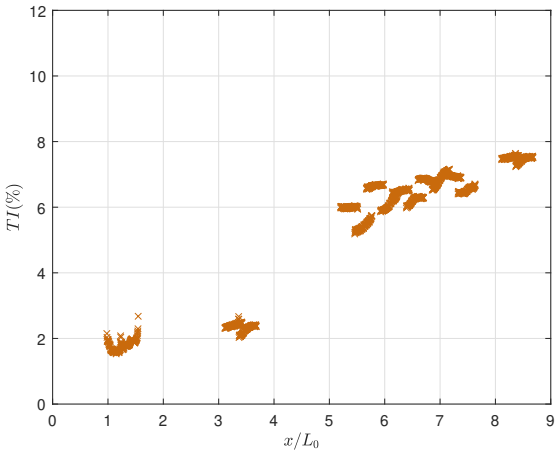

(a) SFG5*

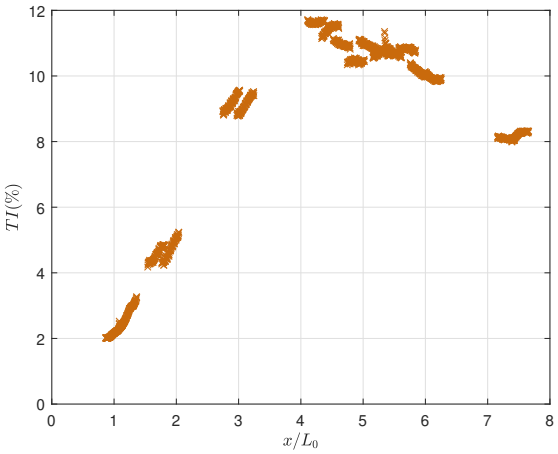

(b) SFG7*

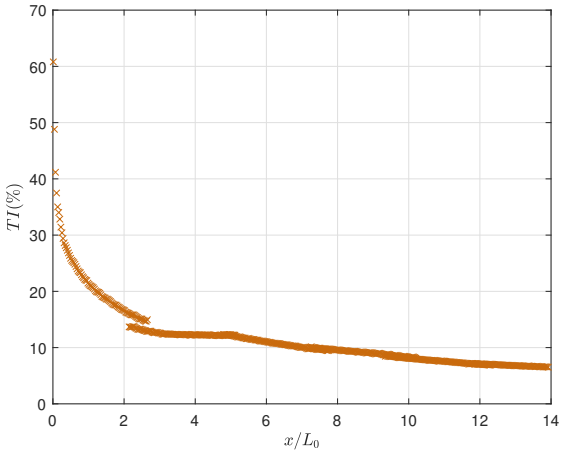

(c) SRG38*

Figure B.4: Turbulence intensity as a function of streamwise distance downstream of equivalent grids.

Appendix C

Campaign II

C.1 Field of view locations for runs conducted in campaign II

Figures C.1 to C.4 depict the turbulence intensity field as well as the locations of the field of view for runs conducted in campaign II. Note that, in all figures, the position of the cylinder as well as the extent of the field of view is clearly highlighted. In the cases where multiple run configurations are shown in the same figure, the cylinder and the boundary of the field of view are colour matched.

C.2 Further validation of wake boundary detection methodology

To further validate the experimental methodology utilised to identify the wake boundary, conditional enstrophy jumps calculated using two different approaches are compared. A light intensity gradient based methodology, as used in this experiment, is validated against a vorticity boundary calculated by examining enstrophy gradients. Note that the latter is a good

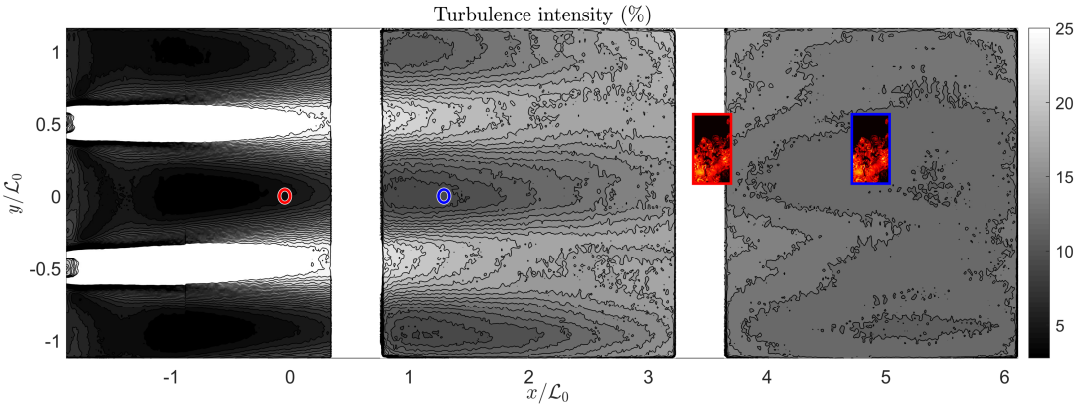

Figure C.1: Turbulence intensity profile downstream of a square regular grid with $\mathcal{L}_0 = 111$ mm. The overlays represent the investigated FOVs. The positioning of the grid, cylinder and the experimental FOV are consistent with that of runs 3b & 3c for the red outline. Whereas the blue outline highlights the positioning for run 3a.

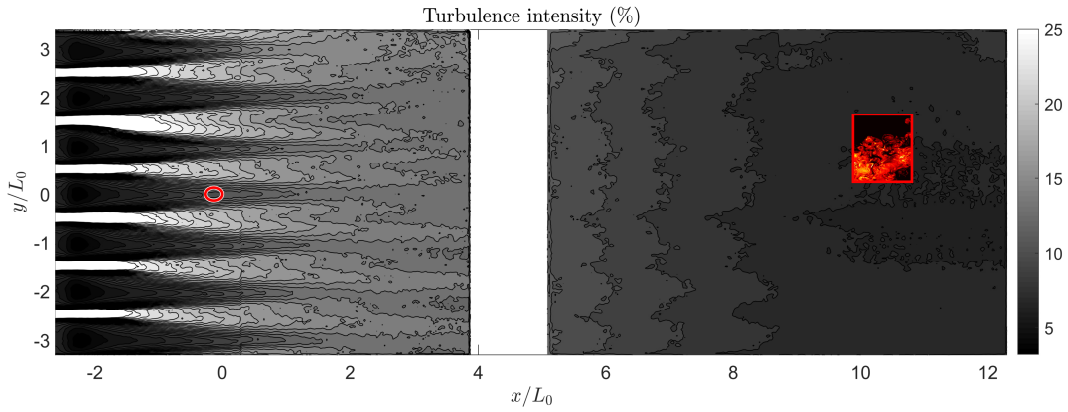

Figure C.2: Turbulence intensity profile downstream of a square regular grid with $\mathcal{L}_0 = 38$ mm. The overlays represent the investigated FOVs. The positioning of the grid, cylinder and the experimental FOV are consistent with that of run 2b.

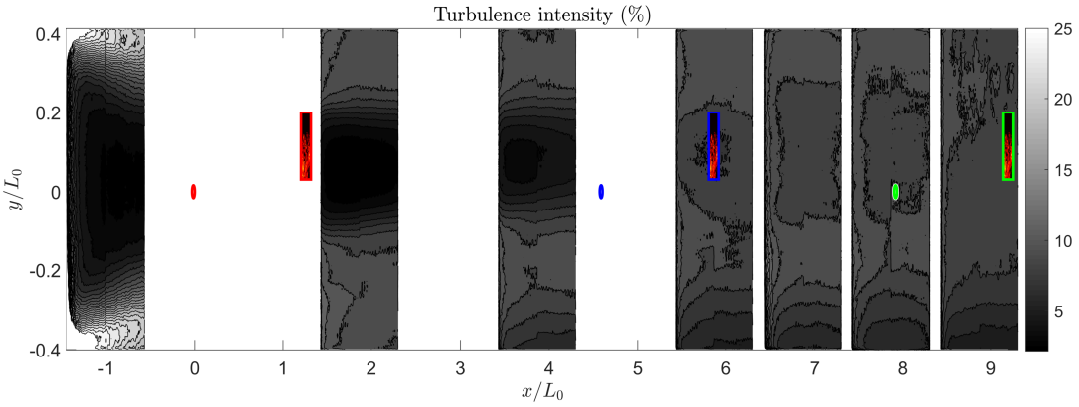

Figure C.3: Turbulence intensity profile downstream of a square fractal grid with $\mathcal{L}_0 = 312$ mm. The overlays represent the investigated FOVs. The positioning of the grid, cylinder and the experimental FOV as defined by the red outline are consistent with that of run 1b. The blue outline represents run 2c, whereas the green outline represents run 2d.

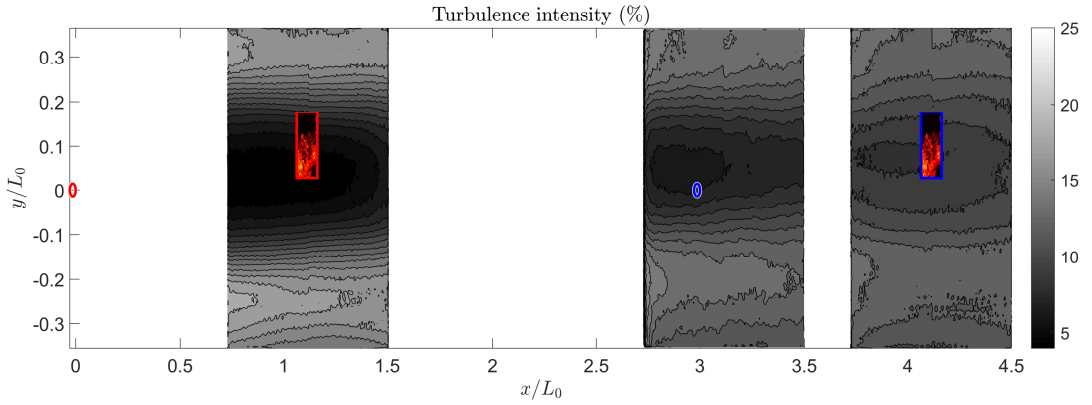

Figure C.4: Turbulence intensity profile downstream of a square fractal grid with $\mathcal{L}_0 = 354$ mm. The overlays represent the investigated FOVs. The positioning of the grid, cylinder and the experimental FOV are consistent with that of run 2a for the red outline. Whereas the blue outline highlights the positioning for run 2e.

control case as it is independent of the PLIF experiment. A comparison of this kind is only meaningful if the background flow lacks a significant amount of rotational flow. Therefore, this validation is conducted on the dataset produced from the no-grid case (run 1a).

Experimental vorticity data are inherently very noisy and hence finding a continuous contour of enstrophy across the entire field of view is not consistently possible. Therefore, a median filter is applied to the velocity vectors prior to the calculation of vorticity. Furthermore, a median filter is also applied to the resulting enstrophy to produce an enstrophy field that is conducive to evaluating a continuous contour along the wake boundary. However, even after these measure it is not possible to evaluate a continuous contour on all snapshots. In several cases the contour identifies an internal interface in the bulk of the wake, thereby outputting a non-physical contour of the outer boundary. Hence, all snapshots where the mean difference between the contours using the two different methodologies are greater than a chosen threshold are discarded from the validation process. Note that the sensitivity to this threshold is also investigated and reported in figure C.5.

Examining the behaviour of normalised enstrophy for all cases displayed in figure C.5, it is evident that the sharp rise in the metric occurs at the same region of $\gamma = 0$ regardless of the size of the dataset chosen to be examined. Furthermore, we also highlight that the level in the turbulent bulk and the free-stream collapse. However, discrepancies do exist between

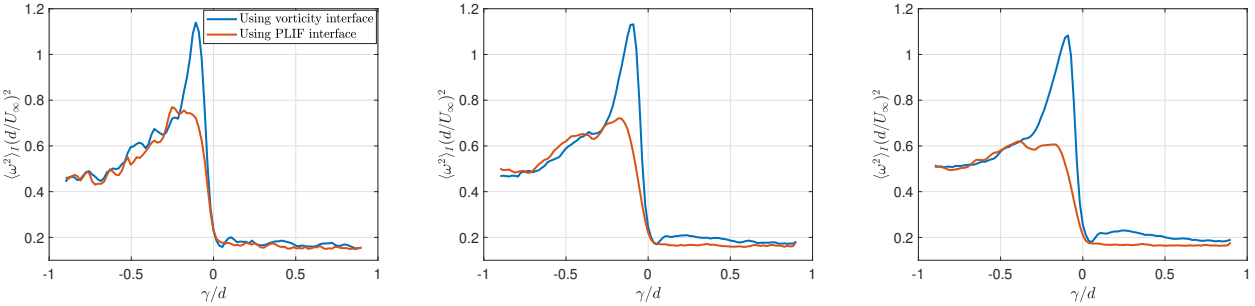

(*a*) Threshold = 1 mm
Valid snapshots = 73

(*b*) Threshold = 2.5 mm
Valid snapshots = 402

(*c*) Threshold = 4 mm
Valid snapshots = 726

Figure C.5: Interface conditioned statistics as a function of normal distance away from the wake boundary identified by both the PLIF data as well as the vorticity data. The series of figures illustrate the sensitivity to the chosen threshold. Captions of each panel represent the chosen threshold difference between the contours identified using the two different methodologies as well as the number of valid snapshots that consist of valid contours using both methodologies and pass the threshold test.

the two conditional plots and this is especially evident by examining the correlation near the enstrophy peak. This lack of correlation should be expected as the experimental methodology within campaign II can only collect a single component of vorticity. Visual examination of the snapshots reveals instances where the scalar extent is greater than that of the concentrated bulk of vorticity, hence resulting in a reduced peak of mean enstrophy just inside the scalar boundary. Despite the lack of correlation at the peak, the jump at $\gamma = 0$ in this analysis combined with the respective conditional jumps for enstrophy as well as PLIF light intensity proves that the scalar is faithfully mixed within the entire extent of the wake.

C.3 Thickness of the turbulent interface

This section details the thickness of the identified turbulent/non-turbulent interface as a function of both the Taylor and Kolmogorov scales. It has been omitted from the main part of the thesis since the scalings outlined in this section are for reference only. In order to establish a true scaling for the interface, experiments over a large range of Reynolds numbers are necessary, which is not present within this study. After considering figure 3.4, it may be possible to estimate the enstrophy adjustment region of run 1a (TNTI) to be equivalent to $0.2d$. Using the Taylor scale and Kolmogorov scale, calculated for the no-grid case, $0.2d$ is equivalent to

approximately 0.7λ and 12.5η. These scalings are in line with TNTI thicknesses observed in literature (Silva *et al.*, 2018). For further detail, the reader is advised to refer to Silva *et al.* (2018), who collate previously observed scalings in addition to detailing the relationship of the thickness of the TNTI and it's sublayers, with both the Taylor and the Kolmogorov scale.

C.4 Data clean up: Removing unphysical entrainment velocities from the flux calculation

The data cleaning process is designed to ensure that the final entrainment mass flux result is a true reflection of the physical phenomenon and is not adversely affected by numerical or algorithmic artefacts. Firstly, the baseline procedure disregards snapshots that do not include the wake boundary covering the full extent of the field of view. The data cleaning process is then implemented on this subset of snapshots. Prior to outlining this process, it is important to address its necessity. Unphysical entrainment velocity vectors creep into the algorithmic procedure when the contour that is identified as the wake boundary drastically (and unrealistically) changes shape between two consecutive snapshots. This may occur when an overhanging eddy either leaves or enters the field of view between a pair of snapshots. As the treatment mechanism identifies the point that is furthest away from the core of the wake to represent the wake boundary, this can lead to a misleading result that claims a large amount of either entrainment or detrainment. This process is illustrated in figure C.6. Similarly, large additions and removals from the instantaneous wake interface may also occur when a 'three-dimensional reconnection event' or the PIV plane traverses a wake structure in the form of a 'teacup handle'. Therefore, these instances need to be rejected from the flux calculation. Furthermore, the entrainment velocity vectors that are calculated in the near vicinity of any artificial cliffs also need to be accounted for. In order to eliminate any invalid vectors that can arise due to the reasons specified above, the following steps were taken.

1. Using all snapshots that pass the baseline filter (as discussed above), a first pass of calculating the entrainment velocity vectors was conducted. This set of calculated velocity

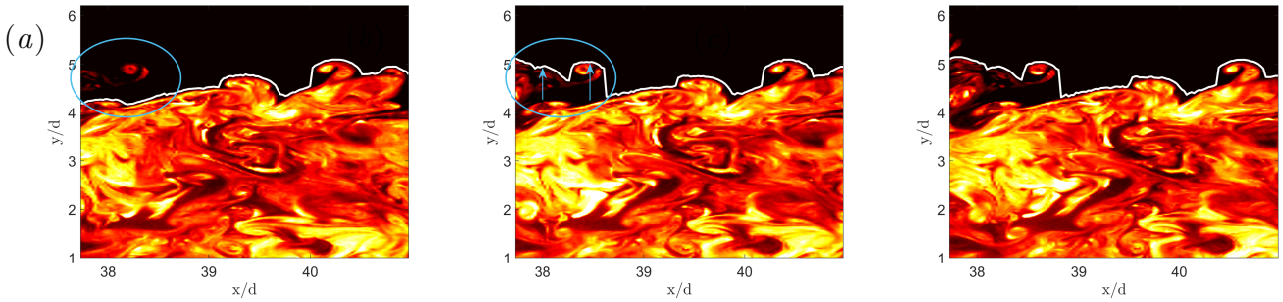

Figure C.6: Artificial cliffs in the contour as a result of eddies entering the field of view. (a) Snapshot at time, t_0 (b) Snapshot at time, $t_0 + \Delta t$ (c) Snapshot at time, $t_0 + 2\Delta t$

vectors was then used to evaluate a first pass mean (μ_{fp}) and standard deviation (σ_{fp}).

2. Next, a maximum and a minimal valid velocity magnitude was calculated using, Max&Min valid velocity = $\mu_{fp}\pm$ cutoff coefficient $\times\sigma_{fp}$. The selected cutoff coefficient for this study was equal to 2.4. Note that the value for this coefficient was carefully selected upon conducting a sensitivity study and ensuring that the mean entrainment mass flux was insensitive to a deviation of the cutoff coefficient in the neighbourhood of the selected value. These limits were used to produce a subset of valid entrainment velocity vectors.

3. The vectors that were located adjacent to artificial cliffs were considered to be invalid.

4. Finally, any snapshot that had greater than 40% invalid vectors, was discarded from the flux calculations. Note that a similar sensitivity study as above was conducted for the 40% value and a robust and insensitive percentage was chosen.

Upon the completion of this process, the valid entrainment velocity vectors within each snapshot were integrated in segments that were split by any invalid vectors. The result of all of these segments were summed and the entrainment mass flux value for the snapshot was determined.

Appendix D

Near wake

D.1 Threshold study

This section details the threshold study conducted to evaluate the sensitivities of the wake width calculated using the time average of the scalar extent. Plots in figure D.1 show the same metric over a wide range of threshold values. The threshold value itself represents the probability that a particular point is present inside the wake over the time series. The threshold values range from the 5% in figure D.1(a) to 25% in figure D.1(e). As expected the absolute value of wake width increases for lower threshold probabilities. However, most important are the relative widths of each run. Even with a significant change in the threshold value, trends of each run remain the same. Thereby, our qualitative conclusions are insensitive to the chosen threshold value.

D.2 Spectral analysis

Examining the spectra of each of the runs revealed that background turbulence led to a shift in the shedding frequency. This behaviour is depicted in figure D.2, where the power spectral density is plotted as a sweep across the y-extent of the field of view. The x-position of the probe

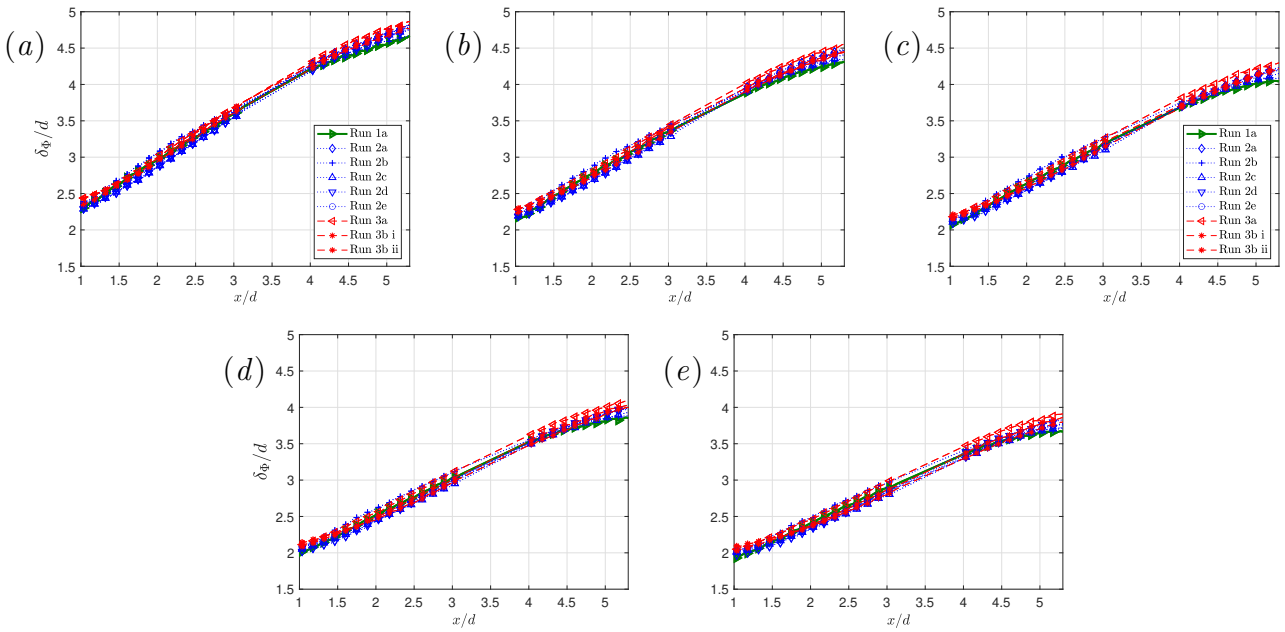

Figure D.1: Traditional wake width threshold sensitivity study. (a),(b),(c),(d) and (e) refer to threshold values of 5%,10%,15%,20% and 25% respectively.

is located halfway between the rear face of the cylinder and the maximal streamwise extent of the field of view.

Considering all the runs with applied free-stream turbulence (not plotted), a shift in the main shedding peak is clear to see, however no discernible pattern can be established as to which parameters of the background turbulence most affect this behaviour or even as to in which way background turbulence acts to shift the shedding peak. Certain cases of background turbulence are seen to increase the Strouhal number, whereas the opposite behaviour is noticed in some other cases.

In most cases with subjected background turbulence, a broadening of the shedding peak is observed as vortex shedding is spread over a larger frequency band. This behaviour is similar to the wide shedding band observed by Bearman (1969) when a small perturbation has been placed on the surface of the cylinder. Bearman (1969) explained that disturbances on the cylinder surface tripped the boundary layer ahead of the laminar separation bubble and locally tripped it. They further explain that the reason for regular shedding ceasing is due to gross three-dimensionality of the flow caused by the disturbances on the surface disrupting the separation bubbles. It is likely that applied free-stream turbulence disturbs the regular laminar separation

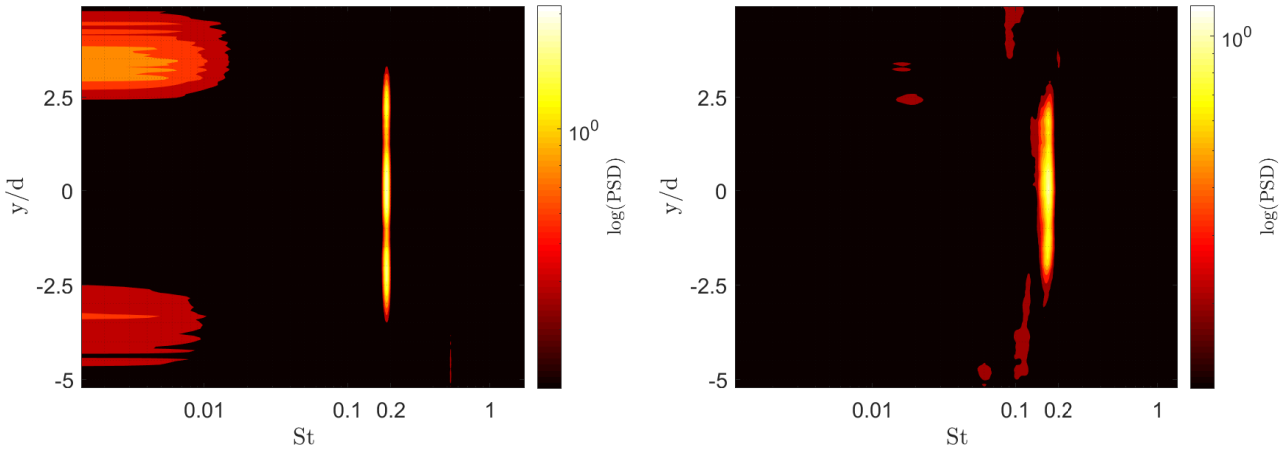

(*a*) Run 1a - No-grid case (*b*) Run 2a

Figure D.2: y-position sweeps of power spectral density at $x/d = 2.8d$ for a no-grid case and a case with subjected background turbulence.

in the sub-critical regime and thereby contributes to broad-band shedding.

Sadeh & Brauer (1980); Sadeh & Saharon (1982) and Kwok (1986) examined the effect of grid generated and rod generated turbulence on flow near the front stagnation region of a circular cylinder. Sadeh & Saharon (1982) concluded that boundary layer flow similar to the flow that can be found in the super-critical regime could be found in the sub-critical regime when subjected to background turbulence and concluded that the effect of free-stream turbulence was equivalent to an increase in "effective" Reynolds number. Bearman & Morel (1983) explained that packaging the effects of free-stream turbulence as an increase in "effective" Reynolds number was inherently flawed. The results depicted in this section further support the argument laid out by Bearman & Morel (1983) since no clear increase in Strouhal number is observed under turbulent free-stream conditions, as one might expect for a cylinder that naturally enters the critical regime (Bearman, 1969).

Bibliography

Ainslie, J.F. 1988 Calculating the flowfield in the wake of wind turbines. *Journal of Wind Engineering and Industrial Aerodynamics* **27** (1), 213–224.

Apelt, C. J. & West, G. S. 1975 The effects of wake splitter plates on the flow past a circular cylinder in the range lo4 < R < 5 x lo4. Part 2. *Journal of Fluid Mechanics* **71** (1), 145–160.

Arcoumanis, C., McGuirk, J. J. & Palma, J. M. L. M. 1990 On the use of fluorescent dyes for concentration measurements in water flows. *Experiments in Fluids* **10** (2), 177–180.

Atreya, S.K., Wong, M.H., Owen, T.C., Mahaffy, P.R., Niemann, H.B., de Pater, I., Drossart, P. & Encrenaz, Th 1999 A comparison of the atmospheres of jupiter and saturn: deep atmospheric composition, cloud structure, vertical mixing, and origin. *Planetary and Space Science* **47** (10), 1243–1262.

Baj, Paweł 2018 Experimental investigation of wake development and mixing behind a multi-scale array of bars - *PhD thesis* .

Baj, P., Bruce, P. J. K. & Buxton, O. R. H. 2015 The triple decomposition of a fluctuating velocity field in a multiscale flow. *Physics of Fluids* **27** (7).

Baj, P., Bruce, P. J. K. & Buxton, O. R. H. 2016 On a PLIF quantification methodology in a nonlinear dye response regime. *Experiments in Fluids* **57** (6), 1–19.

Baj, P. & Buxton, O. R. H. 2019 Passive scalar dispersion in the near wake of a multi-scale array of rectangular cylinders. *Journal of Fluid Mechanics* **864**, 181–220.

Baker, Robert W. & Walker, Stel N. 1984 Wake measurements behind a large horizontal axis wind turbine generator. *Solar Energy* **33** (1), 5–12.

Barbi, C., Favier, D. P., Maresca, C. A. & Telionis, D. P. 1986 Vortex Shedding and Lock-on of a Circular-Cylinder in Oscillatory Flow. *Journal of Fluid Mechanics* **170** (1973), 527–544.

Bastankhah, Majid & Porté-Agel, Fernando 2014 A new analytical model for wind-turbine wakes. *Renewable Energy* **70**, 116–123, special issue on aerodynamics of offshore wind energy systems and wakes.

Batchelor, George Keith 1953 *The theory of homogeneous turbulence*. Cambridge university press.

Bearman, P. W. 1965 Investigation of the flow behind a two-dimensional model with a blunt trailing edge fited with splitter plates. *Journal of Fluid Mechanics* **21**, 241–255.

Bearman, P. W. 1969 On vortex shedding from a circular cylinder in the critical Reynolds number regime. *J . Fluid Mech* **37** (3), 577–585.

Bearman, P. W. & Morel, T. 1983 Effect of free stream turbulence on the flow around bluff bodies. *Progress in Aerospace Sciences* **20** (2-3), 97–123.

Betchov, R. 1956 An inequality concerning the production of vorticity in isotropic turbulence. *Journal of Fluid Mechanics* **1** (5), 497–504.

Bisset, D. K., Hunt, J. C. R. & Rogers, M. M. 2002 The turbulent/non-turbulent interface bounding a far wake. *Journal of Fluid Mechanics* **451**, 383–410.

Breda, M. & Buxton, O. R. H. 2019 Behaviour of small-scale turbulence in the turbulent/non-turbulent interface region of developing turbulent jets. *Journal of Fluid Mechanics* **879**, 187–216.

Burridge, H. C., Parker, D. A. & Kruger, E. S. 2017 Conditional sampling of a high Peclet number turbulent plume and the implications for entrainment. *J. Fluid Mech* **823**, 26–56.

Buxton, O. R. H., Breda, M. & Dhall, K. 2019 Importance of small-scale anisotropy in the turbulent / nonturbulent interface region of turbulent free shear flows. *Physical Review Fluids* **4** (3), 1–17.

Canny, John 1986 A computational approach to edge detection. *IEEE Transactions on Pattern Analysis and Machine Intelligence* **PAMI-8** (6), 679–698.

Cantwell, B. J. & Coles, D. 1983 An experimental study of entrainment and transport in the turbulent near wake of a circular cylinder. *Journal of Fluid Mechanics* **136**, 321–374.

Chauhan, K., Philip, J., De Silva, C. M., Hutchins, N. & Marusic, I. 2014 The turbulent/non-turbulent interface and entrainment in a boundary layer. *Journal of Fluid Mechanics* **742**, 119–151.

Ching, C. Y., Fernando, H. J. S. & Robles, A. 1995 Breakdown of line plumes in turbulent environments. *Journal of Geophysical Research: Oceans* **100** (C3), 4707–4713.

Cimarelli, A., Cocconi, G., Frohnapfel, B. & De Angelis, E. 2015 Spectral enstrophy budget in a shear-less flow with turbulent/non-turbulent interface. *Physics of Fluids* **27** (12).

Comte-Bellot, Geneviéve & Corrsin, Stanley 1966 The use of a contraction to improve the isotropy of grid-generated turbulence. *Journal of Fluid Mechanics* **25** (4), 657–682.

Corrsin, S. & Kistler, A. L. 1955 Free-stream boundaries of turbulent flows. *NACA technical report* (1244).

Dahm, WJA & Dimotakis, PE 1987 Measurements of entrainment and mixing in turbulent jets. *AIAA journal* **25** (9), 1216–1223.

Dahm, Werner JA & Dimotakis, Paul E 1990 Mixing at large schmidt number in the self-similar far field of turbulent jets. *Journal of Fluid Mechanics* **217**, 299–330.

Eames, I., Jonsson, C. & Johnson, P. B. 2011 The growth of a cylinder wake in turbulent flow. *Journal of Turbulence* (12), N39.

Elsinga, G. E. & da Silva, C. B. 2019 How the turbulent/non-turbulent interface is different from internal turbulence. *Journal of Fluid Mechanics* **866**, 216–238.

Foucaut, Jean-Marc, Carlier, Johan & Stanislas, Michel 2004 Piv optimization for the study of turbulent flow using spectral analysis. *Measurement Science and Technology* **15** (6), 1046.

Ganapathisubramani, B., Lakshminarasimhan, K. & Clemens, N T 2007 Determination of complete velocity gradient tensor by using cinematographic stereoscopic PIV in a turbulent jet. *Experiments in Fluids* pp. 923–939.

Gaskin, S. J., McKernan, M. & Xue, F. 2004 The effect of background turbulence on jet entrainment: an experimental study of a plane jet in a shallow coflow. *Journal of Hydraulic Research* **42** (5), 533–542.

Gomes-Fernandes, R., Ganapathisubramani, B. & Vassilicos, J. C. 2012 Particle image velocimetry study of fractal-generated turbulence. *Journal of Fluid Mechanics* **711**, 306–336.

Hasager, Charlotte Bay, Rasmussen, Leif, Peña, Alfredo, Jensen, Leo E & Réthoré, Pierre-Elouan 2013 Wind farm wake: The horns rev photo case. *Energies* **6** (2), 696–716.

Herpin, Sophie, Wong, Chong Yau, Stanislas, Michel & Soria, Julio 2008 Stereoscopic piv measurements of a turbulent boundary layer with a large spatial dynamic range. *Experiments in fluids* **45** (4), 745–763.

Holzner, M. & Lüthi, B. 2011 Laminar superlayer at the turbulence boundary. *Physical Review Letters* **106** (13), 134503.

Hurst, D. & Vassilicos, J. C. 2007 Scalings and decay of fractal-generated turbulence. *Physics of Fluids* **19** (10).

Hussain, K. M. F. & Reynolds, W. C. 1970 The mechanics of an organized wave in turbulent shear flow. *J. Fluid Mech.* **41**, 241–258.

Jensen, NO 1983 A note on wind turbine interaction. *Riso-M-2411, Risoe National Laboratory, Roskilde, Denmark* p. 16.

Jiménez, J., Hoyas, S., Simens, M. P. & Mizuno, Y. 2010 Turbulent boundary layers and channels at moderate Reynolds numbers. *Journal of Fluid Mechanics* **657**, 335–360.

Kankanwadi, Krishna S. 2017 Effects of free stream turbulence on entrainment into a cylinder wake - *Master's thesis* .

Kankanwadi, Krishna S. & Buxton, Oliver R. H. 2020 Turbulent entrainment into a cylinder wake from a turbulent background. *Journal of Fluid Mechanics* **905**, A35.

Kankanwadi, Krishna S. & Buxton, Oliver R. H. 2021 Turbulent/turbulent entrainment. In *Progress in Turbulence IX* (ed. Ramis Örlü, Alessandro Talamelli, Joachim Peinke & Martin Oberlack), pp. 13–19. Cham: Springer International Publishing.

Khorsandi, Babak, Gaskin, S & Mydlarski, L 2013 Effect of background turbulence on an axisymmetric turbulent jet. *Journal of fluid mechanics* **736**, 250–286.

Konstantinidis, E. & Balabani, S. 2007 Symmetric vortex shedding in the near wake of a circular cylinder due to streamwise perturbations. *Journal of Fluids and Structures* **23** (7), 1047–1063.

Kwok, K. C. S. 1986 Turbulence Effect on Flow around Circular-Cylinder. *Journal of Engineering Mechanics-Asce* **112** (11), 1181–1197.

Laizet, S. & Vassilicos, J. C. 2012 Fractal space-scale unfolding mechanism for energy-efficient turbulent mixing. *Physical Review E - Statistical, Nonlinear, and Soft Matter Physics* **86** (4), 1–5.

Mandelbrot, B. B. 1983 The fractal geometry of nature **173**.

Marangon Cicolin, Murilo 2020 Manipulating the flow over a circular cylinder with control rods - *PhD thesis* .

Mathew, Joseph & Basu, Amit J 2002 Some characteristics of entrainment at a cylindrical turbulence boundary. *Physics of Fluids* **14** (7), 2065–2072.

Mazellier, N. & Vassilicos, J. C. 2010 Turbulence without Richardson-Kolmogorov cascade. *Physics of Fluids* **22** (7), 1–25.

Melina, G., Bruce, P. J. K., Hewitt, G. F. & Vassilicos, J. C. 2017 Heat transfer in production and decay regions of grid-generated turbulence. *International Journal of Heat and Mass Transfer* **109**, 537–554.

Mistry, D., Philip, J., Dawson, J. R. & Marusic, I. 2016 Entrainment at multi-scales across the turbulent/non-turbulent interface in an axisymmetric jet. *Journal of Fluid Mechanics* **802**, 690–725.

Niayifar, Amin & Porté-Agel, Fernando 2016 Analytical modeling of wind farms: A new approach for power prediction. *Energies* **9** (9).

Norberg, C. 2003 Fluctuating lift on a circular cylinder: review and new measurements. *Journal of Fluids and Structures* **17** (1), 57–96.

Perrin, R., Braza, M., Cid, E., Cazin, S., Moradei, F., Barthet, A., Sevrain, A. & Hoarau, Y. 2006 Near-wake turbulence properties in the high reynolds number incompressible flow around a circular cylinder measured by two- and three-component PIV. *Flow, Turbulence and Combustion* **77** (1-4), 185–204.

Philip, J., Meneveau, C., de Silva, C. M. & Marusic, I. 2014 Multiscale analysis of fluxes at the turbulent/non-turbulent interface in high Reynolds number boundary layers. *Physics of Fluids* **26** (1).

Pope, Stephen B. 2000 *Turbulent Flows*. Cambridge University Press.

Prasad, Anil & Williamson, C. H. K. 1997 The instability of the shear layer separating from a bluff body. *Journal of Fluid Mechanics* **333**, 375–402.

Raffel, M., Willert, Christian, Wereley, Steve & Kompenhans, Juergen 2007 *Particle Image Velocimetry: A Practical Guide*.

Reynolds, W. C. & Hussain, A. K. M. F. 1972 The mechanics of an organized wave in turbulent shear flow. Part 3. Theoretical models and comparisons with experiments. *Journal of Fluid Mechanics* **54** (02), 263.

Romano, GP, Antonia, RA & Zhou, Tongming 1999 Evaluation of lda temporal and spatial velocity structure functions in a low reynolds number turbulent channel flow. *Experiments in fluids* **27** (4), 368–377.

de Rooy, Wim C., Bechtold, Peter, Fröhlich, Kristina, Hohenegger, Cathy, Jonker, Harm, Mironov, Dmitrii, Pier Siebesma, A., Teixeira, Joao & Yano, Jun-Ichi 2013 Entrainment and detrainment in cumulus convection: an overview. *Quarterly Journal of the Royal Meteorological Society* **139** (670), 1–19.

Roshko, A. 1961 Experiments on the flow past a circular cylinder at very high Reynolds number. *J. Fluid Mech* (1924), 345–356.

Sadeh, W. Z. & Brauer, H. J. 1980 A visual investigation of turbulence in stagnation flow about a circular cylinder. *Journal of Fluid Mechanics* **99** (1), 53–64.

Sadeh, W. Z. & Saharon, D. B. 1982 Turbulence effect on crossflow around a circular cylinder at subcritical Reynolds numbers. *NASA Contractor Report* (3622).

da Silva, C. B., Hunt, J. C. R., Eames, I. & Westerweel, J. 2014 Interfacial Layers Between Regions of Different Turbulence Intensity. *Annual Review of Fluid Mechanics* **46** (1), 567–590.

da Silva, Carlos Bettencourt & dos Reis, Ricardo José Nunes 2011 The role of coherent vortices near the turbulent/non-turbulent interface in a planar jet. *Philosophical Transactions of the Royal Society A: Mathematical, Physical and Engineering Sciences* **369** (1937), 738–753.

de Silva, Charitha M., Philip, J. & Marusic, I. 2013 Minimization of divergence error in volumetric velocity measurements and implications for turbulence statistics. *Experiments in Fluids* **54**, 1–17.

Silva, Tiago S., Zecchetto, Marco & Da Silva, Carlos B. 2018 The scaling of the turbulent/non-turbulent interface at high Reynolds numbers. *Journal of Fluid Mechanics* **843**, 156–179.

Sreenivasan, K. R., Ramshankar, R. & Meneveau, C. 1989 Mixing, entrainment and fractal dimensions of surfaces in turbulent flows. *Proceedings of the Royal Society of London A: Mathematical, Physical and Engineering Sciences* **421**, 79–108.

Taveira, Rodrigo R, Diogo, José S, Lopes, Diogo C & da Silva, Carlos B 2013 Lagrangian statistics across the turbulent-nonturbulent interface in a turbulent plane jet. *Physical Review E* **88** (4), 043001.

Taveira, Rodrigo R & da Silva, Carlos B 2014 Characteristics of the viscous superlayer in shear free turbulence and in planar turbulent jets. *Physics of Fluids* **26** (2), 021702.

Taylor, G. I. 1936 Statistical Theory of Turbulence V — Effect of Turbulence on Boundary Layer Theoretical Discussion of Relationship Between Scale of Turbulence and Critical Resistance of Spheres. *Proceedings of the Royal Society of London* **156** (888), 307–317.

Taylor, G. I. 1938 Production and dissipation of vorticity in a turbulent fluid. *Proceedings of the Royal Society of London. Series A - Mathematical and Physical Sciences* **164** (916), 15–23.

Townsend, A. A. 1976 *The Structure of Turbulent Shear Flow*. Cambridge University Press.

van Dyke, M. 1982 An album of fluid motion. *NASA STI/Recon Technical Report A* **82**, 36549.

Van Reeuwijk, M. & Holzner, M. 2013 The turbulence boundary of a temporal jet. *Journal of Fluid Mechanics* **739**, 254–275.

Vanderwel, C. & Tavoularis, S. 2014 On the accuracy of plif measurements in slender plumes. *Experiments in Fluids* **55** (8), 1801.

Vollmers, Heinrich 2001 Detection of vortices and quantitative evaluation of their main parameters from experimental velocity data. *Measurement Science and Technology* **12** (8), 1199–1207.

Watanabe, Tomoaki, Sakai, Yasuhiko, Nagata, Kouji, Ito, Yasumasa & Hayase, Toshiyuki 2014 Vortex stretching and compression near the turbulent/non-turbulent interface in a planar jet. *Journal of Fluid Mechanics* **758**, 754–785.

Watanabe, T, Zhang, X & Nagata, K 2018 Turbulent/non-turbulent interfaces detected in dns of incompressible turbulent boundary layers. *Physics of Fluids* **30** (3), 035102.

Westerweel, J. 2000 Effect of sensor geometry on the performance of piv interrogation. In *Laser Techniques Applied to Fluid Mechanics* (ed. R. J. Adrian, D. F. G. Durão, F. Durst, M. V. Heitor, M. Maeda & J. H. Whitelaw), pp. 37–55. Berlin, Heidelberg: Springer Berlin Heidelberg.

Westerweel, J., Fukushima, C., Pedersen, J. & Hunt, J. C. R. 2005 Mechanics of the Turbulent-Nonturbulent Interface of a Jet. *Physical Review Letters* **95** (17), 1–4.

Westerweel, J, Fukushima, C, Pedersen, Jakob Martin & Hunt, JCR 2009 Momentum and scalar transport at the turbulent/non-turbulent interface of a jet. *Journal of Fluid Mechanics* **631**, 199–230.

Williamson, C. H. K. 1996 Vortex Dynamics in the Cylinder Wake. *Annual Review of Fluid Mechanics* pp. 477–539.

Wise, Adam S & Bachynski, Erin E 2020 Wake meandering effects on floating wind turbines. *Wind Energy* **23** (5), 1266–1285.

Wynn, A., Pearson, D. S., Ganapathisubramani, B. & Goulart, P. J. 2013 Optimal mode decomposition for unsteady flows. *Journal of Fluid Mechanics* **733**, 473–503.

Zhou, Y. & Vassilicos, J. C. 2017 Related self-similar statistics of the turbulent/non-turbulent interface and the turbulence dissipation. *Journal of Fluid Mechanics* **821**, 440–457.